

ADA082163

(12)
A071166

LEVEL

EPITAXIAL GROWTH OF SEMI-INSULATING GaAs

RCA Laboratories
Princeton, New Jersey 08540

FINAL REPORT
for the period 1 July 1977 to 31 August 1979

The views and conclusions contained in this document are those of the authors and should not be interpreted as necessarily representing the official policies, either expressed or implied, of the Defense Advanced Research Projects Agency or the U.S. Government. Approved for public release; distribution unlimited.

DTIC
ELECTE
MAR 21 1980
S A

Sponsored by
Defense Advanced Research Projects Agency (DOD)
Arlington, Virginia 22209

DARPA Order No. 3441 BASIC
Program Code No. 7D10

Monitored by
Office of Naval Research
Arlington, Virginia 22217
Under Contract No. N00014-77-C-0542

DISTRIBUTION STATEMENT A
Approved for public release
Distribution Unlimited

FILE COPY

80 3 20 0 15

UNCLASSIFIED

SECURITY CLASSIFICATION OF THIS PAGE (When Data Entered)

REPORT DOCUMENTATION PAGE		READ INSTRUCTIONS BEFORE COMPLETING FORM
1. REPORT NUMBER	2. GOVT ACCESSION NO.	3. RECIPIENT'S CATALOG NUMBER
4. TITLE (and Subtitle)		5. TYPE OF REPORT & PERIOD COVERED
6. EPITAXIAL GROWTH OF SEMI-INSULATING GaAs,		Final Report
		(1 Jul 1977 to 31 Aug 1979)
7. AUTHOR(s)		8. CONTRACT OR GRANT NUMBER(s)
S. T. Jolly, E. C. Douglas, S. G. Liu, C. P. Wu, C. W. Magee, and S. Y. Narayan		DARPA Order No. 3441 BASIC
9. PERFORMING ORGANIZATION NAME AND ADDRESS		Program Code 7D10
RCA Laboratories		10. PROGRAM ELEMENT, PROJECT, TASK AREA & WORK UNIT NUMBERS
Princeton, New Jersey 08540		PE 61101E/Program
11. CONTROLLING OFFICE NAME AND ADDRESS		Code 7D10/NR 243-018
Defense Advanced Research Projects Agency		12. REPORT DATE
(DOD)		1 January 1980
1400 Wilson Boulevard		13. NUMBER OF PAGES
Arlington, Virginia 22217		100
14. MONITORING AGENCY NAME & ADDRESS (if different from Controlling Office)		15. SECURITY CLASS. (of this report)
Office of Naval Research		Unclassified
Arlington, Virginia 22217		15a. DECLASSIFICATION/DOWNGRADING SCHEDULE
		N/A
16. DISTRIBUTION STATEMENT (of this Report)		
Approved for public release; distribution unlimited.		
17. DISTRIBUTION STATEMENT (of the abstract entered in Block 20, if different from Report)		
18. SUPPLEMENTARY NOTES		
ONR Scientific Officer		
Telephone: (202) 696-4218		
19. KEY WORDS (Continue on reverse side if necessary and identify by block number)		
Semi-insulating (SI) GaAs Ion implantation		
Epitaxial growth Laser annealing		
Chromium doping		
Buffer layers		
20. ABSTRACT (Continue on reverse side if necessary and identify by block number)		
<p>This program was aimed at the study of epitaxial growth of high-resistivity GaAs, high-energy implantation of donors into GaAs, and the use of high-power lasers for annealing implanted GaAs layers. We have made significant progress in these three areas.</p> <p>We have grown high-resistivity Cr-doped GaAs layers with good surface morphology using both Ga/HCl/AsH₃/H₂ and Ga/AsCl₃/H₂ processes. n-Layers grown on epitaxial buffer layers have consistently shown lower compensation than direct growth on SI GaAs substrates. Cr-doped layers have been grown on both SI GaAs and n-GaAs substrates. Ion implantation into epitaxial buffer layers, in general, leads to higher electron mobility than direct implantation.</p>		

DD FORM 1 JAN 73 1473

UNCLASSIFIED

SECURITY CLASSIFICATION OF THIS PAGE (When Data Entered)

299000

AB

UNCLASSIFIED

SECURITY CLASSIFICATION OF THIS PAGE (When Data Entered)

20.

SIMS measurements of the Cr profile in the epi-buffer and n-layers grown on epitaxial Cr-doped buffers sometimes show anomalous pile-up of Cr at the interfaces. This pile-up does not occur if growth is not interrupted. It is speculated that this may be related to deviations in gas-phase stoichiometry during growth start. While we can grow layers without Cr pile-up at the interface, the exact mechanism of the presence/absence of Cr pile-up is not understood.

While high-quality (low compensation) n-layers can be grown on Cr-doped buffer layers, problems arise during the growth of n⁺-n structures. This is particularly true when very highly doped ($\sim 10^{19} \text{ cm}^{-3}$) n⁺-layers are grown. The problem manifests itself as a "conducting knee" in the buffer. SIMS measurements indicate penetration of the n⁺-dopant into the buffer layer.

We have successfully grown high-resistivity layers on SI GaAs substrates by using NH_3 gettering to reduce the background donor concentration by decreasing Si incorporation from the quartz reactor tube. Diffusion from the SI GaAs substrate compensates the remaining donors. n and n⁺-n structures can be grown on NH_3 getterd buffer layers without any anomalous effects as described for Cr-doping.

Implantation of ^{28}Si into SI GaAs up to an implant energy level of 1.2 MeV has been investigated. A maximum range of 1.1 μm was measured by SIMS. Electrical activation and mobility following thermal annealing are comparable to or higher than (depending on implant parameters) those for low-energy (50 to 250 keV) implantation. Higher activation was observed in 1-MeV Si-implanted GaAs than in 200-keV implants at high doses (10^{14} to 10^{15} at./cm^2). Electron density profiles measured on the 1-MeV implants showed a reasonable agreement with normalized SIMS profile.

We have studied profile and range statistics of ^{28}Si -implanted GaAs with energies up to 1.2 MeV using SIMS. ^{28}Si profiles $\sim 1 \mu\text{m}$ deep have been produced using multiple implants. After annealing the measured electron density distribution confirms the 1- μm depth with an average electron density of $\sim 5 \times 10^{17} \text{ cm}^{-3}$.

We have investigated laser annealing of high-dose Si-implanted GaAs using high-power pulsed Nd:glass and ruby lasers. Electrical activation of high-dose, low-energy implanted samples is many times higher for laser-annealed than for thermally annealed samples. Ohmic contacts can be formed to laser-annealed samples without alloying.

Optical absorption in Si-implanted GaAs wafers irradiated with high-power Nd:glass laser pulses was studied. The implant-enhanced absorption at a given infrared wavelength increases with implant dose. This enhanced absorption is greatly reduced following annealing due to lattice reordering.

Impurity distribution in as-implanted, thermally annealed, and laser-annealed samples has been investigated by SIMS. The impurity redistribution depends upon energy, implantation dose, and laser pulse energy density. Substantial impurity broadening was observed in high-dose implanted samples irradiated with high energy-density ($\sim 2 \text{ J/cm}^2$). The broadening is believed to be associated with diffusion in the liquid GaAs created by the high-energy laser pulse. Uneven ripple observed using Nomarski interference contrast confirms occurrence of melting.

UNCLASSIFIED

SECURITY CLASSIFICATION OF THIS PAGE (When Data Entered)

PREFACE

This final report describes research performed in the Microwave Technology Center of RCA Laboratories during the period 1 July 1977 to 31 August 1979 in a program sponsored by Defense Advanced Research Projects Agency (DOD) under DARPA Order No. 3441 BASIC and monitored by the Office of Naval Research under Contract No. N00014-77-C-0542. F. Sterzer is the Center's Director; S. Y. Narayan is the Project Supervisor. S. T. Jolly carried out the research on epitaxial growth; E. C. Douglas, S. G. Liu, and C. P. Wu carried out the ion-implantation and laser annealing work; the SIMS analyses of Si were made by C. W. Magee, and SIMS analyses of Cr were made by Charles Evans and Associates, San Mateo, CA.

Accession For	
NTIS GRA&I	<input checked="checked" type="checkbox"/>
DDC TAB	<input type="checkbox"/>
Unannounced	<input type="checkbox"/>
Justification	
By _____	
Distribution/ _____	
Availability Codes	
Dist.	Avail and/or special
A	

TABLE OF CONTENTS

Section	Page
I. INTRODUCTION	1
II. SEMI-INSULATING GaAs GROWTH	3
A. Introduction	3
B. Cr Doping in the Ga/HCl/AsH ₃ /H ₂ System	3
C. NH ₃ -Gettered High-Resistivity Layers	5
D. Cr Doping in the AsCl ₃ /Ga/H ₂ System	5
E. Evaluation of Submicrometer n-Layers	15
F. Other Doping Methods	18
1. Fe Doping Using Fe(CO) ₅	18
2. Cr Doping Using Cr(CO) ₆	18
III. MATERIAL CHARACTERIZATION	20
A. Introduction	20
B. Room-Temperature Photoconductivity	21
1. Photoconductivity Measurements, SI Substrates	22
2. High-Resistivity Epi Layers on SI GaAs Substrates	25
C. Resistivity Measurements	27
D. Secondary Ion-Mass Spectroscopy (SIMS)	31
IV. HIGH-ENERGY (UP TO 1.2 MeV) ION IMPLANTATION	38
A. High-Energy Van de Graaff for Heavy Ion Implantation	38
B. Calibration Implants Using ¹¹ B ⁺ Beam	39
C. Implantation of ²⁸ Si ⁺ into GaAs	41
1. Calibration	41
2. The Formation of Flat Profiles of Si in GaAs	46
3. Mobility, Carrier Concentration, and Activation Energy	52
4. Carrier Concentration Distribution	55

TABLE OF CONTENTS (Continued)

Section	Page
V. LASER ANNEALING	59
A. Introduction	59
B. High-Power Pulsed Laser System	60
C. Pulsed Nd:Glass Laser Annealing	62
D. Pulsed Ruby-Laser Annealing	66
E. Unalloyed Ohmic Contacts	70
F. SIMS Measurements	71
G. Surface Morphology Study	77
VI. SUMMARY AND CONCLUSIONS	80
REFERENCES	83
APPENDIX - Van der Pauw Measurements of High-Resistivity Materials	84

LIST OF ILLUSTRATIONS

Figure	Page
1. Carrier profile of n-layer grown on Cr-doped buffer layer. Note absence of buffer "knee"	5
2. Carrier profile deduced from resistivity measurements. Note absence of conducting knee. $\text{AsH}_3/\text{Ga}/\text{HCl}/\text{H}_2$ system	6
3. Carrier profile showing conducting knee. $\text{AsH}_3/\text{Ga}/\text{HCl}/\text{H}_2$ system .	6
4. Another example of conducting knee. $\text{AsH}_3/\text{Ga}/\text{HCl}/\text{H}_2$ system	7
5. NH_3 -gettered layer grown on nominally Cr-free n^+ substrate	8
6. n-Layer grown on NH_3 -gettered buffer layer. The NH_3 -gettered layer was grown on a Cr-doped substrate	9
7. Carrier profile of n^+ -n-layer on NH_3 -gettered buffer layer. Note absence of conducting knee. Wafer B507	10
8. Carrier profile of n^+ -n-layer on NH_3 -gettered buffer layer. Note absence of conducting knee. Wafer B523	10
9. Carrier profile of n^+ -n-layer on NH_3 -gettered buffer layer. Note absence of conducting knee. Wafer B524	11
10. n^+ -n-Layer grown on Cr-doped buffer layer in $\text{AsCl}_3/\text{Ga}/\text{H}_2$ system. No conducting knee	12
11. Example of n^+ -n-layer showing conducting knee, $\text{AsCl}_3/\text{Ga}/\text{H}_2$ system. Wafer D630	13
12. Example of n^+ -n-layer showing conducting knee, $\text{AsCl}_3/\text{Ga}/\text{H}_2$ system. Wafer D631	13
13. Cr-doped layer grown on n^+ substrate using $\text{AsCl}_3/\text{Ga}/\text{H}_2$ system. An n-layer was grown before the Cr-doped layer	14
14. High-resistivity layer grown on n^+ substrate using bypass AsCl_3 . An n-layer was grown before the high-resistivity layer ..	14
15. Carrier profile of 0.175- μm n-layer, wafer B532	17
16. Carrier profile of 0.175- μm n-layer, wafer B533	17
17. Room temperature photoconductivity response of SI GaAs sub- strate. Note evolution of a peak at ~ 0.9 eV as Cr content increases	23
18. Photoconductive response of two nominally O-doped SI GaAs substrates	23

LIST OF ILLUSTRATIONS (Continued)

Figure	Page
19. Photoconductive response of three Morgan Cr-doped SI GaAs substrates	24
20. Nominally O-doped and Cr-doped SI GaAs substrates. Note similar photoconductive response	25
21. Photoconductive response of high resistivity epitaxial layers on SI GaAs substrate (M4). Absorption coefficient plot also shown	26
22. Plot of $1000/T'$ as a function of $1000/T$	28
23. $\rho T^{1.5}$ as a function of $1000/T'$ for Morgan M4 substrates	29
24. Hall mobility as a function of $1000/T'$ for Morgan M4 substrates .	30
25. $\rho T^{1.5}$ as a function of $1000/T'$ for NK SI GaAs substrate	31
26. $\rho T^{1.5}$ data points for D80 on NK substrate. The straight line is the characteristic of the substrate alone	32
27. SIMS profile of ^{52}Cr showing pile-up at interface. Note decreasing ^{52}Cr trend in undoped layer	33
28. SIMS profile of Cr-doped epitaxial layer. There is some pile-up at interface	33
29. SIMS profile of substrate-undoped Cr-doped structure. Note Cr pile-up at interface	34
30. ^{52}Cr and ^{80}Se SIMS profiles measured with primary O and Cs beams, respectively. Note Cr pile-up at interface and sharp Se profile	34
31. SIMS profile of ^{80}Se in an $n^+-n-n(\text{buffer})$ -SI GaAs wafer showing Se penetration into the Cr-doped buffer layer	35
32. SIMS profile of Cr-doped layer grown in $\text{AsCl}_3/\text{Ga}/\text{H}_2$ system. No growth interruption, no Cr pile-up	36
33. Another example of a good buffer layer	36
34. Cr-buffer layer with nonuniform Cr concentration	37
35. Carrier profile of Cr-doped layer grown on n^+ substrate. SIMS could not detect Cr in middle layer indicating a Cr concentration less than 10^{16} cm^{-3}	37

LIST OF ILLUSTRATIONS (Continued)

Figure	Page
36. SIMS plots of a 60-keV ^{11}B implant performed on the Laboratories machine and a 1-MeV ^{11}B implant performed on the FEC Van de Graaff implanter	40
37. SIMS plots of a group of samples implanted with increasing energies using the FEC Van de Graaff implanter	41
38. Measured value of the range R_p for the series of ^{11}B implants ...	42
39. SIMS plot of the first $^{28}\text{Si}^+$ implant into a GaAs substrate using the Van de Graaff machine	43
40. SIMS profiles of implants made at energies of 40, 120, 200, and 280 keV	44
41. SIMS profiles of implants made at energies of 0.7, 0.8, 0.9, 1.0, 1.2 MeV	44
42. SIMS plots of 1-MeV ^{28}Si implants made into GaAs at different dose levels	45
43. Curve-fitting to experimental data, 0.7-MeV $^{28}\text{Si}^+$ into GaAs	46
44. Curve-fitting to experimental data, 1.18-MeV $^{28}\text{Si}^+$ into GaAs	47
45. Composite plots of curves corresponding to the data given in Fig. 41	48
46. Reduction of data to R_p and ΔR_p values	49
47. Comparison of calculated and actual SIMS profiles, log plot	50
48. Comparison of calculated and actual SIMS profiles, linear plot ..	50
49. SIMS plots of the multiple-implant profiles formed using different dose levels	52
50. Mobility and sheet resistance measured after thermal annealing for samples implanted at different high-energy levels	54
51. Measured sheet carrier concentration as a function Si-implanted samples as 200 keV and 1 MeV	55
52. Electron concentration distribution, 1-MeV, Si-implanted, 1.5×10^{14} at./cm ²	56
53. Electron concentration distribution, 1-MeV, Si-implanted, 5×10^{13} at./cm ²	57
54. Electron concentration distribution, 1-MeV, Si-implanted, 1.5×10^{13} at./cm ²	57

LIST OF ILLUSTRATIONS (Continued)

Figure	Page
55. Carrier concentration of a multiple-implanted sample	58
56. High-power pulsed laser system	61
57. Comparison of thermal and laser annealing; 1.06- μ m, 25-ns single-pulse (Nd:glass) laser was used	63
58. Reflectance measured on an as-implanted wafer (a) and after laser-annealing (b)	64
59. Optical transmission from Si-implanted GaAs sample annealed at different laser energy densities	65
60. Measured values of transmittance (T), reflectance (R), and enhanced absorption ($A-A_0$) for different dose levels	66
61. Sheet electron concentration as a function of dose for ruby-laser and thermal-annealed samples	67
62. Mobility (μ), activation efficiency (η), and sheet resistance (ρ_s) as a function of dose	68
63. Mobility (η), activation efficiency (η), and sheet resistance (ρ_s) as a function of energy density	69
64. I-V characteristics between two unalloyed ohmic contacts	71
65. Resistance between neighboring ohmic contacts as a function of spacing	72
66. SIMS profile of a Si-implanted GaAs sample before and after thermal annealing, 200 keV, 5×10^{14} at./cm ²	73
67. SIMS profile of a Si-implanted GaAs sample before and after thermal annealing, 70 keV, 3×10^{15} at./cm ²	74
68. SIMS profile of a Si-implanted GaAs sample before and after laser annealing, 70 keV, 1×10^{15} at./cm ²	75
69. SIMS profiles: unannealed GaAs wafer; laser-annealed at 1 J/cm ² ; and laser-annealed at 2.3 J/cm ²	76
70. SIMS profiles: unannealed, thermal-annealed, laser- annealed samples	77
71. (a) Nomarski interference contrast. Ruby-laser anneal (2.3 J/cm ²) sample. (b) SEM of same sample at 20K magnification	78

LIST OF ILLUSTRATIONS (Continued)

Figure	Page
72. SEM photographs. (a) As-implanted sample at 20K magnification. (b) Ruby-laser-annealed sample at 1-J/cm^2 energy density (20K magnification)	79
A-1. Schematic of guarded high-impedance van der Pauw system	84

LIST OF TABLES

Table	Page
1. Van der Pauw Measurement Results	16
2. Characteristics of Higher Concentration Layer	19
3. Calculated Multiple Implant Parameters	49
4. Implant Conditions for Flat Profile of Si in GaAs	51
5. 1-MeV Si Implantation in GaAs	53
6. Results of Si-Implanted Wafers at 825 and 970°C	54
7. Comparison of Thermal and Nd:Glass Laser Annealing Data	63

SECTION I

INTRODUCTION

The objectives of this program are to (1) develop techniques for the epitaxial growth of high-resistivity buffer layers on semi-insulating (SI) GaAs substrates, (2) investigate ion implantation of donors into GaAs at energies approaching 1 MeV, and (3) investigate the potential of laser annealing to remove lattice damage caused by ion implantation and to activate the implanted donors.

We have developed methods for the growth of high-resistivity Cr-doped GaAs by vapor-phase epitaxy (VPE) using both the Ga/HCl/AsH₃/H₂ and the Ga/AsCl₃/H₂ systems. We have also succeeded in growing high-resistivity layers in the Ga/HCl/AsH₃/H₂ system by using NH₃ to getter Si from the gas stream. While this method has been described previously in the literature [1], we have been able to grow thicker layers than that achieved previously. Van der Pauw measurements on thin (<0.2 μm) n-layers grown on buffer layers and directly on the substrate indicate that the compensation factor is consistently lower for layers grown on buffers.

The atomic Cr concentration in the Cr-doped buffer layers and n-layers grown thereon was studied by secondary ion-mass spectroscopy (SIMS). It was observed that in some cases there was an anomalous pile-up of Cr at the substrate-buffer and buffer-n-layer interfaces. It was determined that this pile-up does not occur if the growth sequence is continuous (i.e., growth is not interrupted). The mechanism for Cr pile-up is not understood.

High-energy implantation of Si into SI GaAs at energy levels of up to 1.2 MeV has been demonstrated. A range of up to 1.1 μm has been measured by SIMS. Carrier density profiles have been measured on 1-μm-thick n-layers produced by multiple-energy Si implantation.

The investigation of annealing high-dose implanted GaAs using pulsed high-power ruby and Nd:glass lasers was carried out. We have measured activation efficiencies in laser-annealed Si-implanted GaAs that are an order of magnitude

1. G. B. Stringfellow and G. Ham, "Hydride VPE Growth of GaAs for FETs," J. Electrochem. Soc. 124, 1806 (1977).

greater than for samples annealed thermally. Ohmic contacts have been formed on laser-annealed GaAs surfaces without alloying.

A detailed description of the research in these areas is presented in this report.

SECTION II

SEMI-INSULATING GaAs GROWTH

A. INTRODUCTION

The objective of this program is to develop techniques for the vapor-phase growth of high-resistivity epitaxial layers of GaAs on semi-insulating (SI) GaAs substrates. It is believed that such layers when interposed between the substrate and the active device layer will produce a layer with fewer crystal defects and undesirable impurities than one grown directly on the semi-insulating substrate.

Previous reports [2,3] have described successful growth of high-resistivity epitaxial layers by Cr doping using CrO_2Cl_2 as the doping agent in a 2.5-cm bore Ga/HCl/AsH₃/H₂ VPE system. We also described preliminary results on growing high-resistivity GaAs layers by the addition of NH₃ to the reagent gas stream [3]. This final report presents results on the growth of high-resistivity layers in a 5-cm bore Ga/HCl/AsH₃/H₂ system (Reactor B) using CrO_2Cl_2 , NH₃, and other doping agents. We will also describe the results obtained on the growth of SI GaAs using the AsCl₃/Ga/H₂ system (Reactor D).

By growing thin (less than 0.2 μm) doped layers on various semi-insulating substrate materials with and without buffer layers, it has been shown that the presence of a high-resistivity buffer layer does improve the compensation ratio of the subsequent doped epitaxial layer.

Equipment capable of carrying out van der Pauw measurements on high-resistivity samples was constructed.

B. Cr DOPING IN THE Ga/HCl/AsH₃/H₂ SYSTEM

Previous Cr-doping experiments were carried out in the smaller A reactor [2,3]. In this system, the CrO_2Cl_2 was introduced through the Ga zone of the reactor held at approximately 850°C via a separate feed tube. In the work to be described, CrO_2Cl_2 was fed via the support tube of the wafer holder and

2. S. T. Jolly et al., Epitaxial Growth of Semi-Insulating GaAs, Annual Report, Contract N00014-77-C-0542, DARPA Order No. 3461 Basic Program Code 7D10, March 1978.
3. S. T. Jolly et al., Epitaxial Growth of Semi-Insulating GaAs, Interim Report, Contract N00014-77-C-0542, DARPA Order No. 3461 Basic Program Code 7D10, March 1979.

through an extension tube to a point upstream of the substrate. In this arrangement, the CrO_2Cl_2 dopant gas experiences only the lower temperature of the deposition zone (700°C), which results in less decomposition of the CrO_2Cl_2 and reduces the required flow of doping gas by a large factor (approximately 10). The doping gas is a 500-ppm mixture of CrO_2Cl_2 in five-nines pure He. Some deposition of Cr compounds on the inside of the feed tube still occurs. However, the combined effects of using an inert carrier gas and subjecting it to a lower temperature than in the original work reduces the deposition to an acceptable level, and the quartz tubes do not appear to be attacked. Specular GaAs surfaces of good quality are obtained.

In order to evaluate the electrical properties of the high-resistivity layers produced by Cr doping, several techniques have been used. Initially the resistance and breakdown voltage produced by pressing two tungsten probes down onto the substrate about 2 mm apart were measured. If no breakdown occurred at 1600 V and the leakage current was of the order of 10 μA or less, it was assumed that the epitaxial layer was completely high-resistivity material with layer thicknesses of 5 to 7 μm . Later work has shown that epitaxial layers with thin "skins" of n-type material of up to $1 \times 10^{15} \text{ cm}^{-3}$ carrier concentration can give the same result.

An alternative test adopted was to sinter two Sn contacts onto diagonally opposite corners of a square sample and measure the resistance between the contacts. Later, an apparatus capable of carrying out van der Pauw measurements on high-resistivity samples was set up. Typical Cr-doped layers are wafers B365 and B368.

<u>Wafer</u>	<u>Cr-Doped Layer Thickness (μm)</u>	<u>Resistance Across Square Diagonal ($\text{M}\Omega$)</u>
B365	6.0	30
B368	5.7	47

A van der Pauw measurement on a similar wafer, B387, with a Cr-doped layer of 7.5- μm thickness gave the following properties at room temperature:

Resistivity - $8 \times 10^3 \Omega\text{-cm}$

Carrier Concentration - $2.2 \times 10^{12} \text{ cm}^{-3}$ (p-type)

When doped layers are grown on these high-resistivity layers, carrier profiles similar to that shown in Fig. 1 for B371 are obtained. This is a 1.9- μm

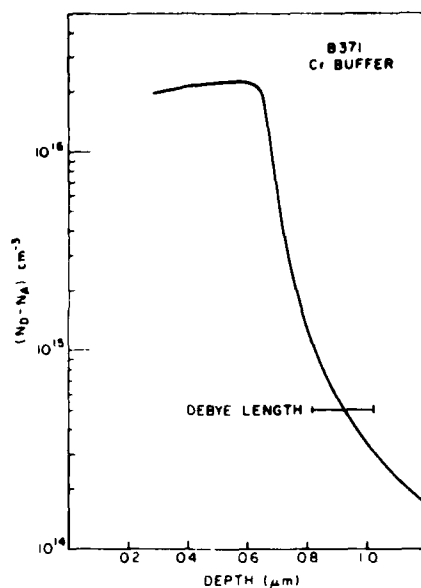


Figure 1. Carrier profile of n-layer grown on Cr-doped buffer layer. Note absence of buffer "knee".

Te-doped layer on a 6.9- μm -thick Cr-doped layer. The profile was obtained after etching approximately 1 μm to enable the profile of the interface to be shown. Hall mobility of this specimen was 6048 at 300 K and 18,960 at 77 K.

A number of wafers for the fabrication of power FETs have been grown and are being evaluated. The structure of these multi-layer wafers are: SI GaAs substrate - high-resistivity buffer layer - 1.25 μm , $8\text{--}10 \times 10^{16} \text{ cm}^{-3}$ active layer - 0.25 μm , 10^{19} cm^{-3} doped contact layer. The 10^{19} cm^{-3} layer is obtained by Se or Te doping. [This high carrier concentration was measured by infrared reflectance techniques.] These wafers were profiled prior to device processing by measuring the resistivity of the total epitaxial layer after a number of partial etching steps. Mobility of the n^+ and n-layers were conservatively assumed to be 1000 and $3000 \text{ cm}^2 \text{ V}^{-1} \text{ s}^{-1}$, respectively. Typical profiles are shown in Figs. 2 to 4. Note that sometimes conducting interfaces appear. When n^+ -layers are not grown, there is no evidence of conducting layers. This effect is still under investigation.

C. NH_3 -GETTERED HIGH-RESISTIVITY LAYERS

Preliminary results on the use of NH_3 in the reagent gas stream to grow high-resistivity layers in the $\text{Ga}/\text{HCl}/\text{AsH}_3/\text{H}_2$ system were reported earlier [3].

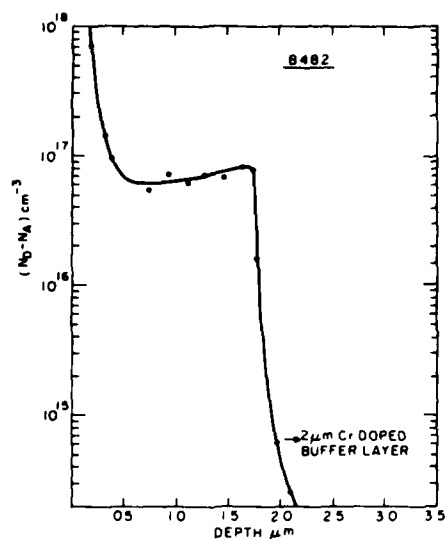


Figure 2. Carrier profile deduced from resistivity measurements. Note absence of conducting knee. $\text{AsH}_3/\text{Ga}/\text{HCl}/\text{H}_2$ system.

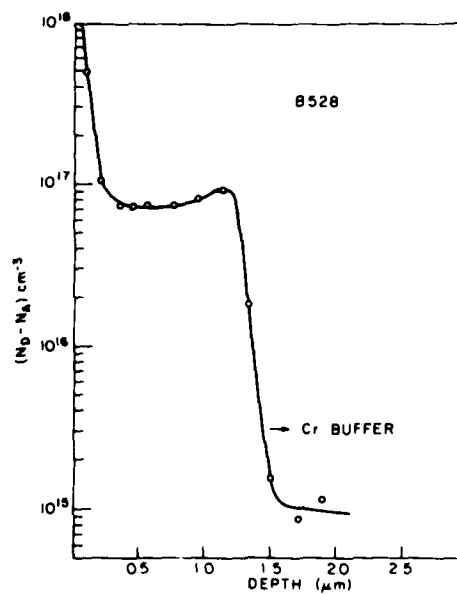


Figure 3. Carrier profile showing conducting knee. $\text{AsH}_3/\text{Ga}/\text{HCl}/\text{H}_2$ system.

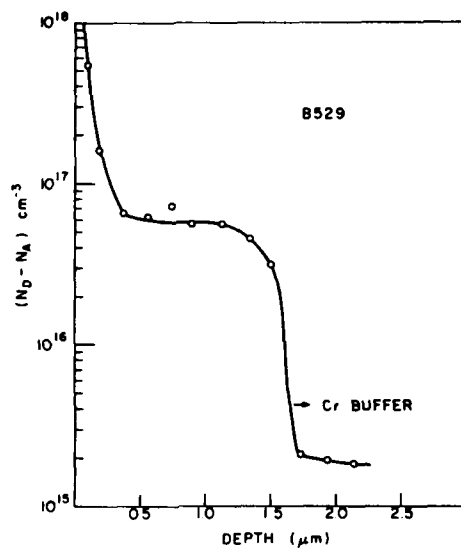


Figure 4. Another example of conducting knee.
AsH₃/Ga/HCl/H₂ system.

It is believed that NH₃ prevents the incorporation of Si from the quartz reactor tube [1]. This lowers the background doping in the reactor. Cr out-diffusion from the SI GaAs substrate [4] then renders this layer semi-insulating.

We have improved our method of the addition of NH₃ into the reactor to prevent clogging of the feed tube. There appears to be some reaction between NH₃ and AsH₃ if the AsH₃ feed is also used for NH₃. With our modified system, no mixture of NH₃ and AsH₃ takes place until they reach the hot zone of the reactor. The gas control system was also modified by addition of a mass flow controller to the ammonia feed line in order to more accurately control the low flow rate (<5 cm³/min) of NH₃ required.

4. H. M. Cox and J. V. DiLorenzo, "Characteristics of an AsCl₃/Ga/H₂ Two-Bubbler GaAs CVD System for MESFET Applications," Proc. Sixth Int. Symp. GaAs and Related Compounds; Inst. Phys. Conf. Series, No. 33b, London, 1977, pp. 11-22.

With slight excess NH_3 , p-type material could be produced, while with slightly insufficient NH_3 , low concentration n-type material could be grown. Two typical wafers are as follows:

Wafer	Layer		$n(b)\text{cm}^{-3}$	Mobility $\text{cm}^2\text{V}^{-1}\text{s}^{-1}$	% NH_3 in Gas Stream
	Thickness (μm)	Type			
B421	7.7	p	1.25×10^{15}	359	1.40
B422	7.5	n	5×10^{13}	5927	0.67

Figure 5 shows the profile of B476 grown on a Cr-free n^+ -substrate. The first layer was a 1.25- μm undoped layer to provide a buffer from the substrate; 3 μm of NH_3 gettered layer followed by 1.5 μm of undoped layer were grown. All layers were grown continuously without growth interruption. The effect of NH_3 gettering is obvious.

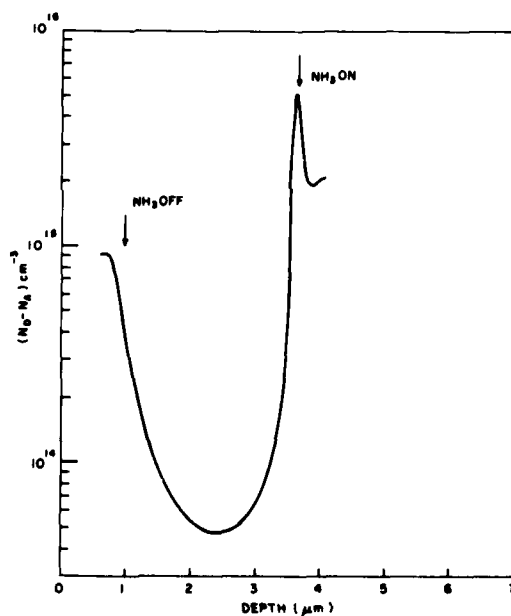


Figure 5. NH_3 -gettered layer grown on nominally Cr-free n^+ substrate.

Figure 6 is an example of an n-layer grown on an NH_3 gettered buffer layer on a Cr-doped SI GaAs substrate.

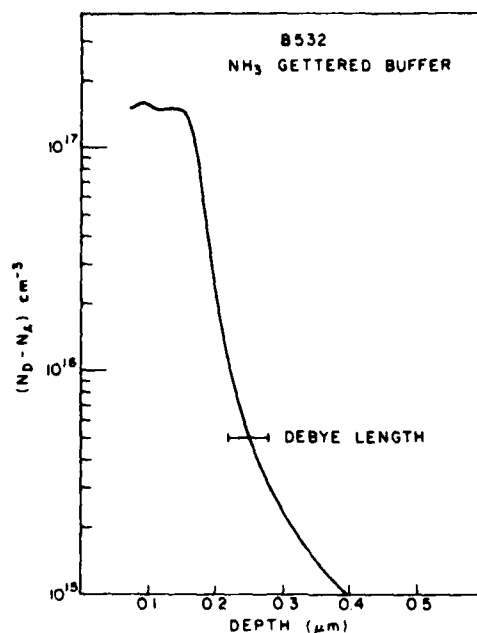


Figure 6. n-Layer grown on NH_3 -getterd buffer layer. The NH_3 -getterd layer was grown on a Cr-doped substrate.

One deposition run was made to determine the effect of continuing the NH_3 flow during growth of a Te-doped layer. Results were as follows for wafer B425 (thickness of NH_3 getterd layer - 3 μm):

	N	μ	$\frac{N_D + N_A}{N_D - N_A}$
Room Temperature	2.04×10^{16}	3745	>5
77 K	1.81×10^{16}	6740	~ 3.8

A possible reason for the poor compensation factor may be insufficient degree of purity of the NH_3 which was an ultrapure grade supplied for semiconductor processing.

A number of wafers have been grown for device fabrication which incorporate an NH_3 doped buffer layer of 4.5 μm thickness. Three of these which have been profiled by the previously mentioned differential resistance technique, are wafers 507, 523, and 524. Figures 7 to 9 show the profiles obtained. These are currently being evaluated for device application. Note the absence of conducting buffer 'knees'.

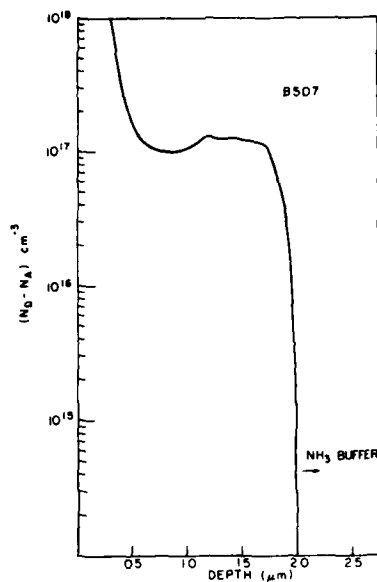


Figure 7. Carrier profile of n^+ -n-layer on NH_3 -gettered buffer layer. Note absence of conducting knee. Wafer B507.

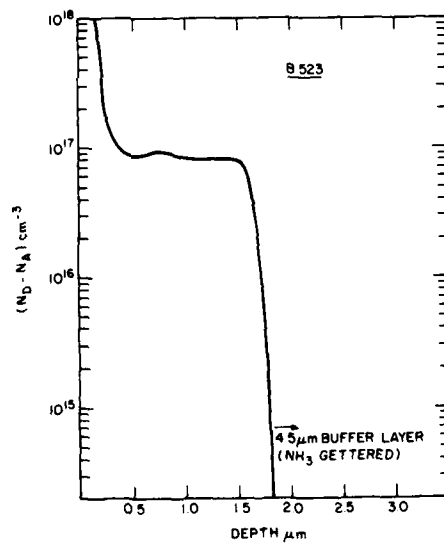


Figure 8. Carrier profile of n^+ -n-layer on NH_3 -gettered buffer layer. Note absence of conducting knee. Wafer B523.

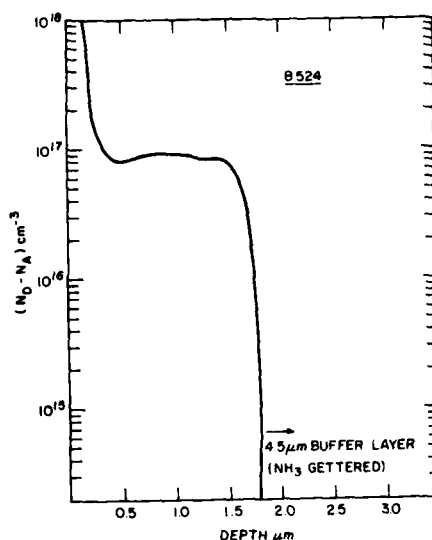


Figure 9. Carrier profile of n^+ -n-layer on NH_3 -gettered buffer layer. Note absence of conducting knee. Wafer B524.

D. Cr DOPING IN THE $\text{AsCl}_3/\text{Ga}/\text{H}_2$ SYSTEM

The reactor employed is a "two bubbler" AsCl_3 system as described elsewhere [4]. One AsCl_3 source is used to saturate the Ga; the second AsCl_3 source bypasses the Ga and controls the mole fraction. Doping gases used are dilute mixtures of SiH_4 in H_2 for growing n^- and n^+ -layers. The substrate holder was modified to permit the introduction of the 500-ppm $\text{CrO}_2\text{Cl}_2/\text{H}_e$ mixture into the reaction gas stream about 7 cm (2.5 in.) ahead of the substrate. In order to obtain a high-resistivity layer, the deposition temperature and mole fraction of AsCl_3 were adjusted to give a background carrier concentration of about $1 \times 10^{15} \text{ cm}^{-3}$. A measure of the resistivity of the Cr-doped layers was obtained by sintering the contacts onto diagonally opposite corners of square samples. The effect of various concentrations of CrO_2Cl_2 is illustrated by the following results.

Run	$\text{CrO}_2\text{Cl}_2/\text{He}$ Mixture (cm^3)	Resistance (Ω)
D539	30	8000
D540	75	6×10^5
D542	120	2×10^8

The thickness of these layers is approximately 5 μm .

Later it was found necessary to reduce the background level of the reactor to $5 \times 10^{14} \text{ cm}^{-3}$ to improve reproducibility. Typical results obtained in attempting to measure n and μ by van der Pauw techniques are those obtained from run D600 (Cr-doped layer approximately $5 \mu\text{m}$ thick). At room temperature n could not be measured. The resistivity was $9 \times 10^4 \Omega\text{-cm}$. At 77 K, the carrier concentration indicated was $4.8 \times 10^{11} \text{ cm}^{-3}$ with a mobility of $1717 \text{ cm}^2 \text{V}^{-1} \text{s}^{-1}$.

A number of wafers having n^+ - and n -layers on a $5\text{-}\mu\text{m}$ Cr-doped layer have been grown. Carrier concentration profiles obtained from such wafers are shown in Figs. 10 to 12. These were obtained as described earlier. Wafers D630 and D631 appear to indicate that the resistivity of the buffer layer is degraded by growth of the top n^+ -layer. In no case do profiles obtained from the automatic profile plotter show this degradation before the n^+ -layer is grown. Other substrates grown in similar runs for device fabrication have not yet been processed.

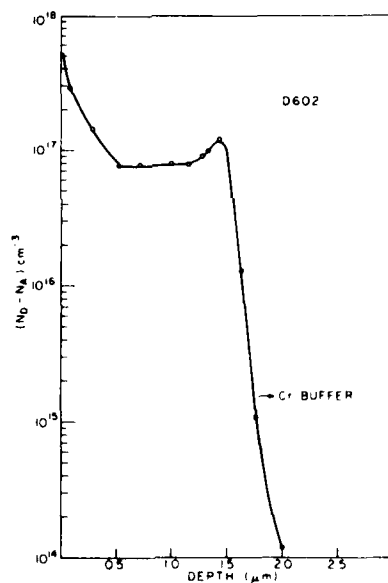


Figure 10. n^+ - n -Layer grown on Cr-doped buffer layer in $\text{AsCl}_3/\text{Ga}/\text{H}_2$ system. No conducting knee.

Experiments have also been carried out to grow Cr-doped layers on Cr-free n^+ -substrates. In these tests, the substrate was Te doped. A layer of undoped GaAs was grown before and after the Cr-doped layer. A typical profile is shown

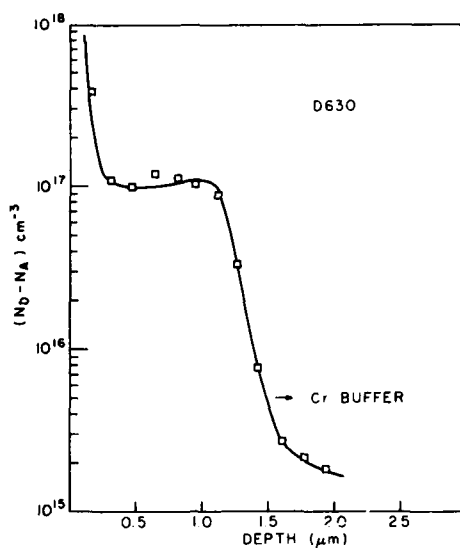


Figure 11. Example of n^+-n -layer showing conducting knee, $\text{AsCl}_3/\text{Ga}/\text{H}_2$ system. Wafer D630.

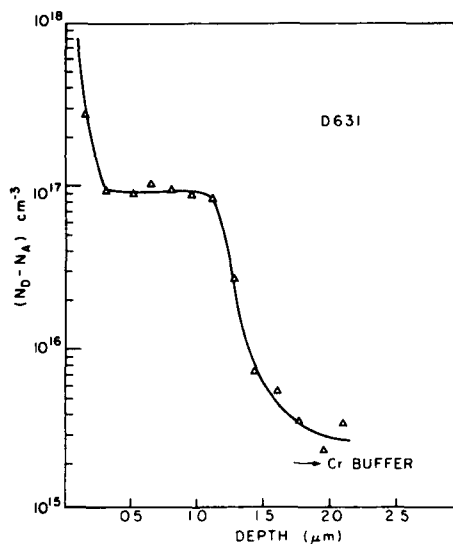


Figure 12. Example of n^+-n -layer showing conducting knee, $\text{AsCl}_3/\text{Ga}/\text{H}_2$ system. Wafer D631.

in Fig. 13. For comparison, a similarly structured wafer, where the high-resistivity layer was produced by changing the As mole fraction, is shown in Fig. 14.

In order to attempt to access the value of a high-resistivity buffer layer on the properties of an n -layer subsequently grown on it, a number of thin

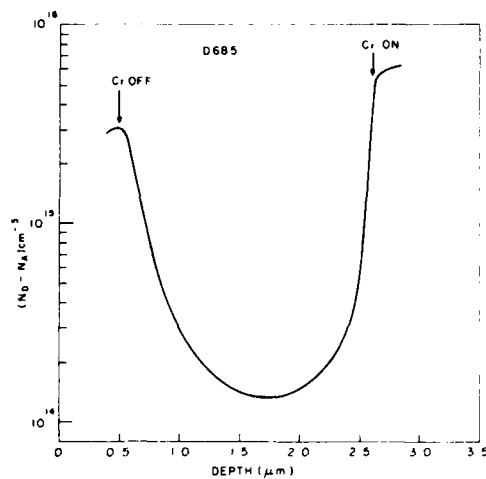


Figure 13. Cr-doped layer grown on n^+ substrate using $\text{AsCl}_3/\text{Ga}/\text{H}_2$ system. An n-layer was grown before the Cr-doped layer.

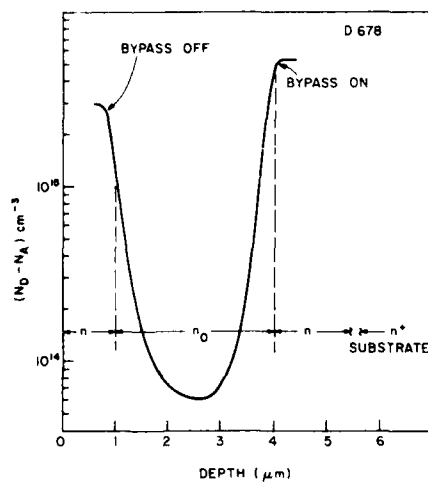


Figure 14. High-resistivity layer grown on n^+ substrate using bypass AsCl_3 . An n-layer was grown before the high-resistivity layer.

(<0.2 μm thick) doped layers have been grown, both on Cr-doped buffer layers and directly on substrates. The results of these experiments are given in subsection E below.

E. EVALUATION OF SUBMICROMETER n-LAYERS

The region of the epitaxial n-layer which most affects the performance of planar devices such as FETs is that immediately adjacent to the substrate or buffer layer. A number of wafers have been grown both directly on SI substrate material from various sources and also on high-resistivity buffer layers produced by Cr doping on NH_3 gettering. In order to maximize the influence of the interface layer on the electrical properties of these epitaxial layers, they were grown to a nominal thickness of 0.2 μm . The average carrier concentrations and mobilities were then determined by van der Pauw measurements. These results are tabulated in Table 1. They were also profiled using an automatic plotter. Typical profiles are shown in Figs. 15 and 16. They indicate that actual thickness of the n-layer is near 0.175 μm . Note that these wafers did not have any anomalous interfaces. The compensation factors, K, were extrapolated from the curves of Rode and Knight [5]. The relative values of K are more significant in estimating trends in data than the absolute values of K.

(1) Averages of compensation factors are:

(a) For B reactor ($\text{Ga}/\text{HCl}/\text{AsH}_3/\text{H}_2$ system):

Layers grown on substrates (300 K)	1.7
Layers grown on substrates (77 K)	1.79
Layers grown on buffer layers (300 K)	1.47
Layers grown on buffer layers (77 K)	1.46

(b) For D reactor ($\text{AsCl}_3/\text{Ga}/\text{H}_2$ system):

Layers grown on substrates (300 K)	1.94
Layers grown on substrates (77 K)	1.78
Layers grown on buffer layers (300 K)	1.81
Layers grown on buffer layers (77 K)	1.32

5. D. L. Rode and S. Knight, "Electron Mobility in GaAs," Phys. Rev. B3, 2534 (1971).

TABLE 1. VAN DER PAUW MEASUREMENT RESULTS

No.	Substrate*	300 K			77 K		
		$(N_D - N_A) \text{ cm}^{-3}$	$\mu \text{ cm}^2 \text{V}^{-1} \text{s}^{-1}$	$\frac{N_D + N_A}{N_D - N_A}$	$(N_D - N_A) \text{ cm}^{-3}$	$\mu \text{ cm}^2 \text{V}^{-1} \text{s}^{-1}$	$\frac{N_D + N_A}{N_D - N_A}$
B537	CS + 4.5 μm Cr doped	6.03×10^{16}	4846	1.7	6.27×10^{16}	7267	1.6
B532	CS + 5 μm NH_3 gettered	1.13×10^{17}	4466	1.35	1.06×10^{17}	6580	1.30
B533	CS	1.59×10^{17}	3949	1.45	1.64×10^{17}	4167	1.65
B534	Mi	7.02×10^{16}	4387	1.8	8.44×10^{16}	5253	1.85
B536	MR2	9.82×10^{16}	4152	1.7	1.1×10^{17}	5098	1.7
B537	Mi	1.14×10^{17}	4272	1.6	1.27×10^{17}	4640	1.75
B538	Mi + NH_3 gettered	1.26×10^{17}	4468	1.3	1.33×10^{17}	5227	1.45
B539	Mi + Cr doped	9.8×10^{16}	4375	1.45	9.46×10^{16}	6091	1.45
B540	CS + Cr doped	9.13×10^{16}	4645	1.4	9.42×10^{16}	6111	1.45
B541	Mi, (Damage gettered)	3.33×10^{17}	3236	1.5	3.55×10^{17}	2937	1.9
B542	Mi, (Damage gettered)	6.04×10^{16}	3904	2.5	6.88×10^{16}	5404	1.75
B543	Mi, (Damage gettered)	1.06×10^{17}	4356	1.5	1.13×10^{17}	5348	1.65
B544	Mi + Cr + NH_3	1.07×10^{17}	4106	1.75	1.07×10^{17}	5721	1.55
B546	CS	2.9×10^{17}	3466	1.4	3.10×10^{17}	3341	1.75
B552	CS + Cr doped	5.8×10^{16}	4810	1.6	6.4×10^{16}	7336	1.15
B553	CS	1.9×10^{17}	3072	2.25	1.98×10^{17}	3195	2.05
D714	MR2	1.15×10^{17}	3820	2.1	1.4×10^{17}	3757	2.1
D718	MR2	6.5×10^{16}	4034	2.4	1.0×10^{17}	5000	1.75
D719	MR2	3×10^{17}	3470	1.45	3.17×10^{17}	3341	1.8
D720	MR2 + Cr doped	1.97×10^{16}	4411	1.95	7×10^{16}	8397	1.3
D721	MR2 - Cr doped	5.8×10^{16}	4360	2.1	6.46×10^{16}	7932	1.35
722	MR2	8.56×10^{16}	4147	1.9	1.2×10^{17}	5862	1.4
724	MR (745°C)	9.88×10^{16}	3645	1.95	1.28×10^{17}	4067	1.95
725	M	9.47×10^{16}	3930	1.85	1.07×10^{17}	5296	1.65
733	B + Cr doped	1.6×10^{17}	3940	1.4	1.45×10^{17}	5514	1.3

*CS - Crystal Specialties Inc. (Cr-doped)
 M - Morgan Semiconductor, Inc., Garland, TX. (Cr-doped)
 MR2 - Metals Research (undoped)
 B - Howard Bertram Assoc.
 Mi - Mitsubishi

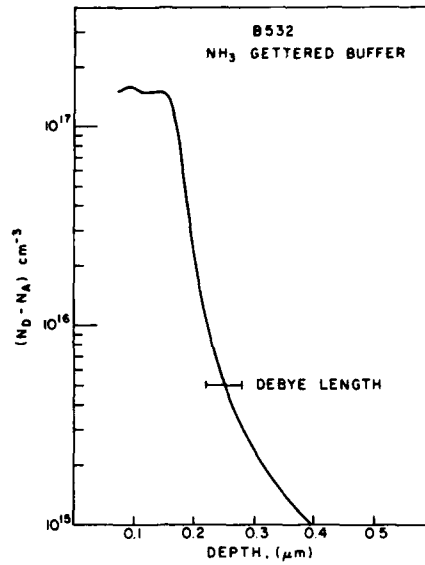


Figure 15. Carrier profile of 0.175- μm n-layer, wafer B532.

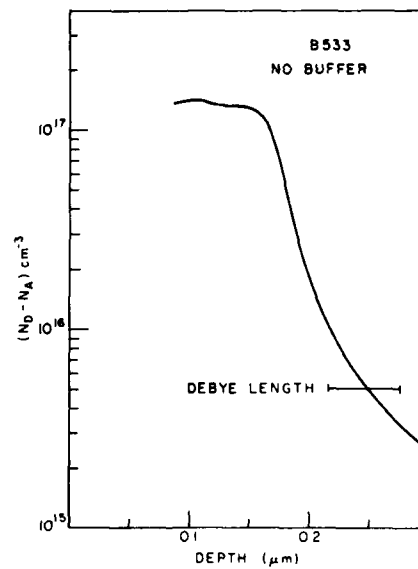


Figure 16. Carrier profile of 0.175- μm n-layer, wafer B533

There appears to be a definite reduction in compensation factor by the use of a buffer layer in both reactors.

- (2) Included in the B reactor results are runs B541, 542, and 543. The substrates employed in these runs were work damaged by spraying fine alumina against the back surface with a sand blaster. Substrates for B541 and 542 were then annealed in the growth reactor at 700°C for 20 minutes prior to growth. The substrate for B543 was annealed under AsH_3 overpressure for 30 minutes at 850°C. A definite improvement in layer quality appears to have occurred as compared with wafer B537, which used the same substrate material with no special treatment.

F. OTHER DOPING METHODS

1. Fe Doping Using $\text{Fe}(\text{CO})_5$

Attempts at Fe doping using $\text{Fe}(\text{CO})_5$ were unsuccessful. A 500-ppm mixture of $\text{Fe}(\text{CO})_5$ in ultrapure He was purchased from Synthatron Corp. and employed in the $\text{Ga}/\text{HCl}/\text{AsH}_3/\text{H}_2$ reactor by direct replacement of the $\text{CrO}_2\text{Cl}_2/\text{He}$ mixture used for Cr doping. A number of runs were made. The layers grown had poor surfaces. Van der Pauw specimens were tested and resistivities of about 300 $\Omega\text{-cm}$ were obtained. However, no Hall voltage could be measured.

2. Cr Doping Using $\text{Cr}(\text{CO})_6$

This compound is a white crystalline solid with high vapor pressure (0.36 mm at 20°C) and appears convenient as a possible source of Cr for doping.

Some experiments were carried out by coupling a refrigerated container containing a little chromium carbonyl in the gas line holder so that the Cr being introduced into the reactor was controllable either by varying the gas flow rate or the container temperature.

Several layers were grown using this technique. Typically, layers with two different characteristics could be grown: the first kind is exemplified by wafer B448. This was a 6- μm layer, the last 2 μm being doped to $4 \times 10^{14} \text{ cm}^{-3}$ and the first 4 μm being high resistivity. If a 6- μm nominally undoped layer were grown on this SI substrate, one typically obtains 3 μm doped to $1 \times 10^{15} \text{ cm}^{-3}$ and 3 μm of high-resistivity layer due to out-diffusion from the substrate. The characteristics of the higher concentration "skin" as measured by the van der Pauw technique are typically as shown in Table 2.

TABLE 2. CHARACTERISTICS OF HIGH CONCENTRATION LAYER

Wafer	300 K		77 K	
B488	$5.7 \times 10^{14} \text{ cm}^{-3}$; 6094 $\text{cm}^2 \text{ V}^{-1} \text{ s}^{-1}$	$8.6 \times 10^{14} \text{ cm}^{-3}$; 73,193 $\text{cm}^2 \text{ V}^{-1} \text{ s}^{-1}$
B453	5×10^{14}	; 5710	8×10^{14}	; 105,636
B455	5×10^{14}	; 7311	8×10^{14}	; 102,100

Increasing the $\text{Cr}(\text{CO})_6$ concentration resulted in material with lower resistivity. It is probable that careful adjustment of reactor parameters would enable high-resistivity layers to be grown but further work is needed. Note also that work has been reported on the successful use of chromium hexacarbonyl in reactors using organometallic compounds of Ga and AsH_3 [6]. In this method, rf heating is employed which only heats the gas stream locally around the substrate, which is desirable when employing thermally unstable compounds such as Cr and iron carbonyl.

6. S. J. Bass, "Growth of Semi-Insulating Epitaxial GaAs by Cr Doping in the Metal Alkyl Hydride System," J. Cryst. Growth 44, 29 (1978).

SECTION III

MATERIAL CHARACTERIZATION

A. INTRODUCTION

The detection and identification of deep levels in high-resistivity GaAs is an important step toward characterization of the material. Cr, Fe, and O are the most common elements used for producing deep levels. Some investigators believe that both Cr and O are necessary to produce SI GaAs [7]. "Cr-free" undoped GaAs has also been reported [8]. The analytical detection and quantitative measurement of the elements causing deep levels is difficult, particularly in thin layers. The Cr concentration in typical Cr-doped GaAs is, for example, in the parts-per-million level. To date, we have found that only spark-source mass spectroscopy (SSMS) and secondary ion-mass spectroscopy (SIMS) have reliably determined Cr in GaAs.

This effort was directed toward characterizing SI GaAs both in bulk form as purchased from various vendors and epitaxially grown samples. During the course of the program, we measured room-temperature photoconductive response, evaluated layers by van der Pauw measurements, made SSMS measurements on substrates obtained from various manufacturers, carried out SIMS measurements on Cr-doped epi-layers and various test structures, and evaluated layers grown on epitaxial high-resistivity layers. The results of the van der Pauw measurements were discussed earlier. We now describe the results of our photoconductivity and SIMS study.

7. R. Zucca, "Electrical Compensation in Semi-Insulating GaAs," J. Appl. Phys. 48, 1987 (1977).
8. R. L. Henry and E. M. Swiggard, "LEC Growth of InP and GaAs Using PBN Crucibles," Proc. Sixth Int. Symp. GaAs and Related Compounds, Inst. Phys. Conf. Series, 33b, London 1977, pp. 28-36.

B. ROOM-TEMPERATURE PHOTOCONDUCTIVITY

This effort was carried out during the first phase of this program. It has been known for some time [9-11] that transitions to and/or from Cr acceptors in SI GaAs could be excited optically with a photon energy of about 0.9 eV. It is not clear in the literature whether holes or electrons are responsible for the increased photoconduction with this subgap illumination, although this could be determined with a photo-Hall experiment. Nevertheless, a peak in the photoconductive spectral response at 0.9 eV appears to be the "signature" of Cr presence in the lattice.

The measurement of photoconductivity as a function of photon energy was carried out using a Bausch & Lomb* grating monochromator with appropriate filters. Measurements involving optical excitation are, in general, sensitive not only to the incident wavelength, but also to the intensity of the radiation. Since the output curve of the monochromator/filter combination is not independent of the wavelength, the system has to be calibrated. The need to employ filters to remove higher order grating modes usually enhances intensity variations as a function of wavelength. There are two available options:

- (a) Normalize the measured dependent variable to the intensity of radiation. For example, the photoconductivity is normalized to μW of incident radiation. This assumes implicitly that the measured parameter varies linearly with intensity. This is not always true; even simple photoconductivity can vary sub- or super-linearly with excitation intensity depending upon the position of the quasi-Fermi level with respect to traps, etc.
- (b) Change the monochromator exit slit setting to produce the same intensity at all wavelengths. Changing slit settings, however, affects spectral purity which may not be reproducible. This can cause problems particularly in the vicinity of sharp quantum transitions such as the band edge.

9. D. R. Heath, P. R. Selway, and C. C. Tooke, "Photoconductivity and Infrared Quenching in Chromium-doped Semi-insulating Gallium Arsenide," Brit. J. Appl. Phys. (J. Phys. D) 1 (Ser. 2), 29 (1968).
10. W. Pleasiewicz, "Photoelectronic Investigations of Semi-Insulating p-Type GaAs:Cr Containing Neutral Chromium Acceptors," J. Phys. Chem. Solids 38, 1079 (1977).
11. H. J. Stocker, "A Study of Deep Impurity Levels in GaAs Due to Cr and O by AC Photoconductivity," J. Appl. Phys. 48, 4583 (1977).

*Bausch & Lomb, New York, NY.

The procedure used in most of our measurements was option a; however, some measurements were made using option b. The corrections and slit setting for various monochromator/filter combinations were determined using a tungsten source and a calibrated thermopile.

1. Photoconductivity Measurements, SI Substrates

Photoconductivity measurements were made using square samples with alloyed In (or Sn) ohmic contacts at the four corners. This is a typical van der Pauw configuration used for resistivity and Hall mobility measurements. The ohmic contacts were shielded from the incident radiation. Since the sample impedances are high, a special circuit was designed and built to allow measurement. Using IC operational amplifiers (CA3130), the differential sample voltage was converted to a single-ended signal at unity voltage gain and an input impedance of greater than 10^{12} ohm.

Figure 17 shows the room temperature (300 K) photoconductive response of three bulk grown substrates. The conductivity per μW of incident radiation is plotted as a function of photon energy. Note the evolution of a peak at 0.9 eV as the Cr content increases. The Cr content was measured by SSMS.

The Sumitomo* oxygen-doped substrate served as a control in the experiment. The PC response of this material is somewhat featureless at 0.9 eV, as expected. The Morgan** substrate did not show evidence of a peak at 0.9 eV. SSMS determined that the concentration of Cr in this sample was about 0.1 ppma- ($2.3 \times 10^{15} \text{ cm}^{-3}$). The Laser Diode† material exhibits a definite peak at 0.9 eV and was determined, by SSMS, to have a Cr concentration of about 1.0 ppma- ($2 \times 10^{16} \text{ cm}^{-3}$). In addition, the Laser Diode material showed lower dark conductivity than the Morgan and had the slow photoresponse characteristic of a high concentration of deep traps.

Figure 18 shows the photoconductive response of two nominally (as specified by vendor) O-doped SI GaAs substrates. Note that the Sumitomo O-doped sample is featureless at 0.9 eV while the Laser Diode O-doped sample appears to show a peak at 0.9 eV. Samples from these boules were also analyzed by SSMS. The Laser Diode sample shows a Cr concentration of $3.5 \times 10^{16} \text{ cm}^{-3}$ and

*Sumitomo Electric Industries, Ltd., Osaka, Japan.

**Morgan Semiconductor Inc., Garland, TX.

†Laser Diode Laboratories, Inc., Metuchen, NJ.

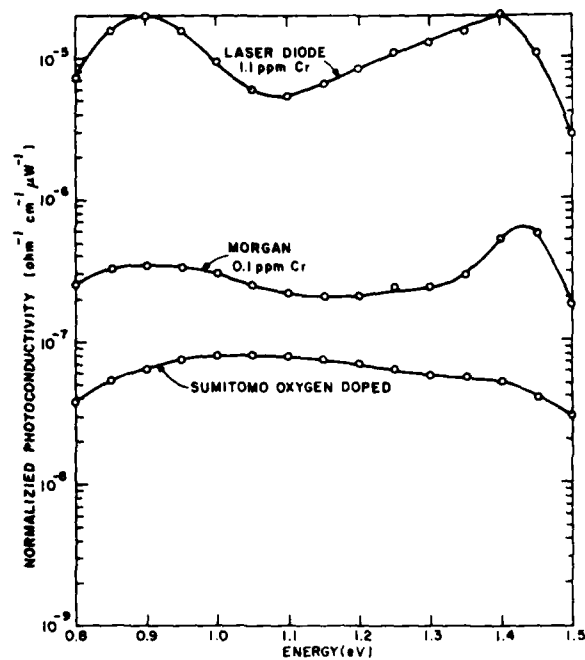


Figure 17. Room temperature photoconductivity response of SI GaAs substrate. Note evolution of a peak at ~ 0.9 eV as Cr content increases.

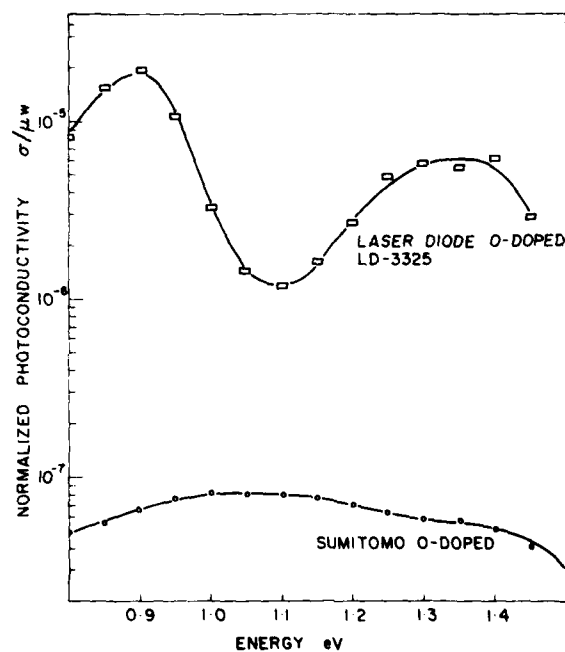


Figure 18. Photoconductive response of two nominally O-doped SI GaAs substrates.

an oxygen concentration of about 10^{16} cm^{-3} while the Sumitomo sample shows $4 \times 10^{16} \text{ cm}^{-3}$ of Cr and $3 \times 10^{16} \text{ cm}^{-3}$ of O. The strikingly different photoconductive response of two wafers with similar Cr and O concentrations as measured by SSMS is not understood. It should be noted that O concentration measured by SSMS is somewhat uncertain. Both these substrates could withstand annealing at 850°C for 20 minutes in a hydrogen atmosphere without degradation of resistivity.

Figure 19 shows the room-temperature photoconductive response of three Morgan semi-insulating GaAs substrates. Note that M2 and M4 have reasonably similar response with broad peaks at about 0.9 eV characteristic of Cr. Substrate M1, on the other hand, shows different characteristics. SSMS measurements show Cr content of $< 1.7 \times 10^{15} \text{ cm}^{-3}$ for M1, $1.6 \times 10^{16} \text{ cm}^{-3}$ for M2, and $2.5 \times 10^{15} \text{ cm}^{-3}$ for M4. Under a high-temperature anneal test (750°C , 30 min), M2 did not show conversion to lower resistivity, some M4 samples showed slight degradation, while M1 samples degraded considerably.

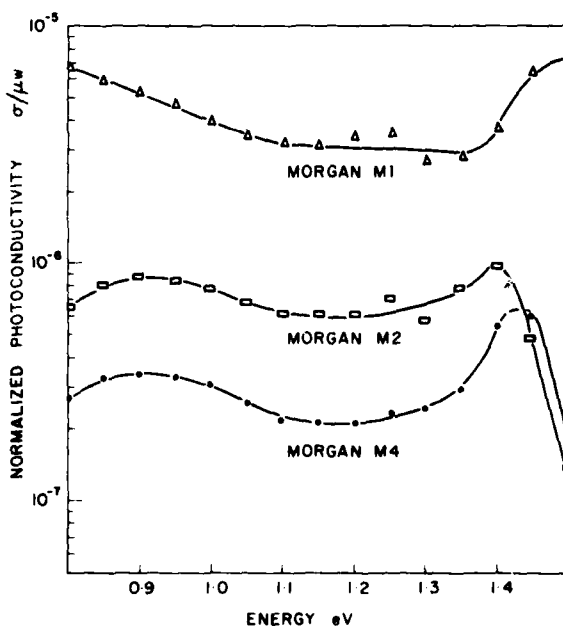


Figure 19. Photoconductive response of three Morgan Cr-doped SI GaAs substrates.

Figure 20 is a replot of the photoconductive response of two Laser Diode substrates, one nominally O-doped (LD-3325) and the other Cr-doped (LD-9918).

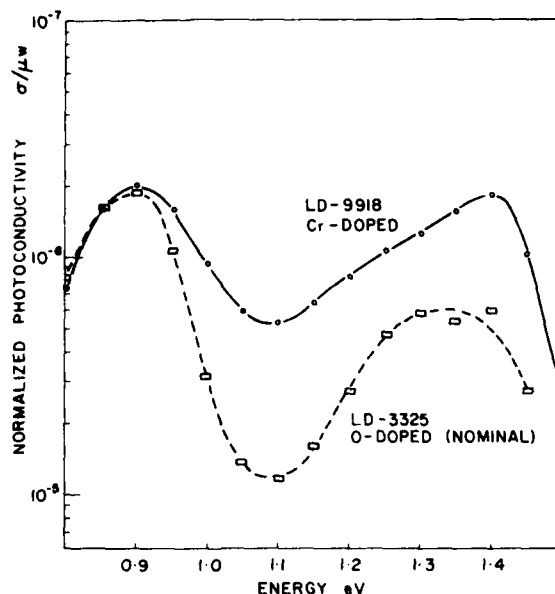


Figure 20. Nominally O-doped and Cr-doped SI GaAs substrates. Note similar photoconductive response.

The responses are essentially similar. This is consistent with SSMS measurements which show Cr in both substrates.

We conclude that photoconductivity measurements can be used to nondestructively detect the presence of Cr in most SI GaAs substrates. The only discrepancy observed was the Sumitomo sample which was specified by the vendor as O-doped, but SSMS detected a significant amount of Cr. It is likely that other deep states can be resolved by extending the measurement to lower temperatures and photon energy. As yet, there is no correlation between other substrate properties such as ability to withstand high-temperature ($\geq 750^\circ\text{C}$) anneals and photoconductive response.

2. High-Resistivity Epi Layers on SI GaAs Substrates

Application of this method directly to the in situ detection of Cr in thin epi layers grown on SI GaAs substrates is not straightforward, however. Measurements of the optical absorption coefficient of Cr-doped material (Fig. 21) showed a negligible increase at 0.9 eV. Thus, the material remains optically transparent, and any increase in photoconductivity could come from the Cr-doped substrate as well as the buffer layer. In view of the relative thickness, it seems unlikely that the effects of the buffer layer at 0.9 eV would be seen at all.

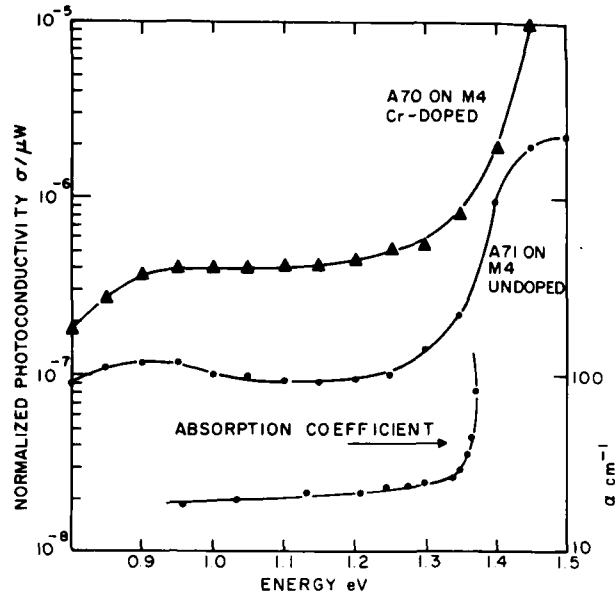


Figure 21. Photoconductive response of high-resistivity epitaxial layers on SI GaAs substrate (M4). Absorption coefficient plot also shown.

On the other hand, band-edge illumination is absorbed very rapidly with depth because of the large value of the absorption coefficient. Behavior of the photoconductive spectral response for the substrates tested was always similar. Conduction increased near the band edge and then dropped off as the photon energy increased (see Fig. 20). This is interpreted as being due to a large value of the surface recombination velocity S . As the generated hole-electron pairs are confined to the surface, the photoconductive is seen to decrease. Figure 21 shows the room-temperature photoconductive spectral response for two SI epi films on the Morgan M4 substrate. The characteristic dip above the band edge seen for the substrate was not observed for either the undoped or Cr-doped samples indicating a lower value of S in the epi material. It is not known, however, whether this fact can be used to advantage in material characterization.

The behavior of the absorption coefficient α makes near-band-edge radiation a useful probe of variable depth into the sample. It is likely that photo-Hall measurements with near-band-edge illumination will allow one to electrically separate the effect of transport in the epitaxially grown high-resistivity

layers from transport in the bulk-grown SI GaAs substrate. However, the significance of such photo-Hall data and their correlation to eventual device performance is as yet unknown.

C. RESISTIVITY MEASUREMENTS

Another basic transport study was the measurement of the resistivity of several SI GaAs substrates and substrate epilayer structures as a function of temperature. Extensive measurements of the resistivity-temperature characteristics of GaAs have been reported by investigators at Rockwell International [7]. The measurements reported here are similar but on substrates from different vendors.

The resistivity measurements were made using square van der Pauw samples with Sn contacts as described earlier. Similar instrumentation was used. Where possible, the Hall mobility was computed assuming single-carrier transport. The temperature range under investigation was from 17 to 170°C. The Sn ohmic contacts were covered by silver epoxy to prevent oxidation and subsequent powdering at elevated temperatures. These measurements were carried out in the dark to avoid effects of photogenerated carriers.

In order to meaningfully interpret the resistivity-temperature characteristic, it is desirable to remove the implicit temperature dependence of the density of states and the various donor and acceptor energy levels. The procedure used by Zucca has been employed [7]. The function $\rho T^{1.5}$ has been plotted as a function of $1/T'$. Since the density of states is proportional to $T^{1.5}$, plotting $\rho T^{1.5}$ removes this implicit temperature dependence. T' is a modified temperature given by:

$$T' = T \frac{E_g(300K)}{E_g(T)} \quad (1)$$

where $E_g(T)$ is the energy gap at a temperature of T (Kelvin). This assumes that relative energies of the impurity levels are proportional to the energy gap. Instead of correcting energies for thermal variations, the correction is made on kT since the energy differences are always divided by kT in expressions for resistivity [7].

The energy gap of GaAs as a function of temperature was determined by the expression of Panish and Casey [12]:

$$E_g(T) = 1.522 - 5.8 \times 10^{-4} \frac{T^2}{T + 300} \text{ eV} \quad (2)$$

where T is the temperature in degrees Kelvin. The parameter $1000/T'$ is plotted as a function of $1000/T$ in Fig. 22 over the temperature range of 300 to 500 K. In this temperature range we can thus approximate the value of $1000/T'$ by the following expression:

$$\frac{1000}{T'} = \frac{1100}{T} - 0.33 \quad (3)$$

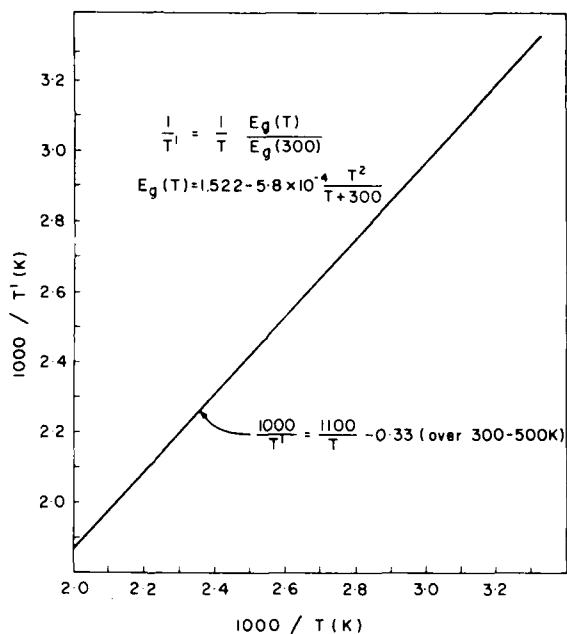


Figure 22. Plot of $1000/T'$ as a function of $1000/T$.

Figure 23 is a plot of $\rho T^{1.5}$ as a function of $1000/T'$ for two samples from a lot of Morgan M4 substrates. A least square fit to the data is also shown.

12. M. B. Panish and H. C. Casey, Jr., "Temperature Dependence of the Energy Gap in GaAs and GaP," J. Appl. Phys. 40, 163 (1969).

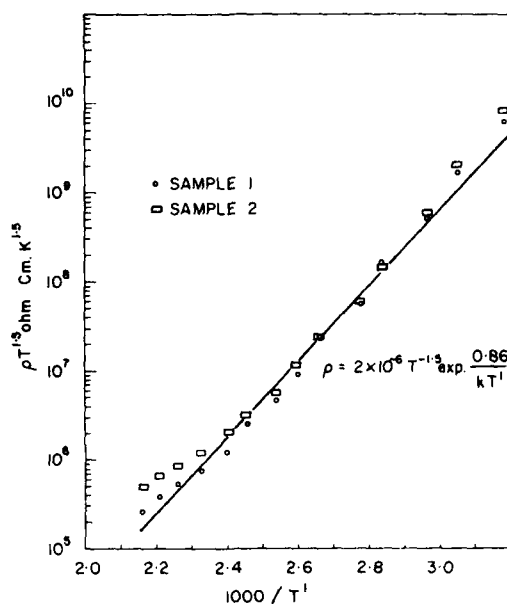


Figure 23. $\rho T^{1.5}$ as a function of $1000/T'$ for Morgan M4 substrates.

Recall that this substrate has a Cr concentration of 0.1 ppma ($2.2 \times 10^{15} \text{ cm}^{-3}$). From the least square fit to the data, we can write the resistivity ρ as:

$$\rho = 2 \times 10^{-6} T^{-1.5} \exp \left(\frac{0.86}{kT} \right) \quad (4)$$

The resistivity is thus thermally activated with an activation energy of about 0.86 eV. This assumes that the mobility μ is independent of temperature over this temperature range. This assumption is justified later.

Let us now compare this result to the measurements of Zucca for the low Cr ($5 \times 10^{15} \text{ cm}^{-3}$) case quoted in Ref. 7. Zucca found that for the particular crystal under consideration:

$$\rho = 1.08 T^{-1.5} \exp \left(\frac{0.72}{kT} \right) \quad (5)$$

Zucca interprets this using the deep donor-deep acceptor model as containing an N_d/N_a of 14 and $E_c - E_d$ of 0.72 eV which corresponds to the 0 level in GaAs. For the Morgan substrate and the curve fit to the resistivity data, Eq. (4), we compute $E_c - E_a$ to be 0.86 eV which is in reasonable agreement with the depth of the Cr level of 0.84 eV reported in the literature [13]. Assuming an average

13. H. J. Stocker and M. Schmidt, "A Study of Deep Impurity Levels in GaAs," J. Appl. Phys. 47, 2450 (1976).

mobility of $3000 \text{ cm}^2 \text{V}^{-1} \text{s}^{-1}$ and a degeneracy factor g_a of unity and using Eq. (12) of Ref. 7, we compute N_a/N_d to be 1.5.

Figure 24 is a plot of the Hall mobility of sample M4 from measured data assuming single-carrier transport. The Hall constant was found to be well behaved and did not change sign over the measured temperature range of 300 to 500 K. Thus our assumption of a constant mobility of $3000 \text{ cm}^2 \text{V}^{-1} \text{s}^{-1}$ is a reasonable assumption for the calculation of N_a/N_d . Also note that this mobility-temperature characteristic is very similar to those reported by Lin for GaAs:Cr [14].

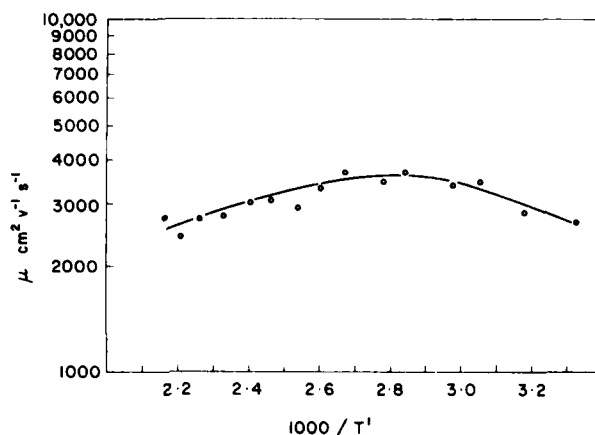


Figure 24. Hall mobility as a function of $1000/T'$ for Morgan M4 substrates.

Figure 25 shows a similar plot of $\rho T^{1.5}$ as a function of $1000/T'$ for a Nikkei-Kako* (NK), Cr-doped substrate from dark conductivity measurements. A straight line fit to these data indicates an activation energy of the order of 0.74 eV which is close to the 0 level in GaAs (0.72 eV). However, it was not possible to measure Hall mobility because the Hall voltages were very small. Thus, the resistivity may be controlled by two levels, a deep donor and a deep acceptor. It may therefore be incorrect to associate the 0.74-eV number with

14. A. W. L. Lin, "Photoelectronic Properties of High Resistivity GaAs:O and GaAs:Cr Single Crystals," Ph.D. Thesis, Stanford University, 1975.

*Nikkei-Kako Company, Tokyo, Japan.

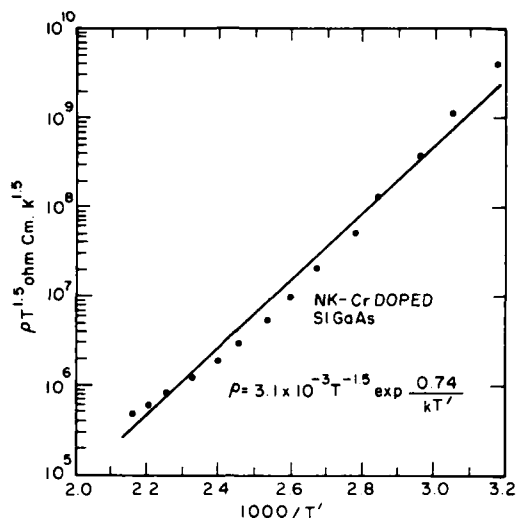


Figure 25. $\rho T^{1.5}$ as a function of $1000/T'$ for NK SI GaAs substrate.

oxygen and a more complex curve fit procedure as discussed by Zucca may be necessary [7]. In fact, other NK samples were found to be p-type at 27°C and became n-type above 50°C indicative of mixed conduction.

Note that for Morgan substrates, the activation energy of 0.86 roughly correlates with the broad peak at 0.9 eV seen in photoconductivity measurements.

Figure 26 shows the $\rho T^{1.5}$ - $1000/T'$ characteristics of the NK substrate repeated from the previous figure. The points, however, represent the data obtained from a dark conductivity measurement carried out on an undoped epitaxial SI layer (D80) grown on an NK substrate. This undoped layer was grown using the $\text{AsCl}_3/\text{GaH}_3$ process. The layer thickness was 6 μm and the substrate thickness 318 μm . Note that the data points for the composite structure fit reasonably well to the substrate characteristic. For these layer thicknesses, we can compute that ρ (buffer) $\geq 0.2 \rho$ (substrate) if we assume that the effect of the total layer resistance has to be about 10 times the substrate resistance to be unobservable. This puts a lower bound of $5 \times 10^5 \Omega\text{-cm}$ for the buffer layer resistance, which is adequate for device applications.

D. SECONDARY ION-MASS SPECTROSCOPY (SIMS)

Recent results on the use of SIMS for measuring the atomic profiles of impurities in GaAs have been very encouraging. We have investigated Cr profiles

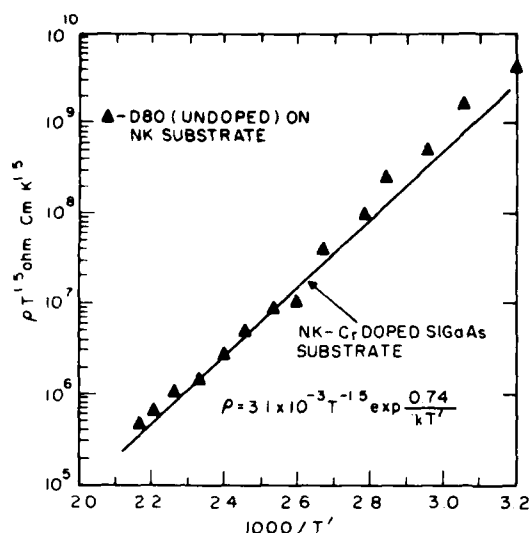


Figure 26. $\rho T^{1.5}$ data points for D80 on NK substrate. The straight line is the characteristic of the substrate alone.

in Cr-doped epi-layers and other test structures using SIMS. Measurements were made at Charles Evans and Associates* and RCA using an O^+ primary ion beam.

Figure 27 shows the ^{52}Cr profile measured using SIMS for wafer B307 grown by the $\text{AsH}_3/\text{Ga}/\text{HCl}/\text{H}_2$ process. A Cr-doped layer followed by an undoped layer was grown. After growth of the Cr-doped layer, growth was stopped to flush out the doping gas by stopping HCl flow. Growth of the undoped layer was started by re-establishing HCl flow. SIMS shows a significant accumulation of Cr at the interface of the undoped and Cr-doped layers. Note also the decreasing trend in Cr concentration in the undoped layer.

Figure 28 shows the ^{52}Cr profile in B309, which has only a Cr-doped layer. Figure 29 shows the ^{52}Cr profile in a test structure wherein an undoped layer was grown prior to the Cr-doped layer. Note that the Cr concentration in the undoped layer is lower than that in the Cr-doped layer, but that there is still a significant amount of Cr in the undoped layer. It is not clear whether this concentration is actually present or represents the background Cr concentration in the SIMS machine. Again, note the pile-up of Cr at the interface.

Figure 30 shows the ^{52}Cr and ^{80}Se profile of B371. This wafer had a 2- μm Se-doped n-layer grown on 6 μm of Cr-doped buffer layer. Again, growth was stopped after the Cr-doped layer. Note the excellent ^{80}Se profile indicating

*Charles Evans and Associates, San Mateo, CA.

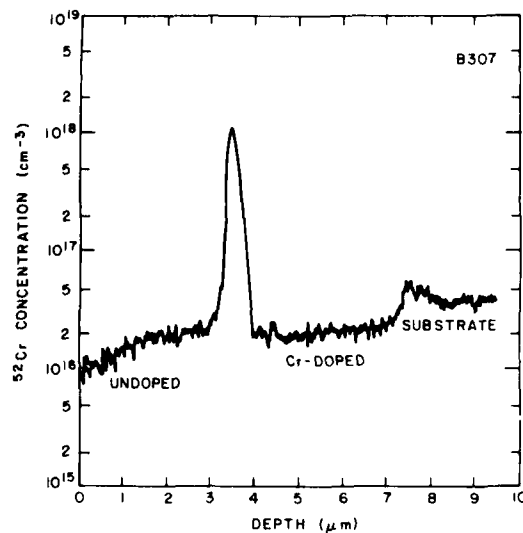


Figure 27. SIMS profile of ^{52}Cr showing pile-up at interface. Note decreasing ^{52}Cr trend in undoped layer.

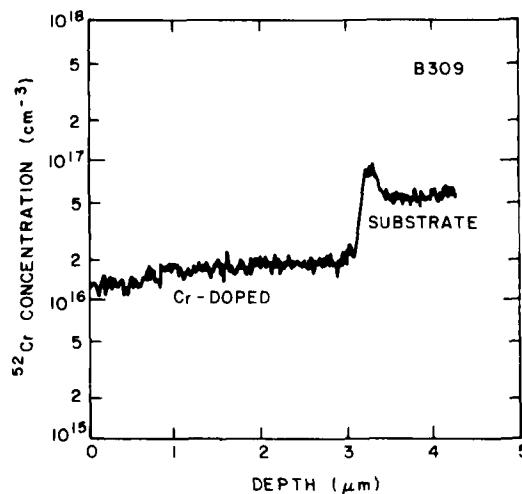


Figure 28. SIMS profile of Cr-doped epitaxial layer. There is some pile-up at interface.

good control on n-layer dopant incorporation. Note, however, that SIMS shows a 10^{16} cm^{-3} Cr concentration in the n-layer and the accumulation of Cr at the interface. The carrier profile ($N_D - N_A$) measurement indicates a uniformly doped 2- μm , $2 \times 10^{16} \text{ cm}^{-3}$ layer. There is a discrepancy between the effective donor

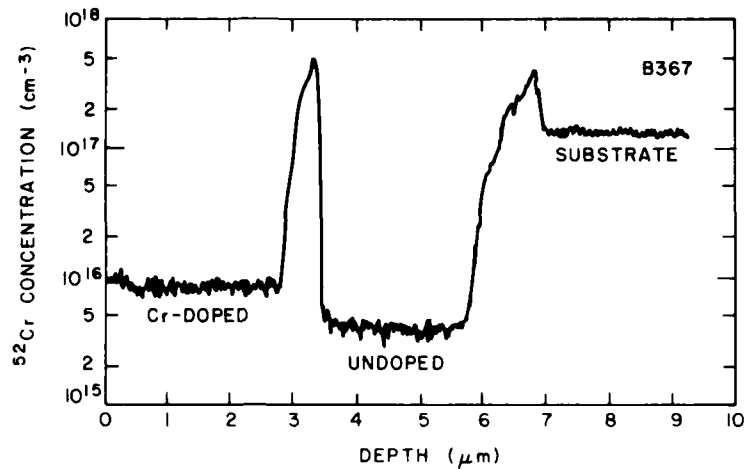


Figure 29. SIMS profile of substrate-undoped Cr-doped structure. Note Cr pile-up at interface.

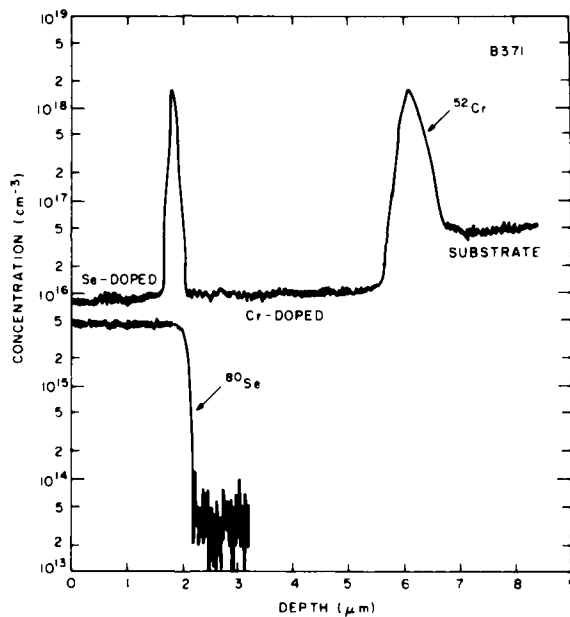


Figure 30. ^{52}Cr and ^{80}Se SIMS profiles measured with primary O and Cs beams, respectively. Note Cr pile-up at interface and sharp Se profile.

concentration and ^{80}Se concentration which may be due to the calibration uncertainties in the SIMS measurement. Van der Pauw measurements on the n-layers show $\mu_{300} = 6048 \text{ cm}^2 \text{V}^{-1} \text{s}^{-1}$ and $\mu_{77} = 18,955 \text{ cm}^2 \text{V}^{-1} \text{s}^{-1}$ indicating low compensation in spite of Cr accumulation and the apparent 10^{16} cm^{-3} in the n-region.

Figure 31 shows the ^{80}Se profile of an n^+ -n-n(buffer)-SI substrate wafer. The buffer layer was Cr-doped. Note the penetration of Se into the buffer layer. The n^+ -layer is only $0.25\text{ }\mu\text{m}$ thick. It was established that this apparent Se penetration was not an artifact. This is in agreement with our observation of conducting "knees" on resistivity profiles whenever an n^+ -layer is grown (see Fig. 4). Figure 30 confirms that no Se penetration occurs into the buffer layer when an n^+ -layer is not grown. The mechanism of this phenomenon is not understood.

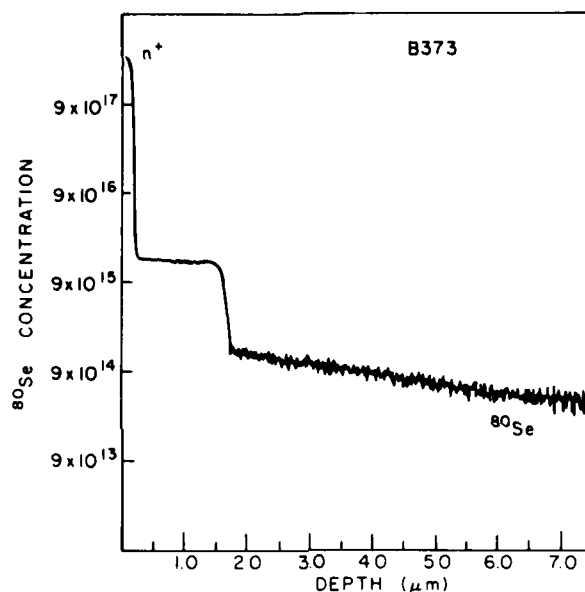


Figure 31. SIMS profile of ^{80}Se in an n^+ -n-n(buffer)-SI GaAs wafer showing Se penetration into the Cr-doped buffer layer.

Figures 32 to 34 show ^{52}Cr profiles of wafers grown by the $\text{AsCl}_3/\text{Ga}/\text{H}_2$ process. In this series of wafers, the growth was not stopped in the middle, and about $10\text{ }\mu\text{m}$ of the substrate in situ etched before start of Cr-doped layer growth. Note the abrupt interface between the substrate and the epi-layer with no evidence of the Cr pile-up.

In order to differentiate between Cr added deliberately from the gas phase and Cr out-diffusion from the substrate, test samples were grown on nominally Cr-free n^+ substrates. First, 3 to $4\text{ }\mu\text{m}$ of n-layers were grown to get away from the n^+ substrate; then, a high-resistivity layer followed by an n-layer

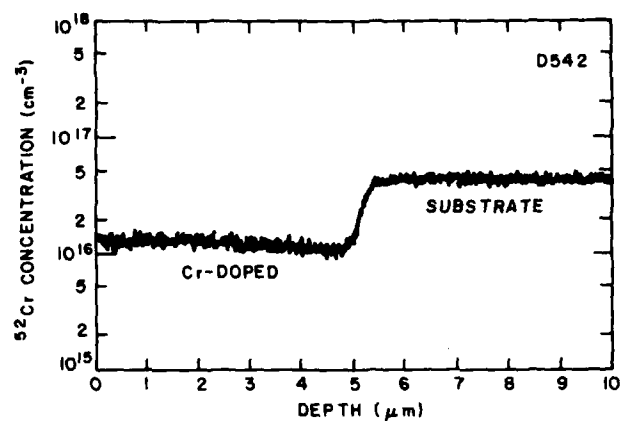


Figure 32. SIMS profile of Cr-doped layer grown in $\text{AsCl}_3/\text{Ga}/\text{H}_2$ system. No growth interruption, no Cr pile-up.

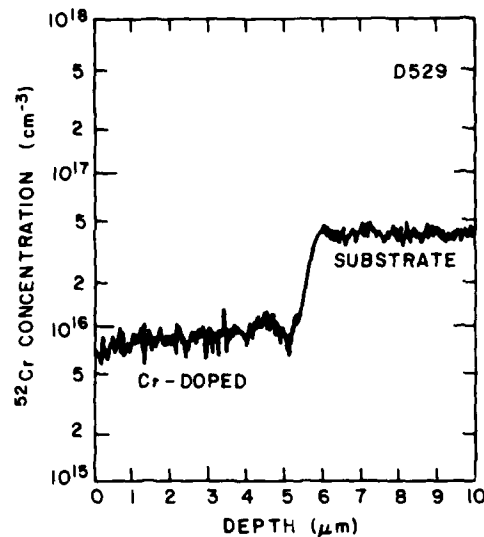


Figure 33. Another example of a good buffer layer.

was grown. The carrier profile was then measured using Al Schottky-barrier diodes. In Fig. 35, the effect of Cr-doping is clearly visible as an over an order of magnitude decrease in carrier concentration. Growth was continuous with no interruption. SIMS measurement, however, did not provide a Cr profile since the instrument background at the time of measurement was 10^{16} cm^{-3} . Note that no Cr spikes were observed.

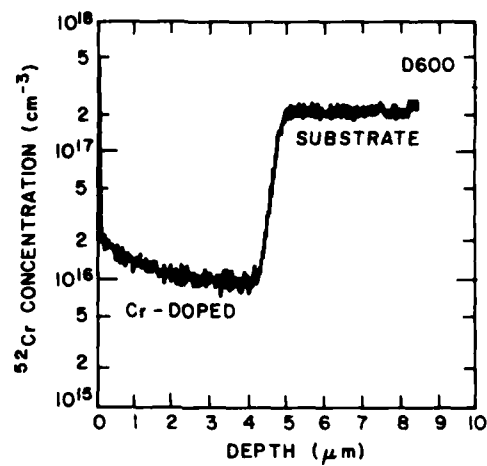


Figure 34. Cr-buffer layer with nonuniform Cr concentration.

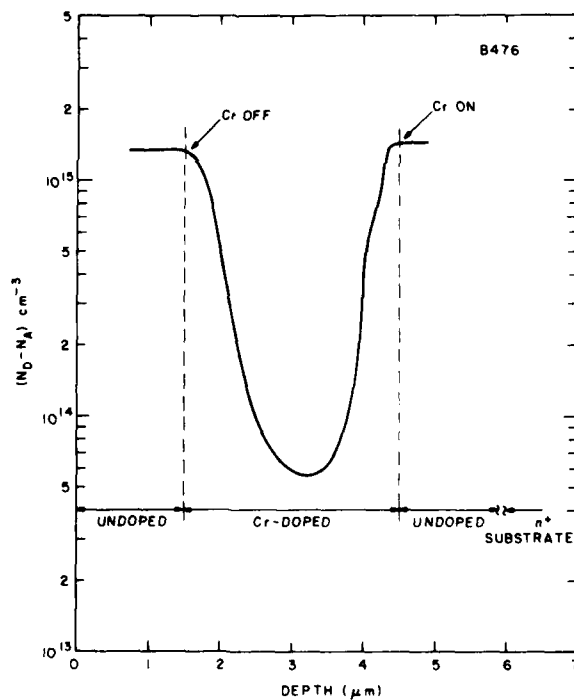


Figure 35. Carrier profile of Cr-doped layer grown on n^+ substrate. SIMS could not detect Cr in middle layer indicating a Cr concentration less than 10^{16} cm^{-3} .

SECTION IV

HIGH-ENERGY (UP TO 1.2 MeV) ION IMPLANTATION

One of the major reasons for the development of a technology for the epitaxial growth of SI GaAs is to use this layer as starting material for ion implantation. If high-quality, high-resistivity epitaxial layers can be repeatedly grown on a variety of commercial bulk-grown SI substrates, more reproducible results can be obtained by ion implantation. One of the tasks in this program is the investigation of the implantation of ^{28}Si up to an energy of 1.5 MeV. This implantation effort is supported in part with RCA funds and by an Office of Naval Research supported effort (N00014-78-C-0367).

In this section, the progress made in obtaining and implanting high-energy (up to 3 MeV) ion beams will be reviewed. Beams of ^{11}B and ^{28}Si have been produced and implanted into both silicon and GaAs substrates. The profiles and range statistics of these implants have been analyzed using SIMS (secondary ion-mass spectroscopy) analysis, and based on the information obtained, uniformly doped ^{28}Si profiles $\sim 1\text{ }\mu\text{m}$ deep have been produced in GaAs using multiple implants. This section discusses the production of implanted profiles, dopant activation analyses, and mobility measurements on implanted (single or multiple) and annealed GaAs wafers.

A. HIGH-ENERGY Van de GRAAFF FOR HEAVY ION IMPLANTATION

The Van de Graaff machine used for the high-energy implant experiments was built by High Voltage Engineering Corp* and was originally designed to produce proton beams at 3 MeV and $\sim 1\text{ mA}$. The machine was originally equipped with a duo-plasmatron source and operated with a cumbersome end-station (for wafer implantation) attached to the 25° magnet port.

To produce and implant heavy ion beams, two major modifications were made to the Van de Graaff machine. First, the duo-plasmatron source was replaced with a cold-cathode-discharge heavy ion source, and the cold cathode source was in turn replaced with a rf-excited plasma source. Both the extraction optics on the machine and the high operating pressures required by the available cold cathode source made it unusable, and hence the final selection of

*High Voltage Engineering Corp, Burlington, MA.

the rf source. The second major modification to the Van de Graaff machine was the construction of a new beam line attached to the 15° port rather than the 25° port of the analyzing magnet. Using the 15° port, a mass-energy (at mass x energy in MeV) product of ~33 could be achieved with the available analyzing magnet. The new beam line that was constructed contained x-y sweep plates and terminated in an end-station which holds a single wafer at a time. The implant area is ~2.54 cm by 2.54 cm. During the implant, the normal to the wafer was inclined at an angle of 7° relative to the direction of the incident beam. The vacuum in the beam line and end-station during the implant was maintained in the 10⁻⁶-Torr region.

B. CALIBRATION IMPLANTS USING ¹¹B⁺ BEAM

The first experiments were performed using BF₃ as a source gas in the ion source and implanting ¹¹B⁺ ions into a silicon substrate. These conditions were chosen because the spectrum of BF₃ (i.e., the amplitude of the various ion components extracted from the source plotted as a function of the current in the analyzing magnet) is well known and has a distinctive set of ¹⁰B⁺, ¹¹B⁺ peaks. The mass of the boron ion is also relatively small so the machine could be exercised at higher energies. The mass-energy product (atomic mass x energy in MeV) for the machine is ~33. ¹¹B in silicon was also selected for the first tests because of the ability of SIMS analysis to readily measure the profile.

Figure 36 shows a SIMS plot of a 1-MeV ¹¹B implant that was made on the FEC* machine compared with a 60-keV ¹¹B implant that was made on the Princeton Labz implanter. The scanned area in the newly constructed beam line is 2.54 cm x 2.54 cm and all portions of the system performed well during the implant.

To test the endurance of the machine for higher level implants, a series of implants was made at progressively higher energies as shown in the SIMS plots given in Fig. 37. Each implant required approximately 45 min of implant time using a beam current of ~4 µA. These implants were carried out over a two-day period of essentially continuous running. Terminal overheating problems were experienced during these long tests, and suitable corrections were made

*Fusion Energy Corporation, Princeton, NJ.

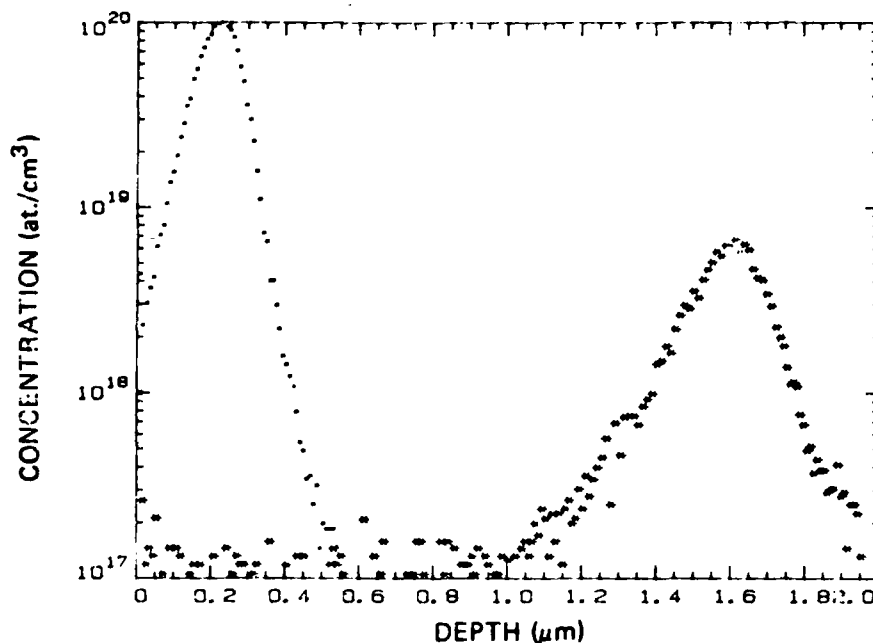


Figure 36. SIMS plots of a 60-keV ^{11}B implant performed on the Laboratories machine and a 1-MeV ^{11}B implant performed on the FEC Van de Graaff implanter.

to some of the cooling systems. Beam currents as high as $8\text{ }\mu\text{A}$ of ^{11}B were obtained, but lower values were used to prevent excessive end-station and wafer heating. (At 2 MeV and $8\text{ }\mu\text{A}$, the average incident power density on target is $\sim 2.5\text{ W/cm}^2$.)

The measured value of the range R_p for the series of ^{11}B implants is given in Fig. 38. The value of the implant energy was calibrated by bombarding a lithium target with high-energy protons (obtained from the source operating with SiH_4). A resonant interaction occurs between the lithium target and the proton beam at 1.88 MeV which produces detectable neutrons. The machine is calibrated by comparing the reading on the machine energy dial with the occurrence of neutrons being emitted from the lithium target.

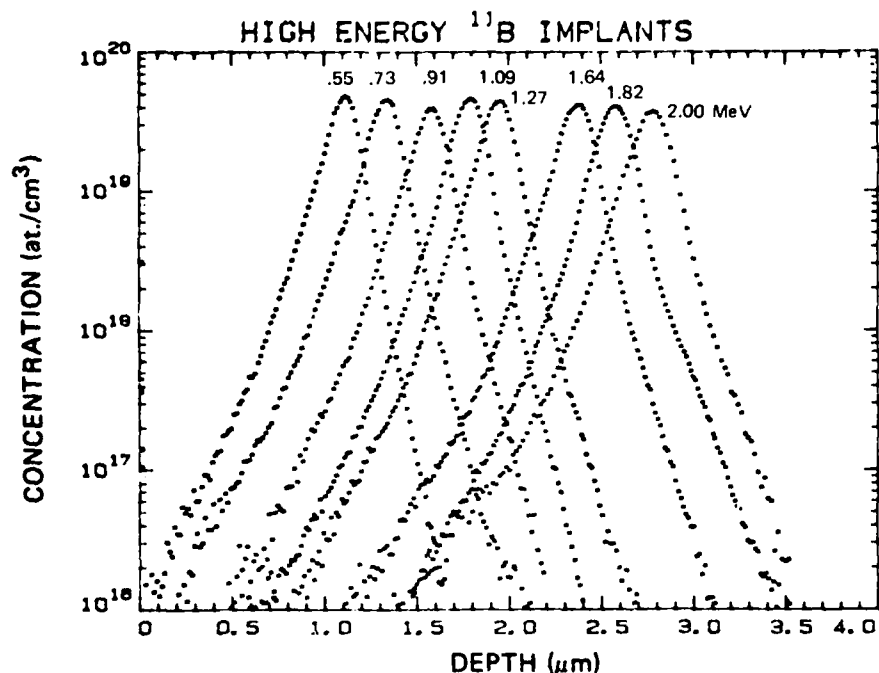


Figure 37. SIMS plots of a group of samples implanted with increasing energies using the FEC Van de Graaff implanter.

C. IMPLANTATION OF $^{28}\text{Si}^+$ INTO GaAs

1. Calibration

Having demonstrated with ^{11}B the ability of the Van de Graaff machine to produce heavy ion beams, we changed the source gas from BF_3 to SiH_4 ; beams of $^{28}\text{Si}^+$ were produced and implanted into GaAs substrates. The results of the first test implants made at 600 keV are shown in the SIMS plot given in Fig. 39. These results indicate that the magnet was properly adjusted to produce a Si beam.

The results of a series of implants made at a number of different implant energies ranging from 40 keV to 1.2 MeV are shown in Figs. 40 and 41. The lower range implants (40 to 280 keV) were performed on the implant machine located at the Princeton Laboratories and the higher range implants (0.7 to 1.2 MeV) were performed on the Van de Graaff implanter.

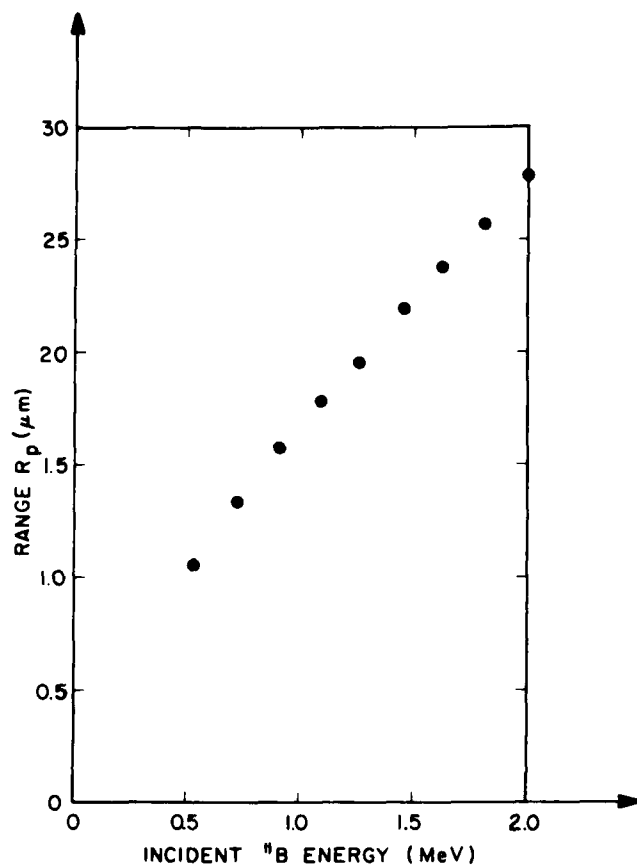


Figure 38. Measured value of the range R_p for the series of ^{11}B implants.

Figure 42 shows a set of implants made at different dose levels. There is a discrepancy between the dose specified and the dose actually observed in the wafer. This error could be caused by inaccuracies in the dose measurement system or perhaps could be due to the implantation of $^{28}\text{N}_2^+$ along with $^{28}\text{Si}^+$. A similar dose discrepancy has been observed in the multiple-implant profile (described in the next section) and work is underway to resolve this discrepancy.

It is evident from Fig. 41 that the profiles are not Gaussian in shape but are noticeably skewed toward the wafer surface. This is not unexpected for high-energy implants since the conventional LSS theory, which predicts Gaussian

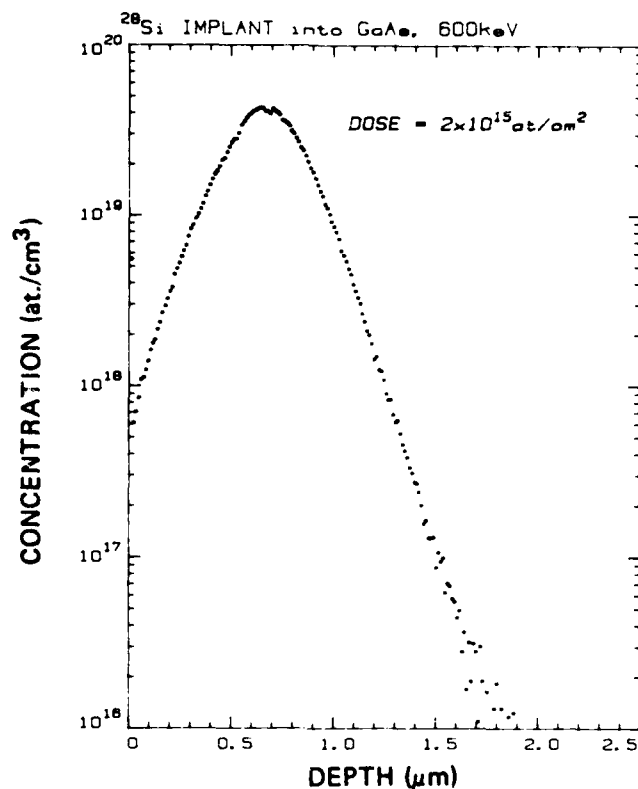


Figure 39. SIMS plot of the first $^{28}\text{Si}^+$ implant into a GaAs substrate using the Van de Graaff machine.

profiles, i.e., distributions with all moments greater than the second moment equal to zero, is known to be a low-energy approximation. A theory, developed by the statistician Karl Pearson [15,16] and applied to ^{11}B implants into Si at energies up to 800 keV by Hofker [17], makes use of the first four experimental moments to produce fits to the observed profile data. From these calculations, statistical information, such as the range R_p and straggle ΔR_p , can be obtained for skewed data.

15. M. G. Kendall and A. Stuart, The Advanced Theory of Statistics, (Charles Griffin, London, 1958), Vol. 1, p. 148.
16. W. P. Elderton, Frequency Curves and Correlation, (Cambridge University Press, 1953), 4th ed.
17. W. K. Hofker, Implantation of Boron in Silicon, Philips Research Supplements, 1975, No. 8.

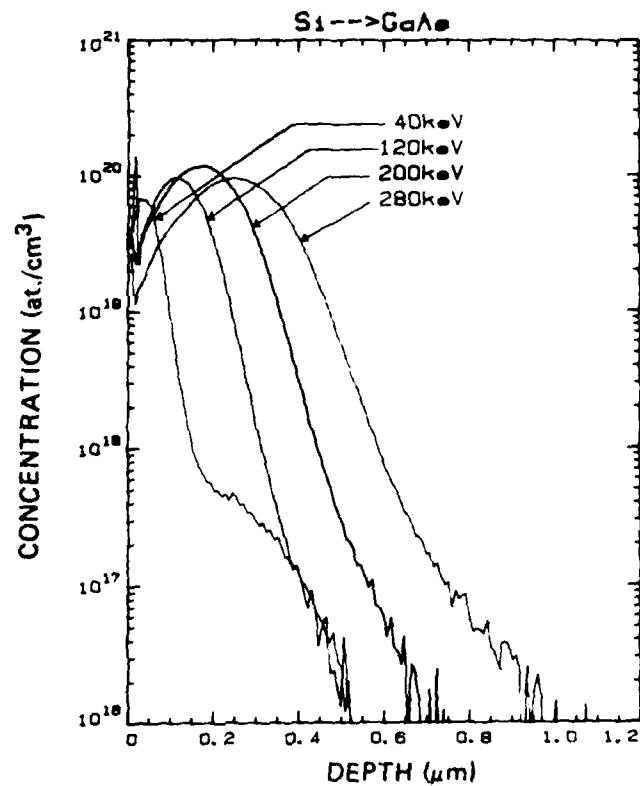


Figure 40. SIMS profiles of implants made at energies of 40, 120, 200, and 280 keV.

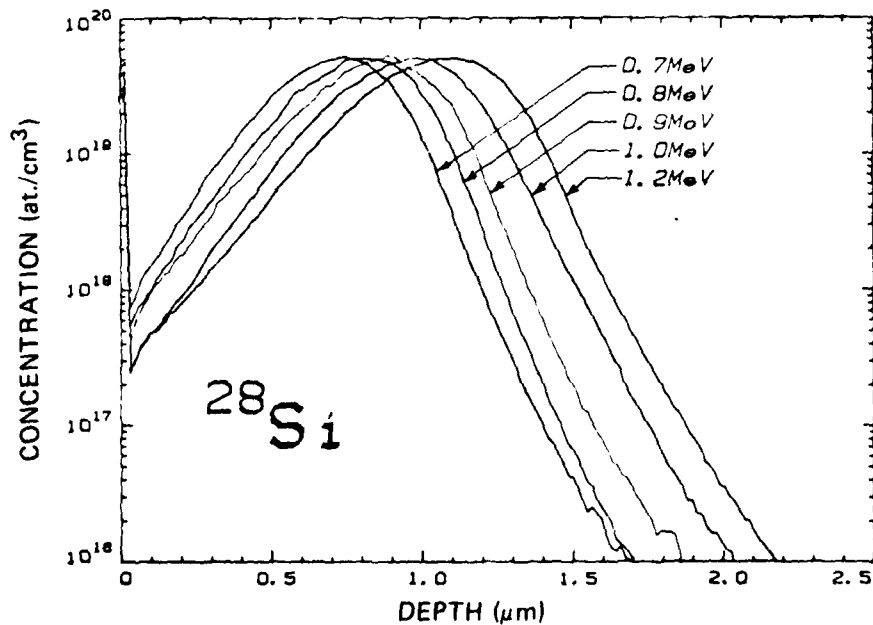


Figure 41. SIMS profiles of implants made at energies of 0.7, 0.8, 0.9, 1.0, 1.2 MeV.

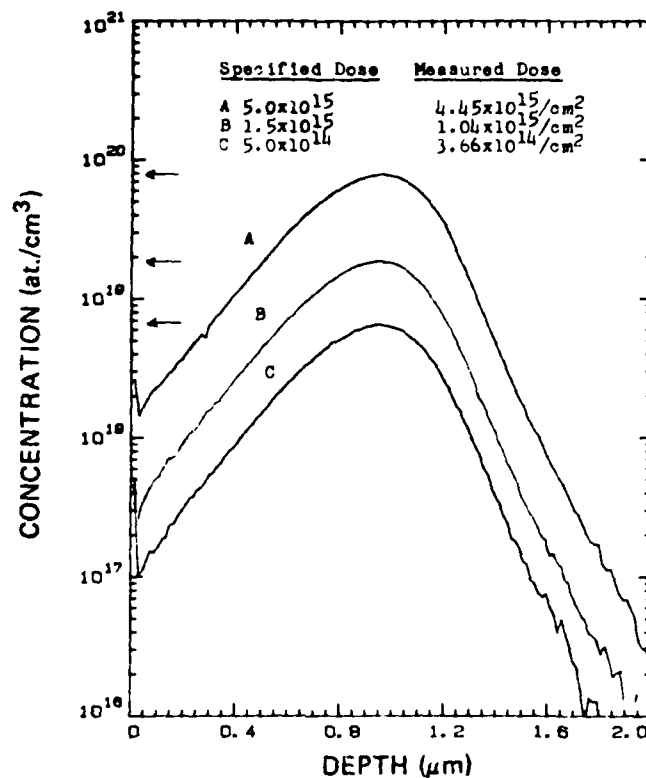


Figure 42. SIMS plots of 1-MeV ^{28}Si implants made into GaAs at different dose levels.

The results of curve fitting to the experimental data, based on the first four experimental moments, are shown in Figs. 43 to 45. Figures 43 and 44 show both a log and a linear plot of the experimental and calculated data using the formula described by Elderton [16]. Figure 45 shows a composite plot of the curves corresponding to the experimental data given in Fig. 41. Figure 46 shows a reduction of the data to R_p and ΔR_p values corresponding to LSS Gaussian reduction techniques and first-four-moment Pearson techniques. It should be noted that the crossovers of the computed curves in Fig. 45 and the poor fit of the computed curves to the extended tails at both the shallow and deep portions of the curve indicate that care must be taken to ensure that excessive channeling is not present. To test this hypothesis, experiments are planned which involve implantation into amorphized substrates.

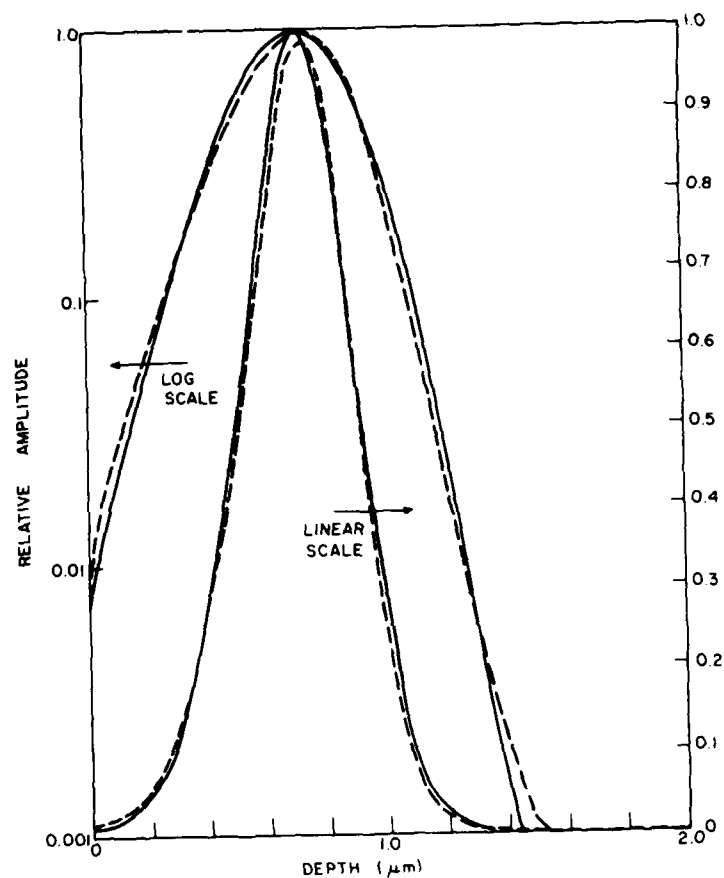


Figure 43. Curve-fitting to experimental data, 0.7-MeV $^{28}\text{Si}^+$ into GaAs.

2. The Formation of Flat Profiles of Si in GaAs

Implant conditions have been worked out for forming $\sim 1\text{-}\mu\text{m}$ -deep layers of Si in GaAs with nearly constant doping throughout the layer. Five implants, ranging from 40 to 900 keV, are used to construct the layer. Table 3 shows the calculated implant conditions for achieving flat profiles at three different impurity concentration levels: 1×10^{20} at./cm³ for sample H23, 2.5×10^{19} at./cm³ for sample H24, and 1×10^{19} at./cm³ for sample H25.

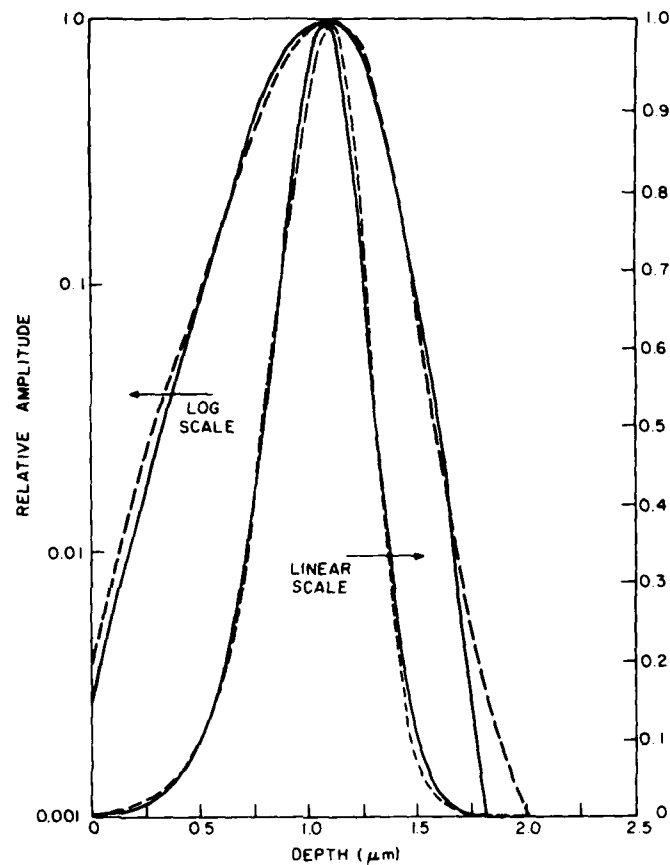


Figure 44. Curve-fitting to experimental data, 1.18-MeV $^{28}\text{Si}^+$ into GaAs.

A comparison of the calculated plot* and the actually measured SIMS profile is given in Fig. 47 (log plot) and Fig. 48 (linear plot). Actual implantation data are shown in Table 4. It is evident from the plot in Fig. 48 that a discrepancy exists between the calculated profile and the actual profile produced by the implant machine. Figure 49 shows a plot of the "flat profile" implemented at three different dose levels. Sample H25 is a gross example of the dose discrepancy.

*The calculated data were made using conventional LSS R_p and ΔR_p values because at the time of calculation, the Pearson four-moment-curve fits had not yet been investigated.

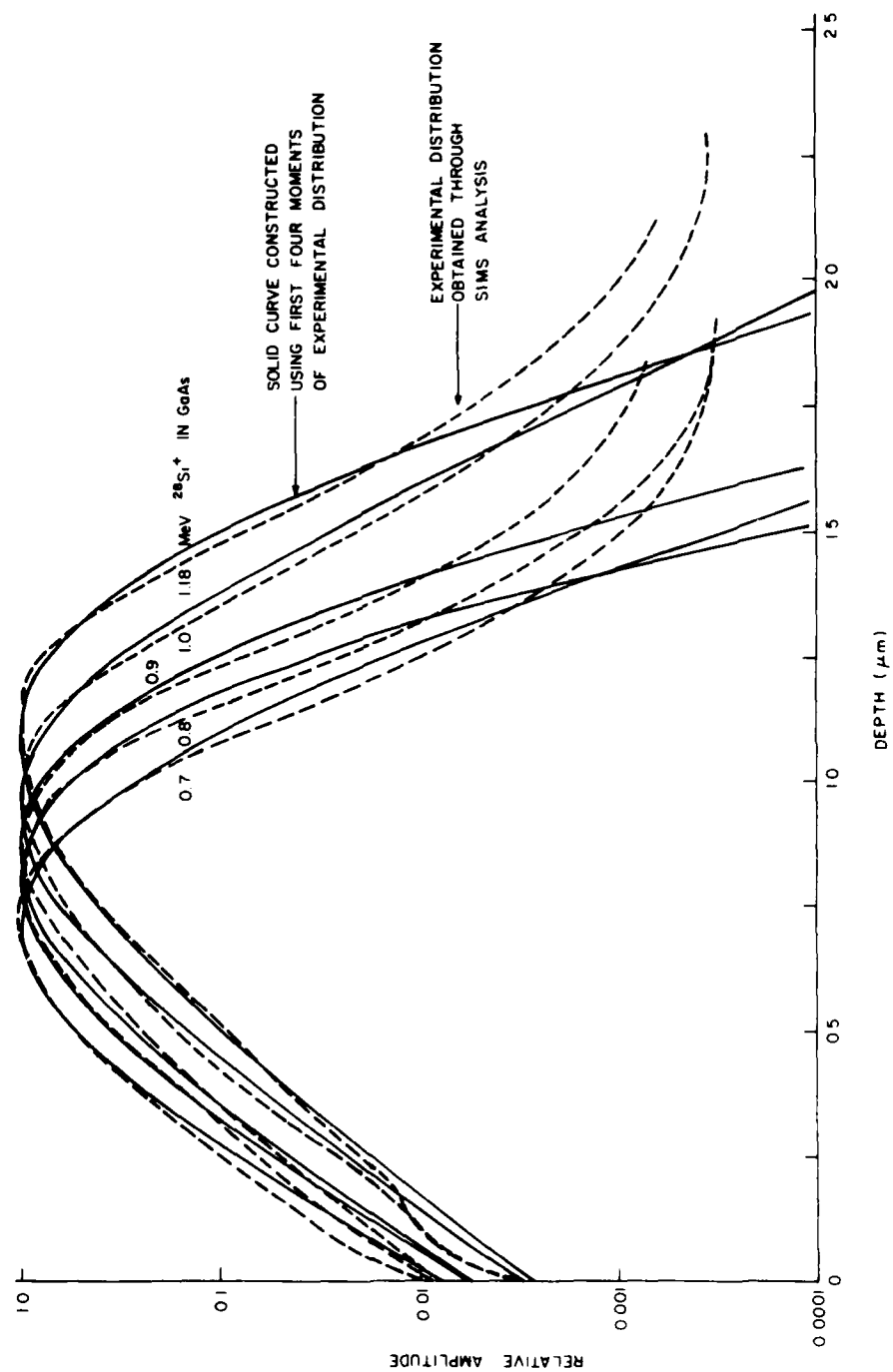


Figure 45. Composite plots of curves corresponding to the data given in Fig. 41.

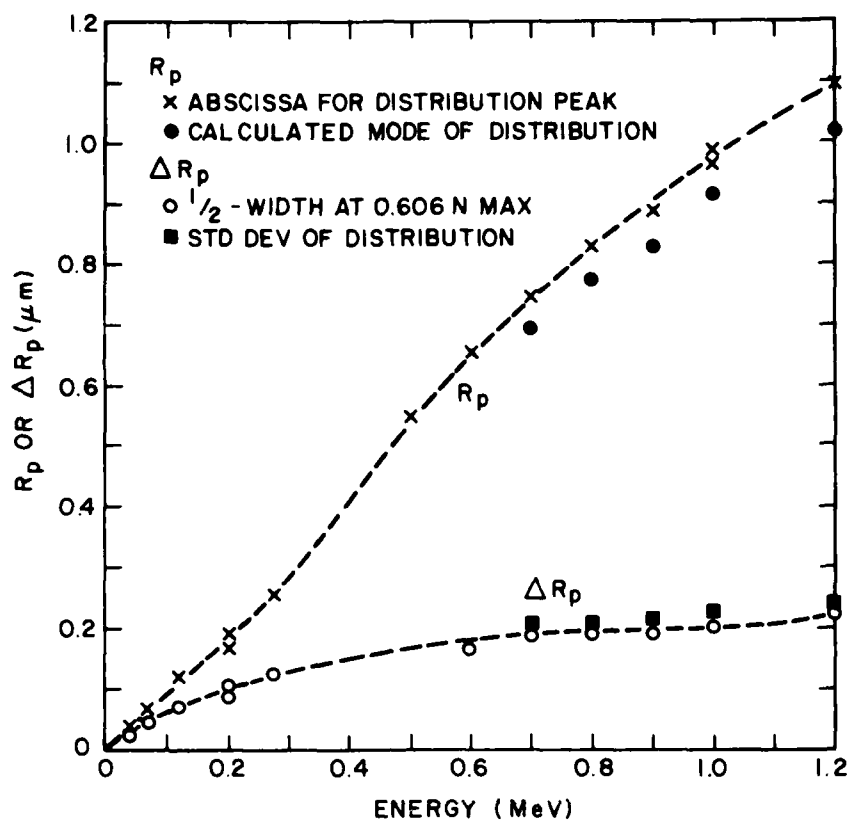


Figure 46. Reduction of data to R_p and ΔR_p values.

TABLE 3. CALCULATED MULTIPLE IMPLANT PARAMETERS

H23		H24		H25	
Energy (keV)	Dose (cm ⁻²)	Energy (keV)	Dose (cm ⁻²)	Energy (keV)	Dose (cm ⁻²)
40	4.7x10 ¹⁴	40	1.4x10 ¹⁴	40	4.7x10 ¹³
120	1.35x10 ¹⁵	120	4x10 ¹⁴	120	1.35x10 ¹³
280	1.9x10 ¹⁵	280	5.7x10 ¹⁴	280	1.9x10 ¹⁴
500	2.7x10 ¹⁵	500	8.2x10 ¹⁴	500	2.7x10 ¹⁴
900	4.3x10 ¹⁵	900	1.3x10 ¹⁵	900	4.3x10 ¹⁴

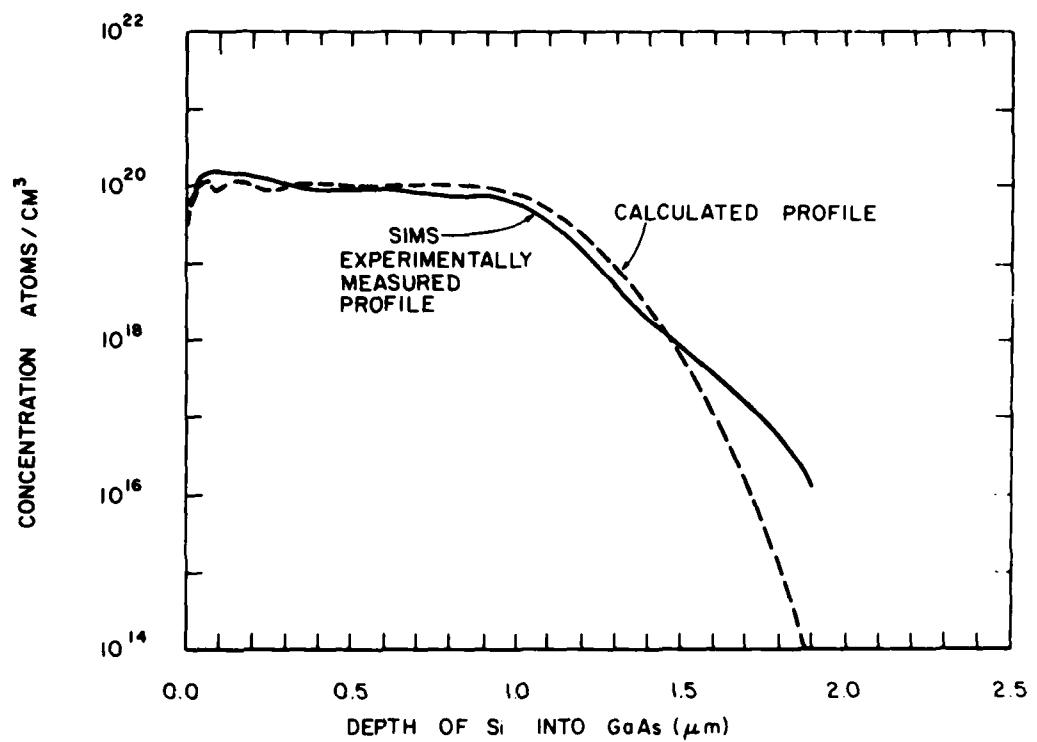


Figure 47. Comparison of calculated and actual SIMS profiles, log plot.

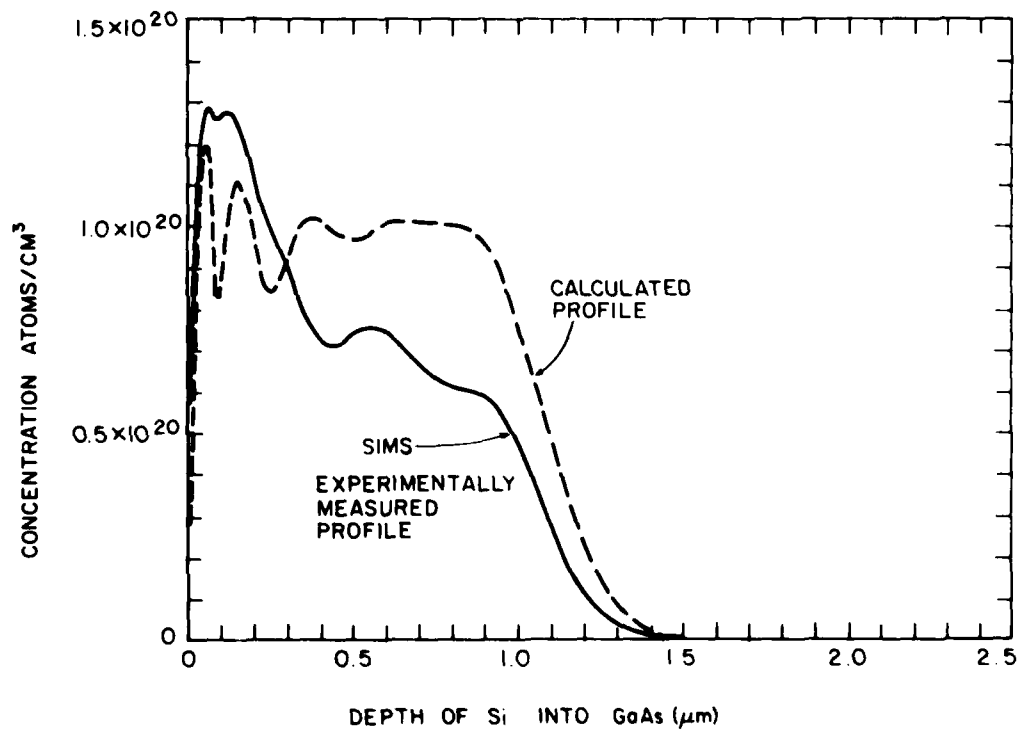


Figure 48. Comparison of calculated and actual SIMS profiles, linear plot.

TABLE 4. IMPLANT CONDITIONS FOR FLAT PROFILE OF Si IN GaAs

Parameter	Energy (keV)				
	40	120	280	500	900
R_p (μm)	0.0466	0.1375	0.3195	0.5500	0.8860
ΔR_p (μm)	0.0199	0.0600	0.1050	0.1500	0.1900
N_{max} (cm^{-2})	9.47×10^{19}	9.08×10^{19}	7.23×10^{19}	7.26×10^{19}	9.09×10^{19}
N_{dose} (cm^{-2})	4.70×10^{14}	1.35×10^{15}	1.9×10^{15}	2.73×10^{15}	4.33×10^{15}
Dose No.	303.6	872.0	1227	550.2	872.6
Scale	6E-6	6E-6	6E-6	6E-6	6E-6

$$\text{Area} = 24.29 \text{ cm}^2$$

(Labs machine)

$$\text{Area} = 7.56 \text{ cm}^2$$

(FEC machine)

$$\text{Total Dose} = 1.08 \times 10^{16} / \text{cm}^2$$

$$\text{Conc. Level} = 1.00 \times 10^{20} / \text{cm}^3$$

Steps are being taken to ensure that the dose measurement system functions more reliably. The initial system had independent Faraday cup detectors and a heated substrate holder. These are being replaced by a single Faraday cup and greater care is being exercised with in situ leakage measurements.

Effort will also be focused on making sure that the component of $^{28}\text{N}_2^+$ in the beam is negligibly small. This can be accomplished mainly by making sure that the components in the gas feed line in the accelerator terminal are leak-tight and by looking with SIMS for the presence of ^{14}N .

In summary, the results of the high-energy implant experiments to date indicate that: (1) beams of $^{11}\text{B}^+$ can be produced at energies up to 2 MeV, and (2) beams of $^{28}\text{Si}^+$ can be produced at energies up to 1.2 MeV. SIMS analysis* has proved to be a useful tool for analyzing the results of implant experiments,

*All SIMS measurements were made on unannealed samples.

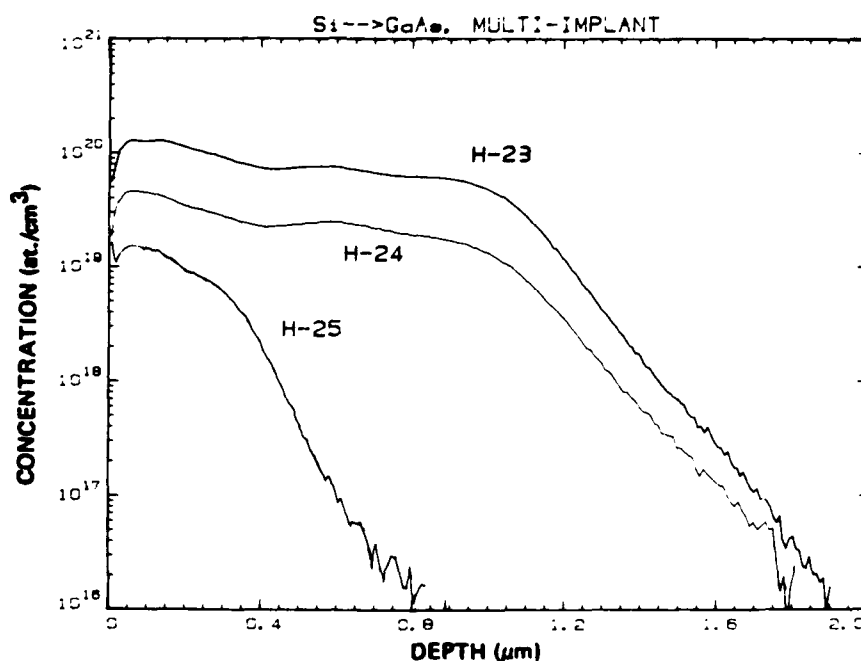


Figure 49. SIMS plots of the multiple-implant profiles formed using different dose levels.

and curve-fitting technique, involving the calculation of the first four moments from the experimental data, can be used to approximate the measured profiles.

Further experiments are being planned to

- (1) investigate implants into amorphized substrates to study the amount of channeling occurring for 7° off-axis implants;
- (2) improve the accuracy of the dose measurement system; and
- (3) ensure that $^{28}\text{N}^+$ components in the incident beam are negligible.

3. Mobility, Carrier Concentration, and Activation Efficiency

Following thermal annealing, the electrical characteristics of the high-energy implanted n-layers were evaluated by the van der Pauw measurement. The measuring technique was briefly described earlier. Table 5 shows the measured sheet carrier concentration, N_s , sheet resistance, ρ_s , Hall mobility, μ , and the activation efficiency, η , on the 1-MeV Si-implanted GaAs. The implanted

TABLE 5. 1-MeV Si IMPLANTATION IN GaAs

Sample No.	Energy (keV)	Dose (at./cm ²)	N _s (cm ⁻²)	ρ _s (Ω/□)	μ (cm ² /V-s)	η (%)
H15	1000	5.0x10 ¹⁵	3.67x10 ¹³	85	2000	0.734
H16	1000	1.5x10 ¹⁵	5.67x10 ¹³	65	1690	3.78
H17	1000	5.0x10 ¹⁴	7.33x10 ¹³	49	1760	14.7
H18	1000	1.5x10 ¹⁴	4.62x10 ¹³	52	2620	30.8
H19	1000	5.0x10 ¹³	2.7x10 ¹³	70	3310	54.2
H20	1000	1.5x10 ¹³	1.10x10 ¹³	142	3980	73.5

Si doses varied between 1.5×10^{13} and 5×10^{15} at./cm². The mobilities and activation efficiencies obtained are either comparable to or better than those obtained with low-energy implantation at comparable dose levels. The mobilities are in the range of 1690 cm²/V-s for high-dose implanted samples to 3980 cm²/V-s for low-dose implanted samples; the activation efficiencies are in the range of below 1% for high-dose implanted samples to over 73% for low-dose implanted samples. All the data shown in Table 5 are for samples capless-annealed at 825°C for 20 min [3].

The activation efficiency of heavily implanted samples increased at a higher annealing temperature. This result is shown in Table 6 where Si-implanted wafers were annealed at two different temperatures, 825 and 970°C. The two samples annealed at 970°C give rise to a higher activation efficiency. The annealing was done in a N₂ atmosphere with samples encapsulated with 2000-Å-thick reactively sputtered Si₃N₄. Mobility and sheet resistance data measured for samples implanted between 600 and 1200 keV at a dose level of 3×10^{15} at./cm² are summarized in Fig. 50.

Figure 51 shows the measured sheet carrier concentration as a function of Si dose for samples implanted at 200 keV and 1 MeV, respectively, and annealed thermally at 825°C for 20 min. The 1-MeV implanted samples showed a substantially higher sheet carrier concentration in the dose range of 5×10^{13} to 2×10^{15} at./cm². This result may be due to the fact that, at a given dose level, the 1-MeV implant results in a lower impurity concentration distribution than that of the 200-keV implantation, because of its higher straggle value. As a

TABLE 6. RESULTS OF Si-IMPLANTED WAFER AT 825 AND 970°C.

Sample No.	Energy (keV)	Dose (at./cm ²)	Anneal Temp (°C)	N _s (cm ⁻²)	ρ _s (Ω/□)	μ (cm ² /V-s)	η (%)
H10	900	3.0x10 ¹⁵	825	4.16x10 ¹³	83.5	1800	1.39
			970	2.13x10 ¹⁴	22.2	1320	7.10
H11	1000	3.1x10 ¹⁵	825	3.73x10 ¹³	92.7	1807	1.20
			970	1.47x10 ¹⁴	27.4	1554	4.14

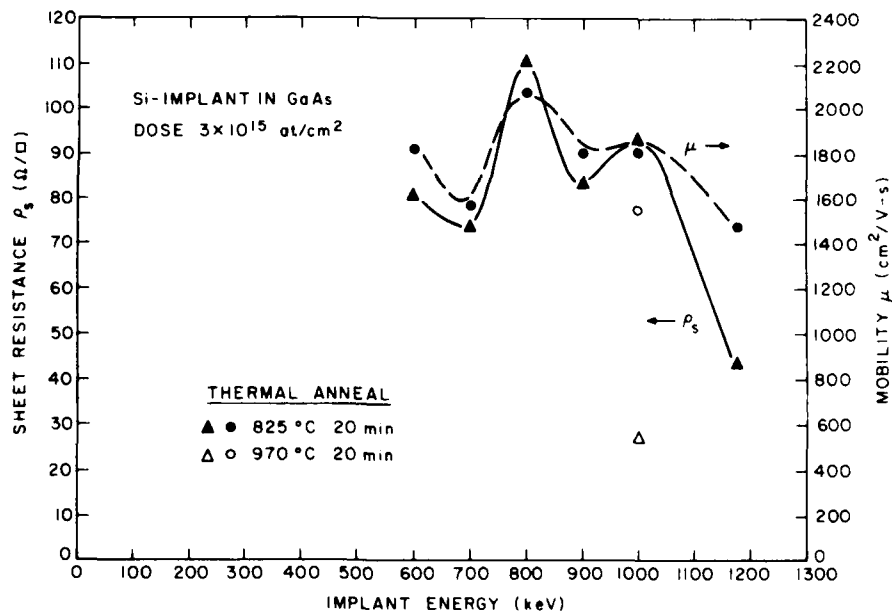


Figure 50. Mobility and sheet resistance measured after thermal annealing for samples implanted at different high-energy levels.

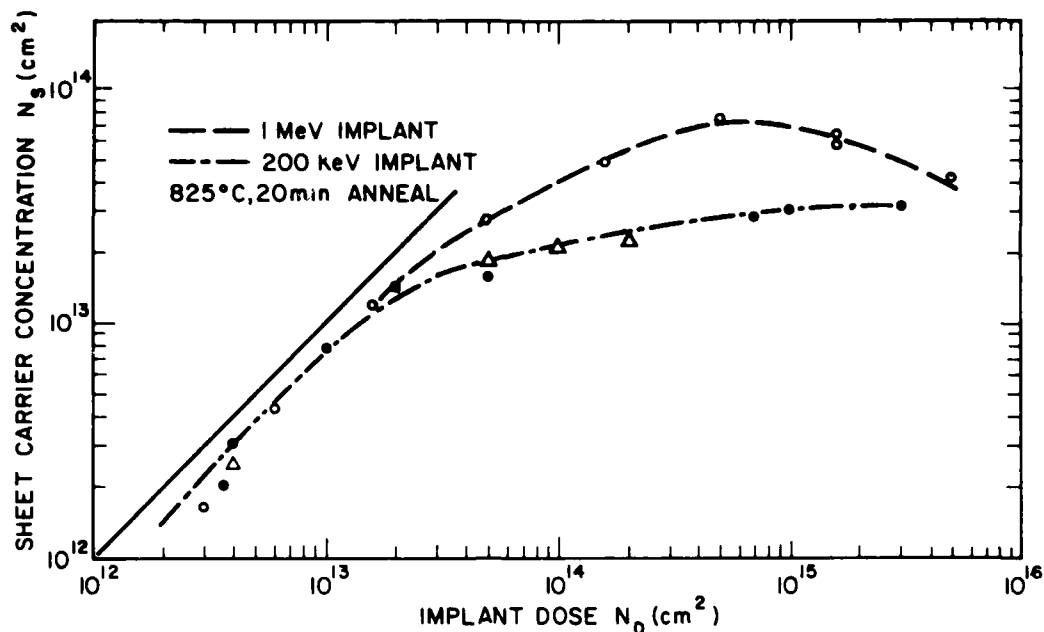


Figure 51. Measured sheet carrier concentration as a function Si-implanted samples at 200 keV and 1 MeV.

result, the 1-MeV high-dose implanted samples are less limited by the solid solubility during the thermal annealing than the 200-keV implant samples. The drooping in the sheet carrier concentration at the high-dose level is not fully understood and is being further studied.

4. Carrier Concentration Distribution

The electron density profiles of high-energy implanted, thermal-annealed samples were evaluated using differential C-V measurement in conjunction with controlled layer removed by chemical etching. Each controlled chemical etching step was between 500 and 1500 μm depending on the electron densities of the layer being removed. Large etching steps were used for low-density regions ($\leq 10^{17}/\text{cm}^3$). Schottky-barrier diodes were formed by evaporation of aluminum onto the surface following each chemical etching step, and depth profiles were measured on automatic C-V profile equipment.

Figures 52 to 55 show the electron concentration distribution of Si-implanted semi-insulating GaAs samples measured using this technique. Figures 52, 53, and 54 are for samples implanted at an energy level of 1 MeV, with fluences of 1.5×10^{14} , 5×10^{13} , and 1.5×10^{13} at./cm², respectively. The circular points shown in the figures are normalized data from SIMS measurement on a high-dose single-implanted (1 MeV) unannealed sample (Fig. 52). Figure 55 shows the profile of a multiple-implanted sample (H27) designed to produce a 1- μ m flat profile with a maximum impurity concentration of 1×10^{18} at./cm³. The implant parameters are therefore the same as those shown in Table 4, except all the fluences are two orders of magnitude lower. The samples were capless-annealed at 825°C for 10 min in an arsenic overpressure following implantation.

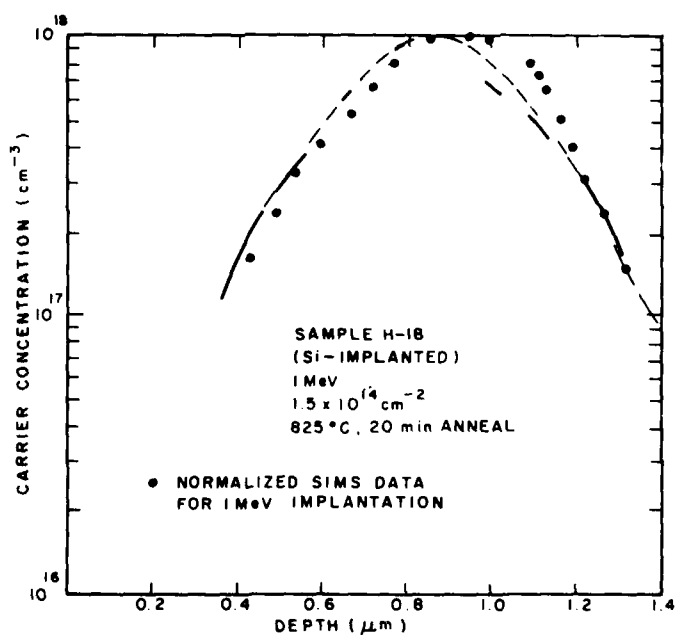


Figure 52. Electron concentration distribution, 1-MeV, Si-implanted, 1.5×10^{14} at./cm².

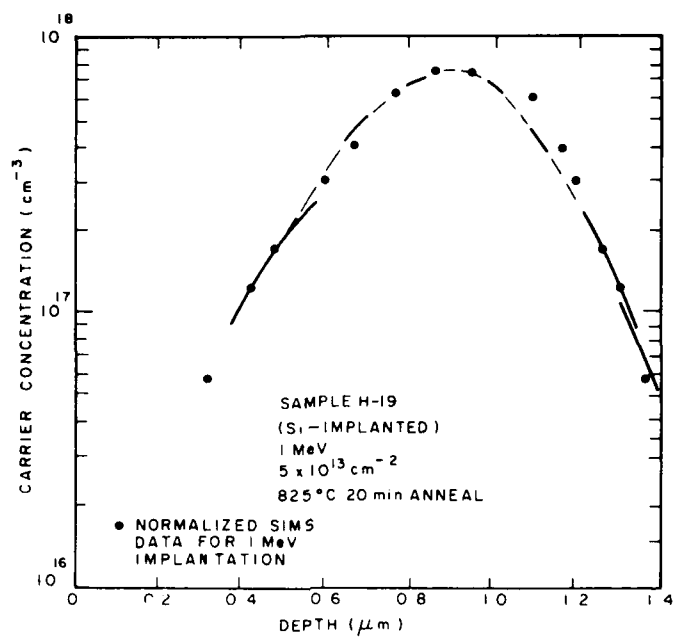


Figure 53. Electron concentration distribution, 1-MeV, Si-implanted, $5 \times 10^{13} \text{ at./cm}^2$.

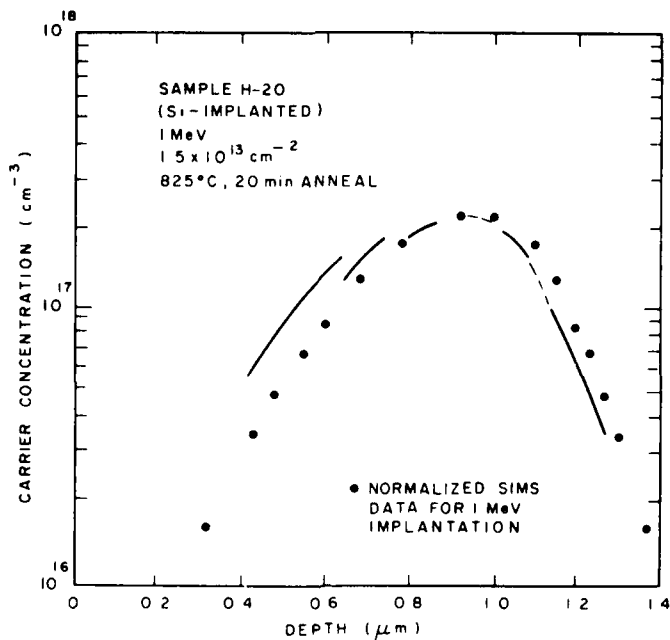


Figure 54. Electron concentration distribution, 1-MeV, Si-implanted, $1.5 \times 10^{13} \text{ at./cm}^2$.

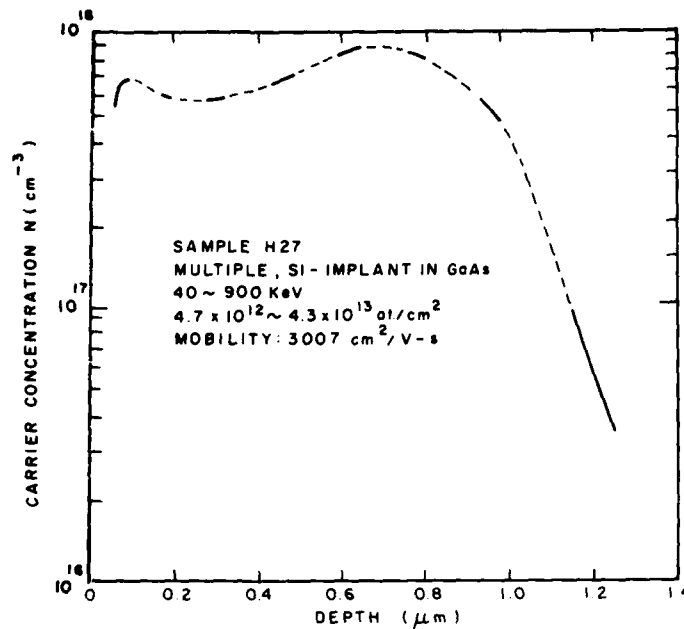


Figure 55. Carrier concentration of a multiple-implanted sample.

The shape of the profiles determined from the differential C-V measurements show reasonable agreement with the SIMS measurements made on high-dose implanted unannealed samples (Figs. 52 and 54). The differences in range and standard deviation are approximately within 10% on the 1-MeV single energy implanted samples. The deviations between the multiple-implanted profiles determined by the SIMS and the C-V measurement are greater. This is expected because the C-V measurement determines the electrically active carrier concentration distribution, while the activation efficiency varies with amount of dose and energy. A better match can be obtained by including the dose-and-energy-dependent activation efficiency in the flat-profile design.

SECTION V

LASER ANNEALING

A. INTRODUCTION

During this program we have studied annealing of Si-implanted GaAs with a high-power Q-switched Nd:glass laser ($\lambda = 1.06 \mu\text{m}$) and with a high-power Q-switched ruby laser ($\lambda = 0.694 \mu\text{m}$). Recent research has shown that laser annealing is an attractive alternative to thermal annealing for removing lattice disorders created by high-energy implantation [18-22]. In contrast to the ruby laser, the photon energy of the Nd:glass laser (1.17 eV) is less than the band-gap of GaAs (1.4 eV at 300 K). The optical absorption at the Nd:glass laser wavelength is therefore strongly dependent upon the amount of impurities and lattice defects produced by implantation. This section describes studies made on as-implanted and laser-annealed samples using van der Pauw measurements, secondary ion-mass spectroscopy (SIMS), and optical absorption measurements. The results are compared with those obtained using thermal annealing. Surface morphology of laser-annealed GaAs layer and ohmic contacts made onto laser-annealed GaAs have been studied. Forming ohmic contacts onto laser-annealed high dose implanted GaAs surface without alloying has been demonstrated. This effort is supported in part by an Office of Naval Research Program (N00014-78-C-0367).

18. E. I. Shtyrkov, I. B. Khaibullin, M. M. Zaripov, M. F. Galyatudinov, and R. M. Bayazitov, "Local Annealing of Implantation Doped Semiconductor Layers," *Sov. Phys. Semicond.* **9**, 1309 (1976).
19. S. U. Compisano, I. Catalano, G. Foti, E. Rimini, F. Eisen, and M. A. Nicolet, "Laser Reordering of Implanted Amorphous Layers in GaAs," *Solid State Electron.* **21**, 485 (1978).
20. R. T. Young, C. W. White, G. J. Clar, J. Narayan, W. H. Christie, M. Murakami, P. W. King, and S. D. Karner, "Laser Annealing of Boron-Implanted Silicon," *Appl. Phys. Lett.* **32**, 139 (1978).
21. S. G. Liu, C. P. Wu, and C. W. Magee, "Annealing of Ion-implanted GaAs with Nd:glass Laser," presented at the Symp. on Laser-Solid Interaction and Laser Processing held in Boston, MA, Nov. 28-Dec. 1, 1978. AIP Conference Proceedings No. 50, p. 603, New York, 1979.
22. B. J. Sealy, M. H. Badawi, S. S. Kular, and K. G. Stephens, "Electrical Properties of Laser-Annealed Donor-Implanted GaAs," *Electron. Lett.* **14**, 720 (1978).

B. HIGH-POWER PULSED LASER SYSTEM

The laser system used is the Korad Model K-1500 gigawatt laser system* (Fig. 56). This consists of the oscillator, the amplifier, and the Pockel cell unit for Q-switching the oscillator output. The oscillator ruby rod is 10.16x0.95 cm (4x3/8 in.) in diameter and is wrapped around by a helical xenon flashlamp, which serves to optically pump the laser material and produce a population inversion of the chromium ions in the ruby when at least half the chromium ions are excited. Lasing occurs when the round-trip gain between parallel mirrors placed at opposite ends of the oscillator ruby rod is greater than unity. The Pockel cell Q-switch prevents threshold for lasing from being attained by effectively reducing the reflectivity of the rear cavity mirror to zero. This allows the ruby rod to achieve a maximum energy storage, which corresponds to a high value for the gain coefficient. The cell is then triggered to "insert" the cavity mirror, at which time a high cavity gain occurs. This results in a "giant pulse" with high power density and short pulse duration, typically 25 to 30 ns. This giant pulse is then further amplified by an amplifier stage. The amplifier ruby rod is 22.9x1.9 cm (9x3/4 in.) in diameter and works by stimulated light emission triggered by the giant pulse pulse from the oscillator stage and the Pockel cell. Amplification by a factor as high as 20X can be achieved. Maximum laser output power is 1 GW/pulse at 2 pulses/min.

At a given oscillator rod high voltage above the threshold value of 3.98 kV, the laser output pulse width is a function of two parameters, namely, Q-switch shutter delay and Pockel cell bias voltage. These two parameters are independent of each other so that they can be optimized separately. The laser output pulse width was measured with a photodiode and a Tektronix** 7704 fast oscilloscope. The photodiode used was silicon avalanche photodiode, type C30902E from RCA Electro Optics and Devices.*** The rise time was specified to be 0.4 ns which was adequate for this application. The Tektronix 7704 oscilloscope was set up to operate in the triggered single sweep mode, and a

*Hadron, Inc., Korad Div., Santa Monica, CA.

**Tektronix Inc., Beaverton, OR.

***RCA Electro Optics and Devices, Lancaster, PA.

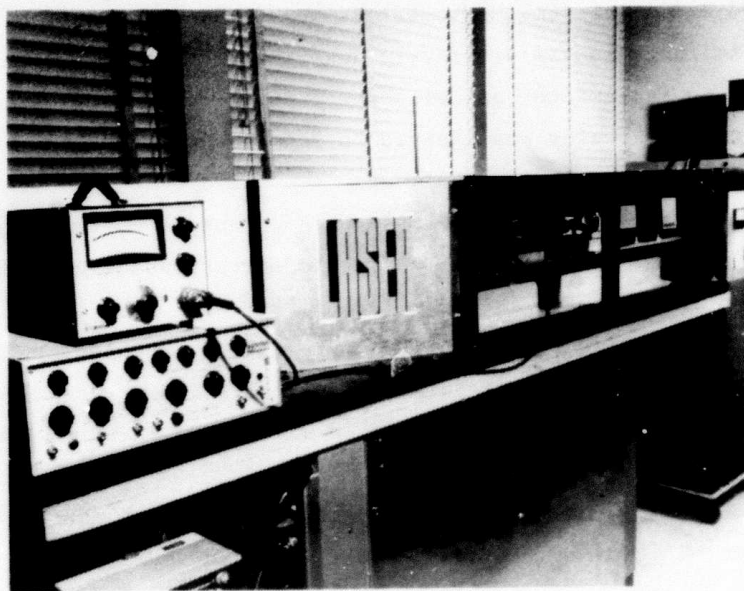


Figure 56. High-power pulsed laser system.

camera with ultrafast Polaroid* film (Type 410, ASA 10,000) was used to photograph the pulse. The optimum pulse shape recorded had a Gaussian distribution with a FWHM of 30 ns. The same laser system was modified for Nd-glass laser experiments with replacement of the laser rod and associated optical devices.

The energy of the laser output pulse was measured with a Korad K-J Calorimeter which gives a voltage output in microvolts proportional to the energy of the input pulse. The proportionality constant was 0.198 J/ μ V as specified and calibrated by Korad.

The laser output energy per pulse can be adjusted by varying the high voltage on the xenon lamps around the amplifier stage and/or around the oscillator stage. After firing the system for 5 or 6 times and reaching a thermal equilibrium in the laser rods, the output energy of the laser pulses is found to be reproducible to $\pm 20\%$.

*Polaroid Corp., Cambridge, MA.

C. PULSED Nd:GLASS LASER ANNEALING

Semi-insulating GaAs substrates of (100) orientation were implanted under high vacuum with $^{28}\text{Si}^+$ at energies between 70 and 200 keV, and fluence between 3×10^{12} and 3×10^{15} at./cm². The wafers were polished and chemically etched prior to implantation as previously described. Some wafers were polished on both sides to facilitate optical absorption studies. Following implantation, the 0.04-cm-thick wafer was cleaved to samples approximately between 0.5 and 2 cm² for laser-annealing experiments.

The Nd:glass laser was operated with an output energy density of between 0.2 and 2.5 J/cm² per pulse (25 ns). The corresponding power density lies between 8 and 200 MW/cm². The diameter of the laser beam is 2 cm. The thermally annealed samples used for comparison were either annealed at 825°C for 20 min under an arsenic overpressure without encapsulation or annealed at temperatures up to 1000°C using samples encapsulated with a 2000-Å-thick sputtered Si₃N₄ layer.

Figure 57 shows comparative results [21] of sheet carrier concentration density for Nd:glass laser and thermally annealed samples with implanted ^{28}Si doses between 3×10^{12} and 3×10^{15} at./cm². The energy density of each laser pulse used in the annealing is indicated by crosses in the figure; they vary between 0.5 and 1.17 J/cm². All experiments were performed with single pulses. At the low energy density level, the implanted layers are only partially annealed. The electrical activation is greatly enhanced by laser annealing for samples implanted with doses higher than 3×10^{14} at./cm². The sheet carrier concentration density N_s as determined by van der Pauw measurement is two-to-five times higher than that of samples thermally annealed at 825 or 1000°C for 20 min. The low electrical activation at a lower dose level for a given pulsed laser energy may be attributed to the reduction in enhanced optical absorption. This reduction is dependent on the amount of dose of the implantation as studied by the optical absorption measurements [21].

Table 7 lists some measured results on the mobility, the sheet carrier concentration, and the activation efficiency on Si-implanted GaAs samples annealed by a Nd:glass laser and by thermal anneal. The fluence listed in the table is greater than 3×10^{14} at./cm². The laser-annealed samples showed higher activation efficiencies. The mobility for laser-annealed samples are 253 cm²/V-s at a sheet carrier concentration of 1.91×10^{14} at./cm², and 529 cm²/V-s at 1.24×10^{14}

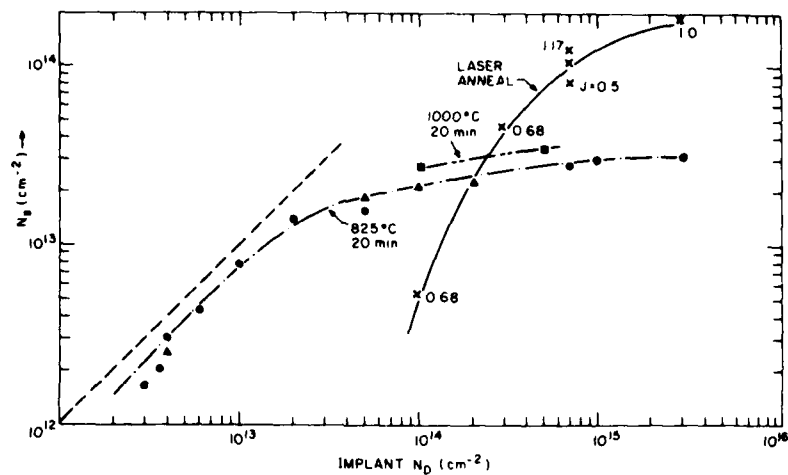


Figure 57. Comparison of thermal and laser annealing; 1.06- μ m, 25-ns single-pulse (Nd:glass) laser was used.

TABLE 7. COMPARISON OF THERMAL AND Nd:GLASS LASER ANNEALING DATA

Si Implantation			Nd:Glass Laser Annealing			Thermal Annealing		
Dose (cm^{-2})	Energy (keV)	Energy (J/cm^2)	N_s (cm^{-2})	μ ($\text{cm}^2/\text{V-s}$)	η (%)	N_s (cm^{-2})	μ ($\text{cm}^2/\text{V-s}$)	η (%)
3.0×10^{15}	70	1.00	1.91×10^{14}	253	6.4	5.1×10^{13}	1392	1.7
3.0×10^{15}	200	2.25	1.45×10^{14}	1017*	4.8	3.3×10^{13}	1909	1.1
1.0×10^{15}	70	0.34	6.55×10^{13}	254	6.6	3.2×10^{13}	1770	3.2
$5/2 \times 10^{14}$	200/70	1.17	1.25×10^{14}	529	17.9	2.8×10^{13}	1881	4.0
3.0×10^{14}	200	0.68	4.60×10^{13}	522	15.3	3.0×10^{13}	1540	10.0

*Laser plus thermal annealing, $\rho_s = 42 \Omega/\square$.

at./ cm^2 , compared with a mobility of $1392 \text{ cm}^2/\text{V-s}$, at 2.9×10^{13} at./ cm^2 and $1881 \text{ cm}^2/\text{V-s}$ at 2.8×10^{13} at./ cm^2 for similar samples annealed thermally.

The optical absorption in the sample was measured by spectrophotometry. The transmission through the sample and the reflection from the sample were measured on a Cary spectrometer in the 7000- to 12000- \AA wavelength range. The absorption at a given wavelength (e.g., $1.06 \mu\text{m}$) is calculated by the expression:

$$A = 1 - T - R$$

where A, T, and R are, respectively, absorption, transmission, and reflection which are all absolute values and are expressed in percentages. The enhanced absorption due to implantation damage is equal to $A - A_0$, where A_0 is the absorption through the unimplanted sample. At 1.06- μm wavelength, the measured value of A_0 was typically 0.1. The reflectance was measured with reference to an aluminum mirror, and the absolute value is obtained through calibration. At 1.06 μm , the reflectance of aluminum on glass is 0.862.

Figure 58 shows the reflectance measured on an as-implanted wafer and on the same wafer irradiated with a Nd:glass laser pulse at an energy density of 0.34 J/cm^2 . Because of the enhanced absorption in the high-dose implanted layer, the reflection is affected only by the front (implanted) surface. Consequently, the reflectance forms a continuous line as it passes through the absorption edge as shown in Fig. 58a. In the case of the annealed sample, restored lattice order reduces the enhanced absorption in the implanted layer. As a result, the reflectance spectrum forms a step (Fig. 58b) as the optical wavelength passes through the band edge of GaAs, because the reflection is enhanced in the long wavelength range due to multiple reflection from the polished sample back surface. The multiple reflection dominates over the change in surface reflectivity which occurs as a result of implantation.

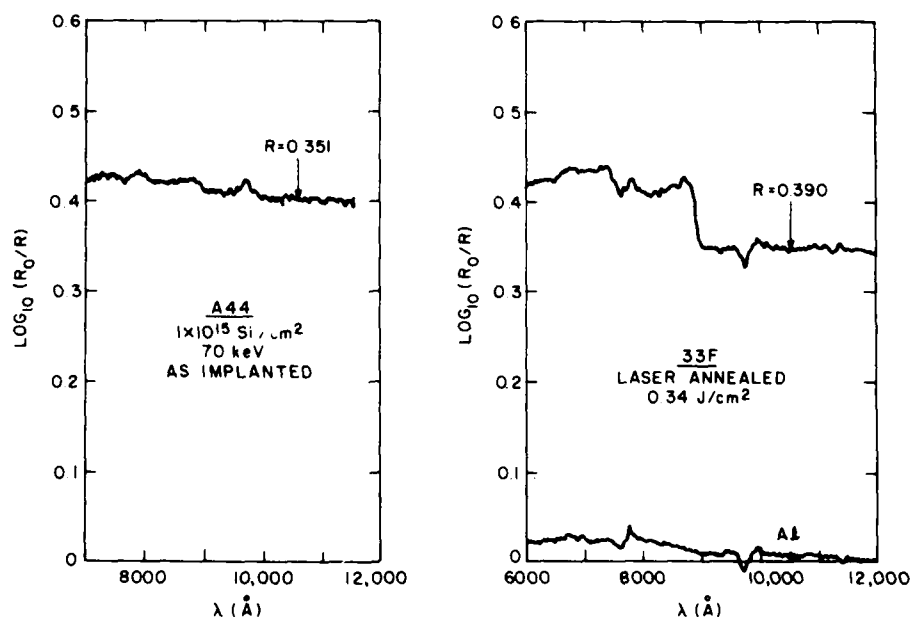


Figure 58. Reflectance measured on an as-implanted wafer (a) and after laser-annealing (b).

The transmittance through an ion-implanted sample before and after annealing is shown in Fig. 59. The gradual increase in absorption from the long-wavelength side toward the absorption edge in the as-implanted sample is a band-tailing effect produced by impurities [23]. The transmittance at 1.06- μm wavelength changes from 0.170 for the as-implanted sample to 0.457 after laser annealing at 0.68 J/cm². The enhanced absorption ($A-A_0$) can be evaluated from the expression given in the previous section. Figure 60 shows the measured values of transmittance, reflectance, and enhanced absorption for as-implanted samples at different dose levels.

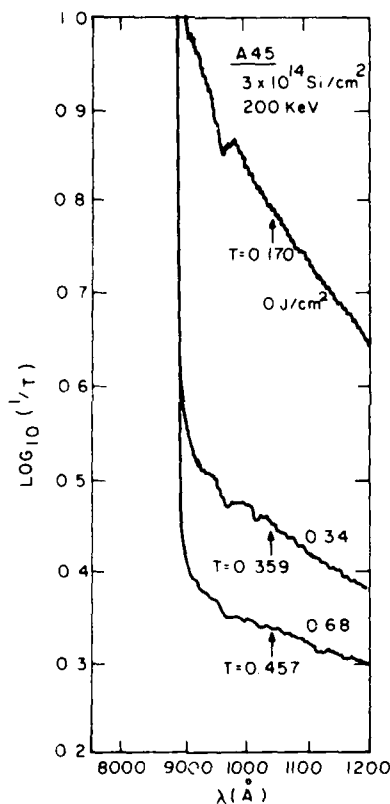


Figure 59. Optical transmission from Si-implanted GaAs sample annealed at different laser energy densities.

23. A. Gat and J. F. Gibbons, "A Laser-Scanning Apparatus for Annealing of Ion-Implantation Damage in Semiconductors," Appl. Phys. Lett. 32, 142 (1978).

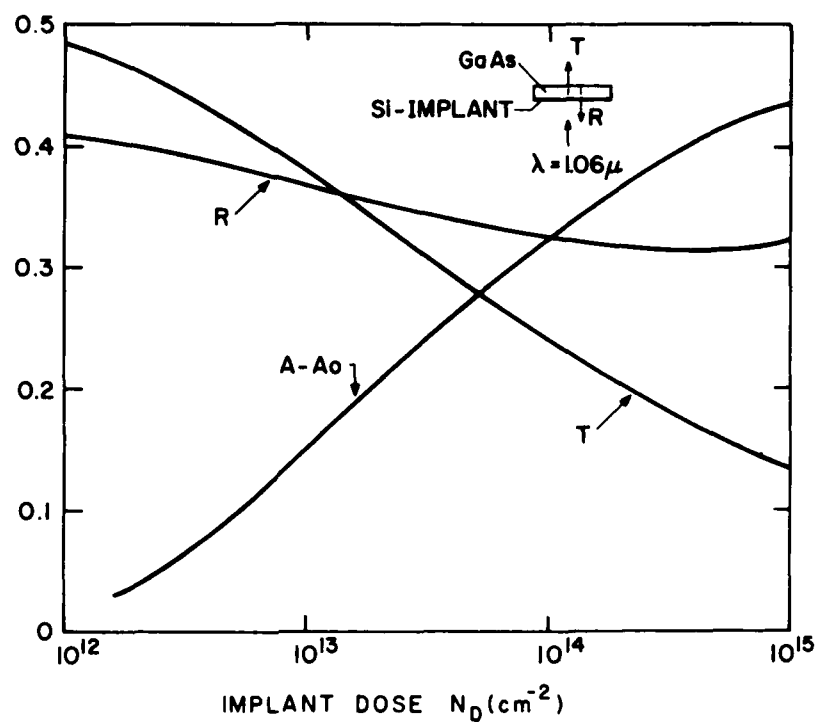


Figure 60. Measured values of transmittance (T), reflectance (R), and enhanced absorption ($A-A_0$) for different dose levels.

Optical absorption measurement show that the implantation enhanced absorption at a given wavelength (e.g., $106 \mu\text{m}$) below the band edge increases with implant dose. This enhanced absorption is greatly reduced following annealing as a result of lattice re-ordering. Such optical measurement may thus be used as a diagnostic technique for optimizing the required laser energy while maintaining good surface morphology.

D. PULSED RUBY-LASER ANNEALING

Laser-annealing experiments were also carried out using a ruby laser on Si-implanted (100)-orientated semi-insulating GaAs substrate. The wafers were implanted at 70, 100, and 200 keV, with doses ranging between 1×10^{14} and 1×10^{16} at./ cm^2 . The Q-switched ruby laser was operated with an output energy

density of between 0.5 and 2.3 J/cm² per 30-ns pulse. The electrical characteristics of the laser-annealed samples were studied using the van der Pauw measurements.

Figure 61 shows results of sheet carrier concentration densities as a function of the implantation dose level for samples annealed by high-power pulsed ruby laser, and for samples annealed thermally. The thermal annealing was done at 825 and 1000°C for 20 min, and the energy used for implantation was at 200 keV, as described previously. The energy densities used for laser anneal shown in Fig. 61 were 1.7 and 2.3 J/cm², which were higher than that plotted in Fig. 57. It is interesting to note that samples implanted at 200 keV show higher activation efficiencies than those implanted at 70 keV, at the high implant dose level. This may relate to the fact that the impurity density in the implanted layer is higher in the 70-keV implanted sample than in the 200-keV implanted sample because of the smaller straggle associated with the 70-keV implantation. Lower activation efficiencies were observed with increased fluence above 5×10^{14} at./cm² as shown in Fig. 61.

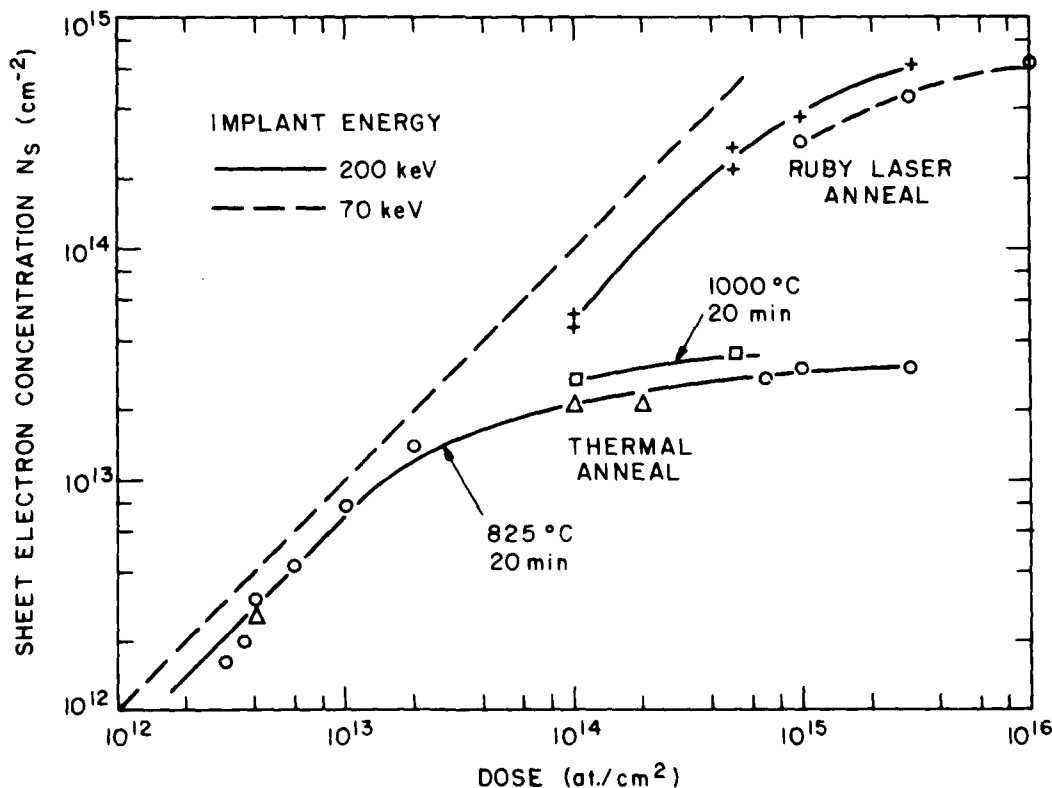


Figure 61. Sheet electron concentration as a function of dose for ruby-laser and thermal-annealed samples.

The sheet carrier concentration density of up to 6.25×10^{14} at./cm² with an activation efficiency of 20.8% was measured on high-dose implanted samples. These results are more than an order of magnitude higher than that for similar samples annealed thermally. Figure 62 shows a plot of the mobility, μ , the activation efficiency, η , and the sheet resistance, ρ_s , for 200-keV Si-implanted GaAs wafers implanted with three different fluences, and followed by a ruby-laser irradiation at 2.3 J/cm². Higher activation efficiencies (45 to 56%) and higher mobilities (930 to 1350 cm²/V-s) were measured in wafers implanted at a dose level ranging from 1×10^{14} to 5×10^{14} at./cm². The sheet resistances are lower and show little variations when the implant dose is higher than about 5×10^{14} at./cm². The sheet resistances at the high-dose region shown in Fig. 62 are typically 4 to 5 times lower than similar thermally annealed wafers. The lowest sheet resistance obtained was 20.8 Ω/\square , which was measured on samples implanted at 70 keV with a dose of 3×10^{15} at./cm², and annealed by ruby-laser irradiation at 2.3 J/cm².

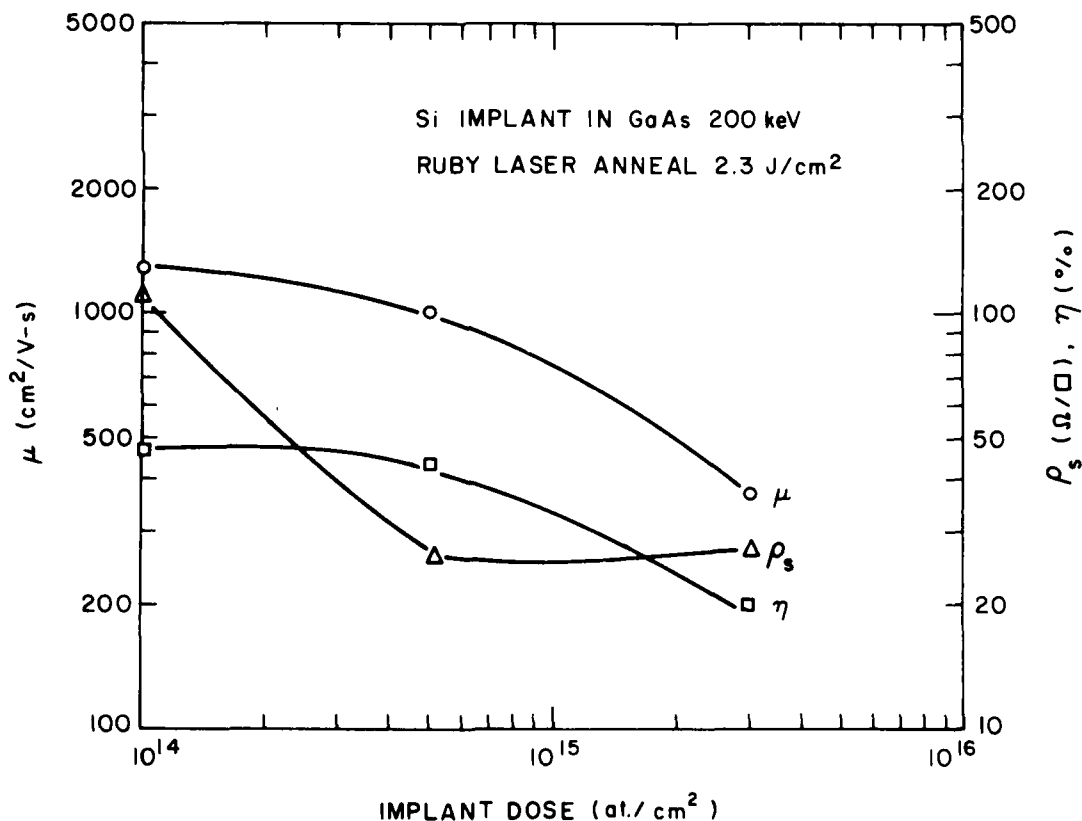


Figure 62. Mobility (μ), activation efficiency (η), and sheet resistance (ρ_s) as a function of dose.

The electrical characteristics of ion-implanted laser-annealed samples depend on the implantation energy and fluence, and the energy density of the laser irradiation on the sample surface. Figure 63 shows the measured mobility, the sheet resistance, and activation efficiency of a Si-implanted GaAs wafer irradiated by a ruby laser operated at different energy densities. The wafer was implanted at 200 keV with a fluence of 5×10^{14} at./cm².

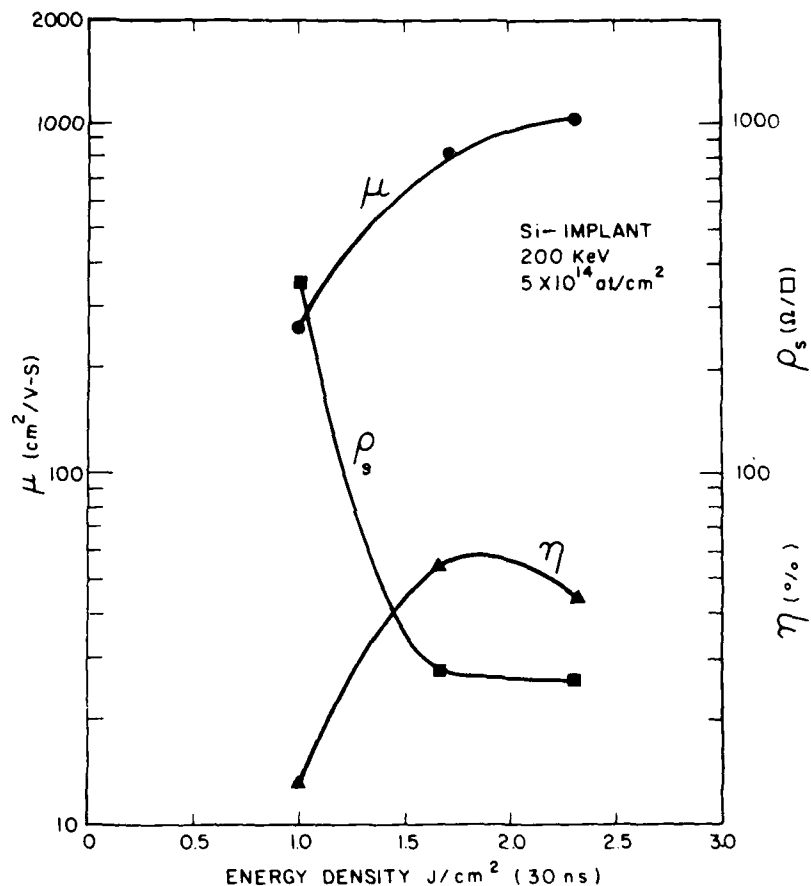


Figure 63. Mobility (μ), activation efficiency (η), and sheet resistance (ρ_s) as a function of energy density.

The data points indicate that the mobility and activation efficiency are much higher for samples irradiated at a higher surface energy density (1.7 to 2.3 J/cm²) than that irradiated at a lower surface energy density (1 J/cm²). The sheet resistance drops substantially from 360 Ω/\square at 1 J/cm², to 27 Ω/\square

at 1.7 to 2.3 J/cm². The sheet resistance starts to reach the low level at a laser energy density of about 1.5 J/cm², which may be considered as a threshold for full activation in this sample.

E. UNALLOYED OHMIC CONTACTS

The contact resistivity of ohmic contacts made onto GaAs has been reported to be inversely proportional to the carrier density of GaAs [24,25]. Contact resistivities of Au-Ge ohmic contacts on ion-implanted GaAs with different dose levels were studied using the TLM technique [26]. Since the laser-annealed heavily implanted GaAs layer shows a much higher activation than does the thermally annealed layer, one expects a superior ohmic contact formed onto such a surface.

We investigated characteristics of contacts on the laser-annealed high-dose (1 to 3x10¹⁵ at./cm²) Si-implanted SI GaAs wafers, and obtained encouraging results: ohmic contacts of low contact resistivity were formed by evaporation of Au-Ge/Ni/Au onto the laser-annealed surface without a subsequent alloying process. Nominally an alloying step at 400 to 450°C is required in order to form the ohmic contact. Figure 64 shows the I-V characteristics between two unalloyed ohmic contacts. Forming a good ohmic contact on GaAs without alloying is obviously of great interest for the device and the integrated circuit fabrication.

The contact resistivity and the sheet resistance of the unalloyed contacts were measured using the TLM technique [26]. Identical rectangular shaped ohmic contacts with varying spacing between them were formed on the sample surface. The contact was made by evaporation of 900 Å of Au-Ge, 300 Å of Ni, and 1500 Å of Au. The patterns were formed by photolithography and lift-off. Mesas were etched for isolation of the test pattern from the remaining implanted layer. Because no alloying step was used following evaporation, no degradations occurred in the metal surface and in the conductivity of the metal.

24. W. D. Edward et al., "Specific Contact Resistance of Ohmic Contact to GaAs," *Solid State Electron.* 15, 388 (1972).
25. Y. Goldberg and B. V. Tsarenkov, "Dependence of the Resistance of Metal GaAs Ohmic Contacts on the Carrier Density," *Soviet Phys. Semicond.* 3, 1447 (1970).
26. H. H. Berger, "Models for Contacts to Planar Device," *Solid State Electron.* 15, 145 (1972). Also, *J. Electrochem. Soc.* 119, 507 (1972).

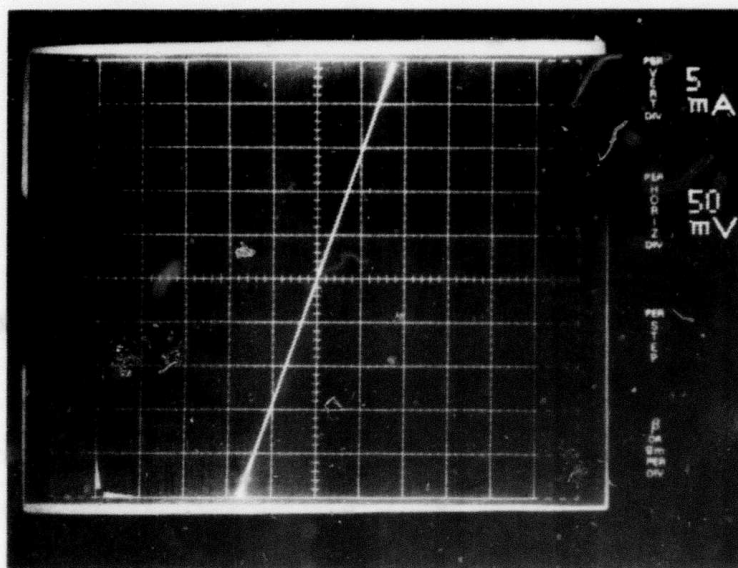


Figure 64. I-V characteristics between two unalloyed ohmic contacts.

Figure 65 shows the resistance between neighboring ohmic contacts measured as a function of spacing. From Fig. 65 the sheet resistance of the laser-annealed ion-implanted layer and the contact resistivity of the ohmic contact are deduced to be $57.6 \Omega/\square$ and $9.2 \times 10^{-6} \Omega\text{-cm}^2$, respectively. The sheet resistance checked reasonably well with that from the van der Pauw measurement. The sheet resistance value was also checked by using a pattern with a wider spacing between two rectangular-shaped ohmic contacts. The large spacing increases the accuracy of ρ_s , hence, the slope dR/dx , and the accuracy of the measurement. The dimensions of the wider spacing between the contacts, and the width, W , of the contacts, are 148 and 240 μm , respectively.

F. SIMS MEASUREMENTS

Impurity distribution in as-implanted, thermal-annealed, Nd:glass laser-annealed, and ruby laser-annealed samples have been investigated with the SIMS

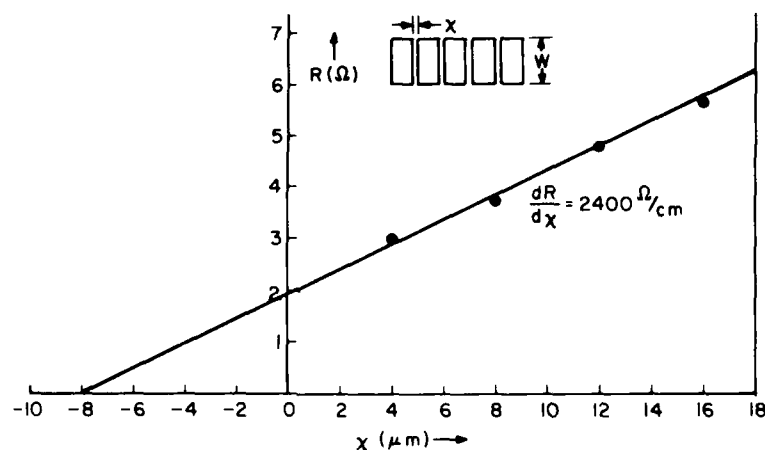


Figure 65. Resistance between neighboring ohmic contacts as a function of spacing.

technique. Depth profiles were obtained by bombarding the samples with 5-keV Cs^+ ions [27,28] while detecting the implanted ^{28}Si atoms as a molecular ion $^{75}\text{As}^{28}\text{Si}^-$ at mass 103. Ultrahigh vacuum (4×10^{-10} Torr) in the sample chamber during the analysis prevented interference from the molecular ion $^{71}\text{Ga}^{16}\text{O}_2$ which is also at mass 103.

The SIMS analyses show that the amount of impurity redistribution depends upon the energy and dose of implantation, and the energy density of the laser pulse used to anneal the sample. No redistribution occurred after irradiation with a low energy-density pulse, but a substantial impurity broadening was observed in high-dose implanted samples irradiated with a high energy-density pulse ($\sim 2 \text{ J/cm}^2$). The broadening is believed to be associated with a diffusion in the liquid GaAs created by the high-energy laser pulse. An anomalous shoulder broadening effect was observed in the SIMS profile, after thermal annealing, in Si-implanted SI GaAs with high peak impurity concentration in the implanted layer; the anomalous broadening is believed to be associated with the damage-enhanced diffusion associated with the implantation.

27. P. Williams, R. K. Lewis, C. A. Evans, and P. R. Hanley, "Evaluation of a Cesium Primary Ion Source on an Ion Microprobe Mass Spectrometer," *Anal. Chem.* **49**, 1399 (1977).
28. C. W. Magee, *J. Electrochem. Soc.* (in press).

Figure 66 shows the SIMS profile of a Si-implanted GaAs sample before and after thermal annealing (825°C, 20 min). The sample was implanted at 200 keV with a dose of 5×10^{14} at./cm². The peak impurity concentration was 2.3×10^{19} at./cm³. No impurity redistributions were observed after thermal annealing under these implantation conditions.

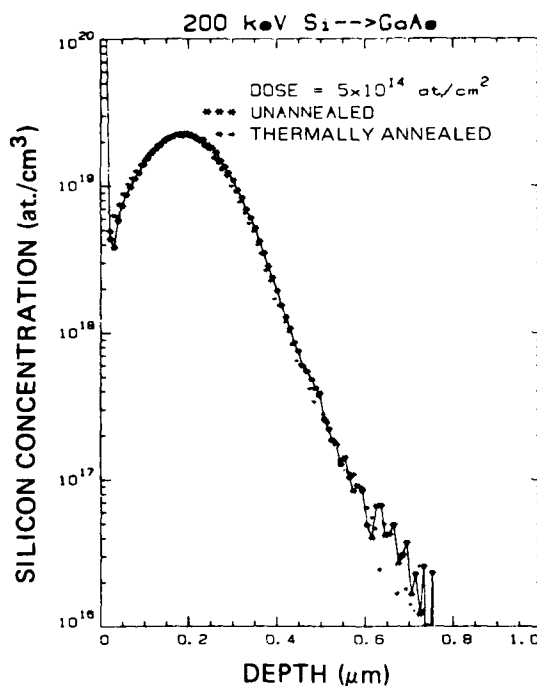


Figure 66. SIMS profile of a Si-implanted GaAs sample before and after thermal annealing, 200 keV, 5×10^{14} at./cm².

Figure 67 shows the SIMS profile of a Si-implanted GaAs sample before and after thermal annealing under the same conditions. The sample was implanted at 70 keV with a dose of 3×10^{15} at./cm². The peak impurity concentration was 3.2×10^{20} at./cm². A shoulder broadening effect occurred at an impurity concentration of about 3×10^{18} at./cm³. The shoulder extends to a depth of 0.35 μm.

These results are believed to be caused by damage-enhanced diffusion of unprecipitated silicon, similar to that being reported in Se-implanted GaAs [29].

29. A. Lidow, J. F. Gibbons, V. R. Deline, and C. A. Evans, Jr., "Solid Solubility of Selenium in GaAs as Measured by Secondary Ion Mass Spectrometry," Appl. Phys. Lett. 32, 572 (1978).

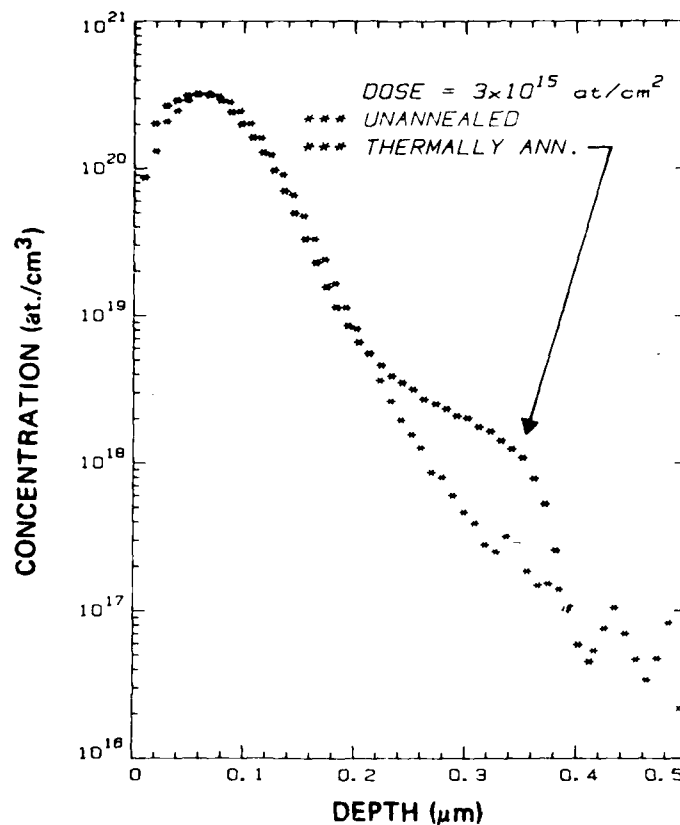


Figure 67. SIMS profile of a Si-implanted GaAs sample before and after thermal annealing, 70 keV, 3×10^{15} at./cm².

Experiments here further demonstrated the dependence of anomalous broadening on the implantation conditions, which affect the degree of damage in the sample.

Figure 68 shows the SIMS profile [21] of a sample implanted at 70 keV with a dose of 1×10^{15} at./cm², (peak impurity concentration $\sim 10^{20}$ at./cm³) before and after irradiation with a low-energy density (0.3 J/cm^2) pulse (25 μs) from a Nd:glass laser. The profile shows no redistribution in impurity after irradiation with a single laser pulse up to about 1 J/cm^2 in energy density.

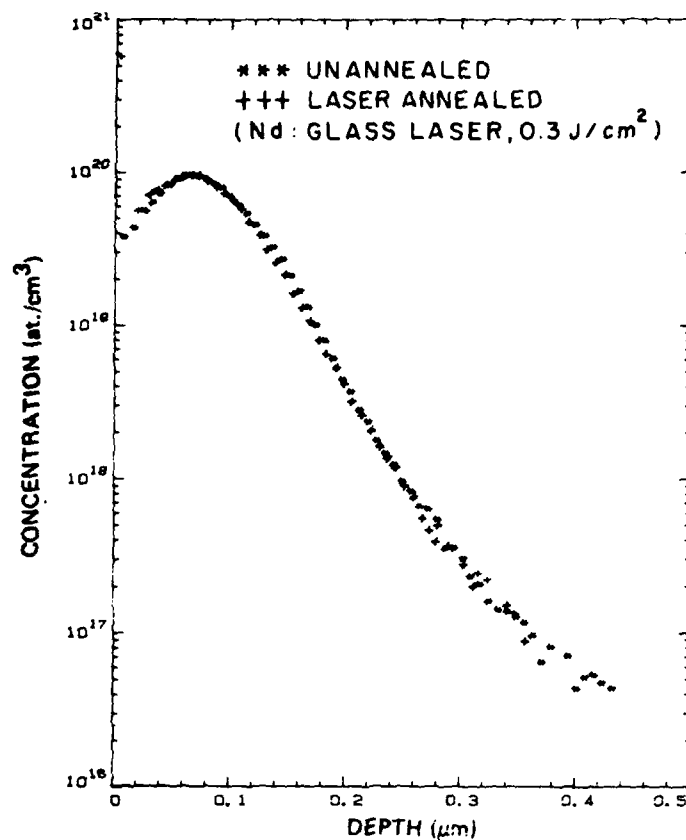


Figure 68. SIMS profile of a Si-implanted GaAs sample before and after laser annealing, 70 keV, 1×10^{15} at./cm².

Figure 69 shows three SIMS profiles: one is the profile of a GaAs wafer as-implanted at 70 keV with a dose of 3×10^{15} at./cm²; the other two are samples from the same wafer after being irradiated with single ruby-laser pulses at energy densities of 1.0 and 2.3 J/cm², respectively. A redistribution in impurity density was observed in the laser-irradiated samples. The impurity profile broadening associated with the short-duration (30 ns) high-energy laser pulse irradiation suggests that melting occurs near the surface region, and the substantial broadening in impurity distribution is a result of diffusion in liquid GaAs.

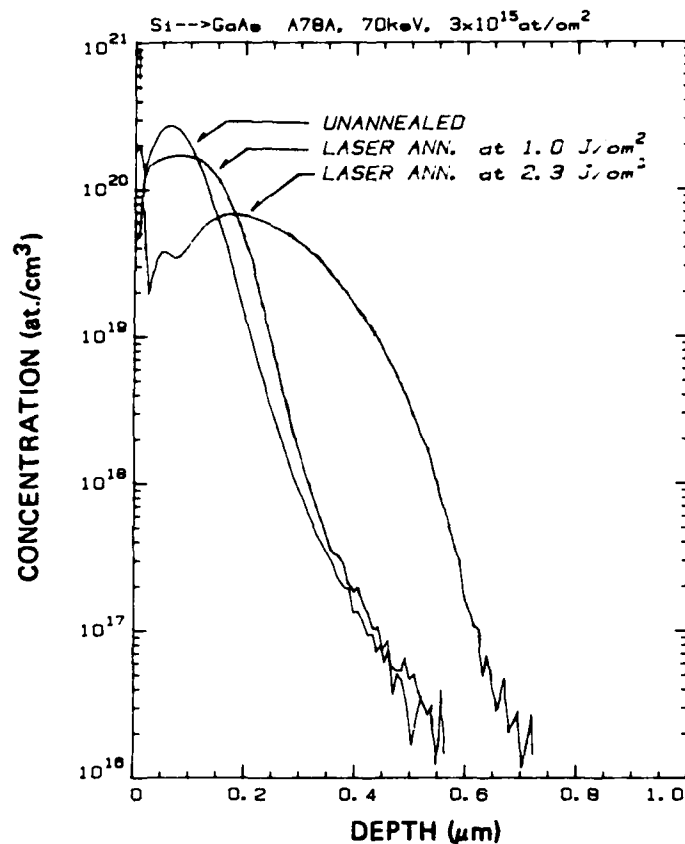


Figure 69. SIMS profiles: unannealed GaAs wafer; laser-annealed at 1 J/cm^2 ; and laser-annealed at 2.3 J/cm^2 .

Figure 70 shows the SIMS profiles of a GaAs sample implanted at 70 keV with a very high dose of $1 \times 10^{16} \text{ at./cm}^2$. The impurity density of the as-implanted sample peaks at $1 \times 10^{21} \text{ at./cm}^3$. After thermal annealing (825°C , 20 min), the impurity profile does not vary except a shoulder broadening occurs at an impurity concentration of $2 \times 10^{19} \text{ at./cm}^2$. After irradiation with a 2.3-J/cm^2 ruby-laser pulse, the peak impurity concentration drops by an order of magnitude to about $1 \times 10^{20} \text{ at./cm}^2$, and the impurity penetrates to a depth of about $0.8 \mu\text{m}$. The deeper penetration depth associated with the higher impurity concentration further suggests the occurrence of diffusion in the melted GaAs surface layer.

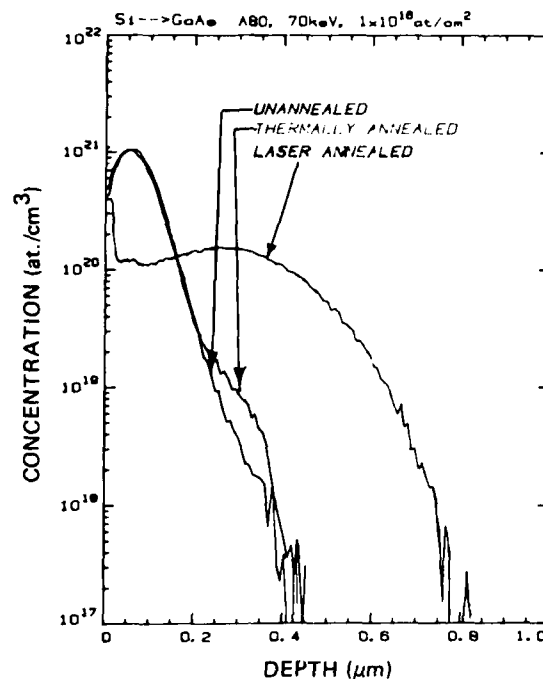
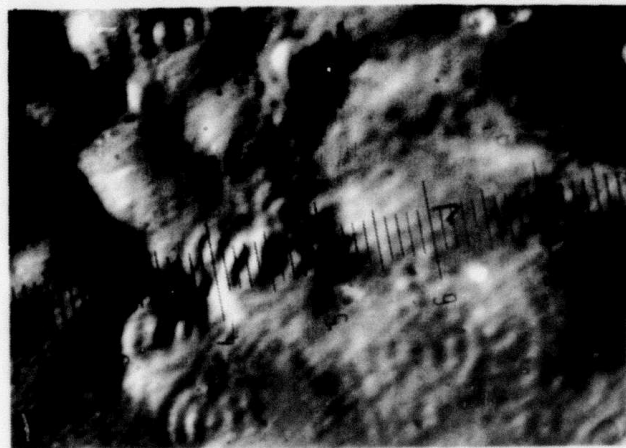


Figure 70. SIMS profiles: unannealed, thermal-annealed, laser-annealed samples.

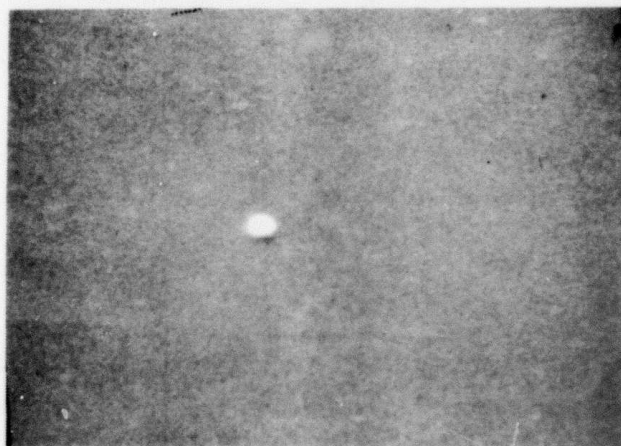
G. SURFACE MORPHOLOGY STUDY

SEM photographs of samples irradiated with high energy-density pulse (2.3 J/cm^2) shows no structures detectable on the surface microscopically at 20K magnification, (Fig. 71) although the sample surface visually appears wavy. A Nomarski interference contrast micrograph (Fig. 71) shows an uneven rippled surface. These results suggest that melting and epitaxial regrowth are associated with annealing of GaAs by high energy-density laser pulse. Similar ripples [30] were observed on laser-annealed silicon surfaces, and it was suggested that the ripple formation occurs when the melting threshold is periodically exceeded. Examination of high-dose implanted GaAs samples irradiated

30. W. L. Brown, J. A. Gdovchenko, K. A. Jackson, L. C. Kimerling, H. J. Leamy, G. L. Miller, J. M. Poate, J. W. Rodgers, G. A. Rozgonyi, T. T. Sheng, T. N. C. Venkatesan, and G. K. Celler, "Laser-Annealing of Ion-Implanted Semiconductors," Proc. on Rapid Solidification Proc. - Principles and Technologies, Reston, VA, Nov. 1977.



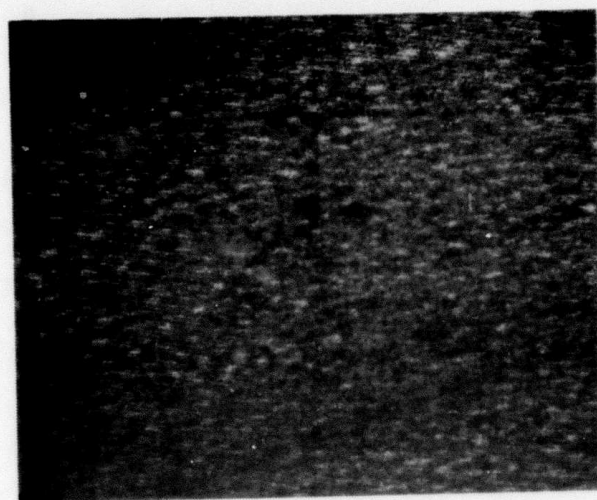
(a)



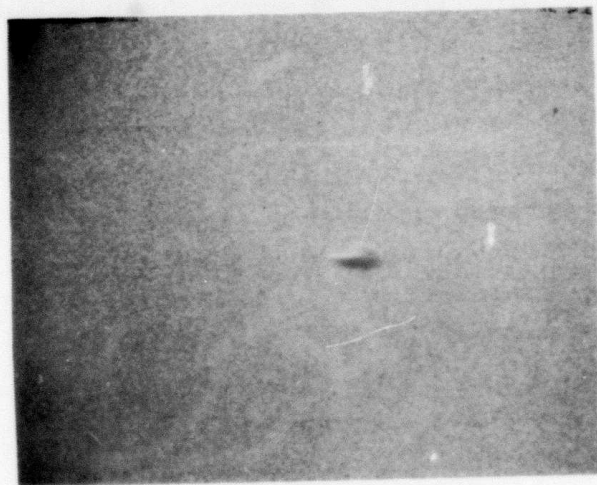
(b)

Figure 71. (a) Nomarski interference contrast. Ruby-laser anneal (2.3 J/cm^2) sample. (b) SEM of same sample at 20K magnification.

with a laser pulse of 1 J/cm^2 SEM reveals a fine structure (Fig. 72) on the surface which does not appear on the as-implanted (Fig. 72) sample. The various observed surface conditions created by different laser energy densities must be further investigated.



(a)



(b)

Figure 72. SEM photographs. (a) As-implanted sample at 20K magnification. (b) Ruby-laser-annealed sample at 1-J/cm^2 energy density (20K magnification).

SECTION VI

SUMMARY AND CONCLUSIONS

This program was aimed at three major areas. Epitaxial growth of high-resistivity GaAs, high-energy implantation of donors into GaAs, and the use of high-power lasers for annealing implanted GaAs layers were investigated. The significant results in these three areas are summarized below:

- (1) We have grown high-resistivity Cr-doped GaAs layers with good surface morphology using both the Ga/HCl/AsH₃/H₂ and the Ga/AsCl₃/H₂ processes. n-Layers grown on these epitaxial buffer layers have consistently shown better compensation than for direct growth on bulk-grown SI GaAs substrates. Cr-doped layers have been grown on both SI GaAs and n⁺-GaAs substrates. Ion implantation into epitaxial buffer layers, in general, leads to higher electron mobility than direct implantation.
- (2) SIMS measurements of the Cr profile in the epi-buffer and in n-layers grown on epitaxial Cr-doped buffers show that there can be an anomalous pile-up of Cr at the interfaces. Experiments indicate that this pile-up does not occur if growth is not interrupted. It is speculated that this pile-up may be related to deviations in gas-phase stoichiometry during the start of growth. While we can grow layers without Cr pile-up at the interface, the exact mechanism of the presence/absence of Cr pile-up is not understood.
- (3) While high-quality (low compensation) n-layers can be grown on Cr-doped buffer layers, problems arise during the growth of n⁺-n structures. This is particularly true when very highly doped ($\sim 10^{19} \text{ cm}^{-3}$) n⁺-layers are grown. The problem manifests itself as a "conducting knee" in the buffer. SIMS measurements indicate penetration of the n⁺-dopant into the buffer layer.
- (4) We have successfully grown high-resistivity layers on SI GaAs substrates by the process of NH₃ gettering. The addition of NH₃ to the gas stream reduces the background donor concentration by decreasing Si incorporation from the quartz reactor tube. Diffusion from the SI GaAs substrate compensates the remaining donors. n and n⁺-n structures can be grown on NH₃-gettered buffer layers without any anomalous effects as described in (3).

- (5) We have investigated implantation of $^{28}\text{Si}^+$ into SI GaAs up to an implant energy level of 1.2 MeV. A corresponding range of 1.1 μm was measured by SIMS. The electrical activation and mobility following thermal annealing are comparable to or higher than (depending on implant parameters) that of thermally annealed low-energy (50 to 250 keV) implanted samples. A higher activation was observed in 1-MeV Si-implanted GaAs than in the 200-keV implants in the high dose region (10^{14} to 10^{15} at./cm²). The electron density profiles measured on the 1-MeV implants showed a reasonable agreement with the normalized SIMS profile.
- (6) We have been studying the profiles and range statistics of ^{28}Si implanted GaAs with implant energies of up to 1.2 MeV using SIMS analysis, and based on the information obtained, uniformly doped ^{28}Si profiles ~ 1 μm deep have been produced in GaAs using multiple implants. After thermal annealing the measured electron density distribution confirms the 1- μm depth with an average electron density of $\sim 5 \times 10^{17}$ at./cm³.
- (7) We have been investigating laser annealing of high-dose Si-implanted GaAs using high-power pulsed Nd:glass laser and ruby laser. Electrical activation of high-dose, low-energy implanted samples are many times higher in laser-annealed samples than for those thermally annealed. Ohmic contacts formed onto laser-annealed samples without alloying have been demonstrated.
- (8) Optical absorption has been studied in Si-implanted GaAs wafers irradiated with high-power Nd:glass laser pulses. Measurements show that the implant-enhanced absorption at a given infrared wavelength increases with implant dose. The enhanced absorption is greatly reduced following annealing as a result of lattice reordering.
- (9) Impurity distribution in as-implanted, thermal-annealed, and laser-annealed samples has been investigated by SIMS analysis. The amount of impurity redistribution depends upon the energy and dose of implantation, and the energy density of the laser pulse used to anneal the sample. A substantial impurity broadening was observed in the high-dose implanted samples irradiated with a high energy-density (~ 2 J/cm²) pulse. The broadening is believed to be associated

with a diffusion in the liquid GaAs created by the high-energy laser pulse. An uneven ripple observed on such a surface using a Normarski interference contrast micrograph indicated the occurrence of melting at the sample surface.

An anomalous "shoulder broadening" effect was observed in the SIMS profile after thermal annealing in Si-implanted SI GaAs with a high peak impurity concentration in the implanted layer; the anomalous broadening is believed to be associated with the damage-enhanced diffusion associated with the heavy implantation.

REFERENCES

1. G. B. Stringfellow and G. Ham, "Hydride VPE Growth of GaAs for FETs," J. Electrochem. Soc. 124, 1806 (1977).
2. S. T. Jolly, et al., Epitaxial Growth of Semi-Insulating GaAs, Annual Report, Contract N00014-77-C-0542, DARPA Order No. 2461 Basic Program Code 7D10, March 1978.
3. S. T. Jolly et al., Epitaxial Growth of Semi-Insulating GaAs, Interim Report, Contract N00014-77-C-0542, DARPA Order No. 3461 Basic Program Code 7D10, March 1979.
4. H. M. Cox and J. V. DiLorenzo, "Characteristics of an $\text{AsCl}_3/\text{Ga}/\text{H}_2$ Two-Bubbler GaAs CVD System for MESFET Applications," Proc. Sixth Int. Symp. GaAs and Related Compounds; Inst. Phys. Conf. Series, No. 33b, London, 1977, pp. 11-22.
5. D. L. Rode and S. Knight, "Electron Mobility in GaAs," Phys. Rev. B3, 2534 (1971).
6. S. J. Bass, "Growth of Semi-Insulating Epitaxial GaAs by Cr Doping in the Metal Alkyl Hydride System," J. Cryst. Growth 44, 29 (1978).
7. R. Zucca, "Electrical Compensation in Semi-Insulating GaAs," J. Appl. Phys. 48, 1987 (1977).
8. R. L. Henry and E. M. Swiggard, "LEC Growth of InP and GaAs Using PBN Crucibles," Proc. Sixth Int. Symp. GaAs and Related Compounds, Inst. Phys. Conf. Series, 33b, London 1977, pp. 28-36.
9. D. R. Heath, P. R. Selway, and C. C. Tooke, "Photoconductivity and Infra-red Quenching in Chromium-doped Semi-insulating Gallium Arsenide," Brit. J. Appl. Phys. (J. Phys. D) 1 (Ser. 2), 29 (1968).
10. W. Pleasiewicz, "Photoelectronic Investigations of Semi-Insulating p-Type GaAs:Cr Containing Neutral Chromium Acceptors," J. Phys. Chem. Solids 38, 1079 (1977).
11. H. J. Stocker, "A Study of Deep Impurity Levels in GaAs Due to Cr and O by AC Photoconductivity," J. Appl. Phys. 48, 4583 (1977).
12. M. B. Panish and H. C. Casey, Jr., "Temperature Dependence of the Energy Gap in GaAs and GaP," J. Appl. Phys. 40, 163 (1969).
13. H. J. Stocker and M. Schmidt, "A Study of Deep Impurity Levels in GaAs," J. Appl. Phys. 47, 2450 (1976).
14. A. W. L. Lin, "Photoelectronic Properties of High Resistivity GaAs:O and GaAs:Cr Single Crystals," Ph.D. Thesis, Stanford University, 1975.

15. M. G. Kendall and A. Stuart, The Advanced Theory of Statistics, (Charles Griffin, London, 1958), Vol. 1, p. 148.
16. W. P. Elderton, Frequency Curves and Correlation, (Cambridge University Press, 1953), 4th ed.
17. W. K. Hofker, Implantation of Boron in Silicon, Philips Research Supplements, 1975, No. 8.
18. E. I. Shtyrkov, I. B. Khaibullin, M. M. Zaripov, M. F. Galyatudinov, and R. M. Bayazitov, "Local Annealing of Implantation Doped Semiconductor Layers," Sov. Phys. Semicond. 9, 1309 (1976).
19. S. U. Compisano, I. Catalano, G. Foti, E. Rimini, F. Eisen, and M. A. Nicolet, "Laser Reordering of Implanted Amorphous Layers in GaAs," Solid State Electron. 21, 485 (1978).
20. R. T. Young, C. W. White, G. J. Clar, J. Narayan, W. H. Christie, M. Murakami, P. W. King, and S. D. Karner, "Laser Annealing of Boron-Implanted Silicon," Appl. Phys. Lett. 32, 139 (1978).
21. S. G. Liu, C. P. Wu, and C. W. Magee, "Annealing of Ion-implanted GaAs with Nd:glass Laser," presented at the Symp. on Laser-Solid Interaction and Laser Processing held in Boston, MA, Nov. 28-Dec. 1, 1978. AIP Conference Proceedings No. 50, p. 603, New York, 1979.
22. B. J. Sealy, M. H. Badawi, S. S. Kular, and K. G. Stephens, "Electrical Properties of Laser-Annealed Donor-Implanted GaAs," Electron. Lett. 14, 720 (1978).
23. A. Gat and J. F. Gibbons, "A Laser-Scanning Apparatus for Annealing of Ion-Implantation Damage in Semiconductors," Appl. Phys. Lett. 32, 142 (1978).
24. W. D. Edward et al., "Specific Contact Resistance of Ohmic Contact to GaAs," Solid State Electron. 15, 388 (1972).
25. Y. Goldberg and B. V. Tsarenkov, "Dependence of the Resistance of Metal GaAs Ohmic Contacts on the Carrier Density," Soviet Phys. Semicond. 3, 1447 (1970).
26. H. H. Berger, "Models for Contacts to Planar Device," Solid State Electron. 15, 145 (1972). Also, J. Electrochem. Soc. 119, 507 (1972).
27. P. Williams, R. K. Lewis, C. A. Evans, and P. R. Hanley, "Evaluation of a Cesium Primary Ion Source on an Ion Microprobe Mass Spectrometer," Anal. Chem. 49, 1399 (1977).
28. C. W. Magee, J. Electrochem. Soc. (in press).

29. A. Lidow, J. F. Gibbons, V. R. Deline, and C. A. Evans, Jr., "Solid Solubility of Selenium in GaAs as Measured by Secondary Ion Mass Spectrometry," Appl. Phys. Lett. 32, 572 (1978).
30. W. L. Brown, J. A. Gdovchenko, K. A. Jackson, L. C. Kimerling, H. J. Leamy, G. L. Miller, J. M. Poate, J. W. Rodgers, G. A. Rozgonyi, T. T. Sheng, T. N. C. Venkatesan, and G. K. Celler, "Laser-Annealing of Ion-Implanted Semiconductors," Proc. on Rapid Solidification Proc. - Principles and Technologies, Reston, VA, Nov. 1977.

APPENDIX

VAN DER PAUW MEASUREMENTS OF HIGH-RESISTIVITY MATERIALS

In the measurement of carrier concentration and mobility of high-resistivity materials by van der Pauw techniques, it is necessary to utilize low-value currents through the specimen, first, because the current source sees resistances on the order of 100 M Ω , and secondly because the use of too large a current produces very nonlinear and often random results. Frequently, currents of 1 μ A or less must be used. The other limitation is that a high impedance voltmeter must be used when the output impedance of the sample is also on the order of 100 M Ω .

Figure A-1 shows the schematic diagram of the equipment used. The current source employed is a Keithley type 225 capable of supplying a controlled constant current down to 10 nA. Two Keithley 610C electrometers are used as operational amplifiers acting as a balanced impedance converter. The input impedance of this combination is nominally 10^{28} Ω .

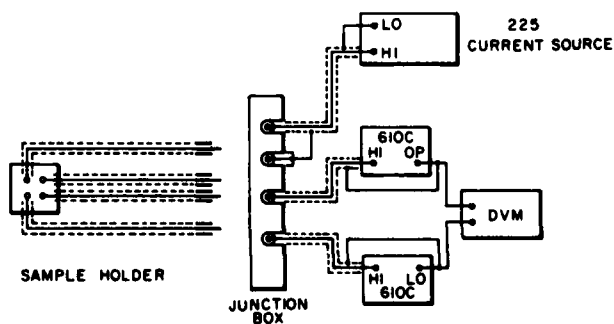


Figure A-1. Schematic of guarded high-impedance van der Pauw system.

To eliminate the effect of stray leakage currents, all connections from the specimen to the inputs of the electrometers are shielded, and the shields held at the same potential as the active connections to the high impedance side of the electrometers by connecting them to the low-impedance outputs of the

electrometers. The low-impedance output terminals of the amplifiers are connected to a conventional digital multimeter of 0.1-mV sensitivity.

Four shielded leads from the sample holder can be connected to any of four connections--2 input connections to the electrometer and 2 to the current source via a junction box. The coaxial plugs and sockets (BNC type) are manually interchanged for each van der Pauw measurement.

Contacts are made to the sample by sintering small pieces of tin wire to its corners at 500°C for 5 minutes in hydrogen. A little acid paste flux assists in wetting the contacts to the specimen and also holding them in place while handling the specimen.

Measurements made on van der Pauw specimens from wafers B392 and B394 are typical. The epitaxial layers in these runs were Cr-doped on undoped semi-insulating substrates.

B392

Layer thickness: 6.5 μm

Current used for measurement: 1 μA

Resistivity: 1018 $\Omega\text{-cm}$

N: $3.35 \times 10^{12}/\text{cm}^2$ at 300 K

Mobility: $1831 \text{ cm}^2 \text{V}^{-1} \text{s}^{-1}$

B394

Layer thickness: 6.5 μm

Current used for measurement: 1 μA

Resistivity: 49.6 $\Omega\text{-cm}$

N: 2.7×10^{13} at 300 K

Mobility: $4647 \text{ cm}^2 \text{V}^{-1} \text{s}^{-1}$

No meaningful measurements were made at 77 K.

DISTRIBUTION LIST - TECHNICAL REPORTS
CONTRACT N00014-77-C-0542

DARPA 1400 Wilson Blvd. Arlington, VA 22209 (Attn: Program Management)	2	Dr. M. Malbon/M.S. 1C Avantek, Inc. 3175 Bowers Avenue Santa Clara, CA 94304	1
Office of Naval Research Code 427Y 800 North Quincy Street Arlington, VA 22217	4	Mr. R. Bierig Raytheon Company 28 Seyon Street Waltham, MA 02154	1
Naval Research Laboratory 4555 Overlook Avenue, S.W. Washington, D.C. 20375 Attn: Code 2627 6800	6 1	Dr. R. Bell, K-101 Varian Associates, Inc. 611 Hansen Way Palo Alto, CA 94304	1
TACTEC Battelle Memorial Institute 505 King Avenue Columbus, OH 43201	1	Dr. H. C. Nathanson Westinghouse Research and Development Center Beulah Road Pittsburgh, PA 15235	1
Defense Contract Administration Services Resident Office RCA Government Systems Division Route 38, Building 204-1 Cherry Hill, New Jersey 08358	1	Dr. Daniel Chen Rockwell International Science Center P. O. Box 1085 Thousand Oaks, CA 91360	1
Defense Documentation Center Building 5, Cameron Station Alexandria, VA 22314	12	Mr. G. J. Gilbert MSC 100 Schoolhouse Road Somerset, NJ 08873	1
Dr. Y. S. Park AFAL/DHR Building 450 Wright-Patterson AFB Ohio 45433	1	Dr. D. Krumn Hughes Research Laboratory 3011 Malibu Canyon Road Malibu, CA 90265	1
ERADCOM DELET-M Fort Monmouth, NJ 07703	1	Mr. Lothar Wandinger ECOM/AMSEL/TL/IJ Fort Monmouth, NJ 07003	1
Texas Instruments M.S. 105/D. Shaw P. O. Box 5936 Dallas, TX 75222	1	Dr. Harry Wieder Naval Ocean Systems Center Code 922 271 Catalina Blvd. San Diego, CA 92152	1

Dr. William Lindley MIT Lincoln Laboratory FI24A, P. O. Box 73 Lexington, MA 02173	1	Professor Walter Ku Phillips Hall Cornell University Ithaca, NY 14853	1
Commander U.S. Army Electronics Command V. Gelnovatch (DRSEL-TL-IC) Fort Monmouth, NJ 07703	1	Commander Harry Diamond Laboratories Mr. Horst W. A. Gerlach 2800 Powder Mill Road Adelphia, MD 20783	1
RCA Microwave Technology Center Dr. F. Sterzer Princeton, NJ 08540	1	Advisory Group on Electron Devices 201 Varick Street, 9th floor New York, NY 10014	1
Hewlett-Packard Corporation Dr. Robert Archer 1501 Page Mill Road Palo Alto, CA 94306	1	D. Claxton MS/1414 TRW Systems One Space Park Redondo Beach, CA 90278	1
Watkins-Johnson Company E. J. Crescenzi, Jr./ K. Niclas 3333 Hillview Avenue Stanford Industrial Park Palo Alto, CA 94304	1	Professor L. Eastman Phillips Hall Cornell University Ithaca, NY 14853	1
Commandant Marine Corps Scientific Advisor (Code AX) Washington, D.C. 20380	1	AIL TECH 612 N. Mary Avenue Sunnyvale, CA 94086 Attn: D. G. Vendelin	1
Communications Transistor Corp. Dr. W. Weisenberger 301 Industrial Way San Carlos, CA 94070	1	Professors Hauser and Littlejohn Department of Electrical Engr. North Carolina State University Raleigh, NC 27607	1
Microwave Associates Northwest Industrial Park Drs. F. A. Brand/J. Saloom Burlington, MA 01803	1		
Commander, AFAL AFAL/DHM Mr. Richard L. Remski Wright-Patterson AFB, OH 45433	1		